

**Global Observations of Martian Clouds with the  
Mars Orbiter Camera of the Mars Global  
Surveyor Spacecraft**

Thesis by

Huiqun Wang

In Partial Fulfillment of the Requirements for the Degree of

Doctor of Philosophy

CALIFORNIA INSTITUTE OF TECHNOLOGY

Pasadena, California

2004

Defended July 18, 2003

© 2004

Huiqun Wang

All Rights Reserved

## Acknowledgements

It has been six years since I came to Caltech. Many people have helped me with my study and research during this period. The completion of this thesis will not be possible without them.

First of all, I am indebted to my thesis advisor, Andrew P. Ingersoll, who has been extraordinarily supportive, informative and patient all these years. Under his guidance, I have been able to pursue my thesis research with confidence and freedom. With his support, I had the opportunity to attend the 2002 GFD summer school which was very beneficial.

I thank Bruce Murray for being my academic advisor. When I first came to Caltech, he organized JPL visits for new students. These visits gave me a great introduction to planetary sciences.

I thank Mark Richardson for his great help during the last two years. With his help, I was able to investigate spacecraft observations with GCM simulations, and found a new avenue for future research.

I thank my thesis advisory committee – Arden Albee, Edward Danielson, Andy Ingersoll, Bruce Murray and Mark Richardson for all the time and thoughts they devoted to my TAC meetings to keep me on track.

I thank David Stevenson for supervising the Europa project in my first year as a graduate student.

I thank Mike Black and Shawn Ewald for solving my numerous computer problems.

I thank Adam Showman, Yibo Jiang, Ashwin Vasavada, Chunhua Qi, Anthony Toigo, Lori Fenton, Antonin Bouchez, Shane Byrne, Junjun Liu, and Shabari Basu for help and discussions.

I thank all the staff members for their help.

I thank my grandparents, parents and husband for their love and support.

# Table of Contents

Acknowledgements.....	iii
Overview.....	xi
Chapter 1: Martian Clouds Observed by Mars Global Surveyor Mars Orbiter Camera. Results for the First Mapping Year.....	1
1.1 Abstract.....	2
1.2 Introduction .....	3
1.3 Data processing .....	5
1.4 Tropical cloud distribution .....	10
1.4.1 General features.....	12
1.4.2 Non-uniform decay of the tropical cloud belt .....	13
1.4.3 Cloud morphology of the tropical cloud belt .....	15
1.4.4 Aster clouds above the volcanoes .....	18
1.5 North polar clouds .....	20
1.5.1 North polar hood formation ( $L_s$ 160°~185°).....	20
1.5.2 North polar streak clouds .....	24
1.5.3 North polar lee waves.....	27
1.5.4 Spiral clouds.....	30
1.6 South polar clouds .....	34
1.6.1 Development of the south polar hood .....	35
1.6.2 South polar clouds from mid winter to mid summer.....	38
1.6.3 South polar lee waves.....	40
1.7 Conclusion.....	41
1.8 Acknowledgments .....	43
1.9 References .....	44
Chapter 2: Cyclones, Tides, and the Origin of a Cross-Equatorial Dust Storm on Mars .....	48
2.1 Abstract.....	49
2.2 Introduction .....	49
2.3 Analysis with GCM.....	53
2.4 Discussion.....	61
2.5 References .....	62
Chapter 3: Cloud-tracked winds for the first Mars Global Surveyor mapping year.....	65
3.1 Abstract.....	66
3.2 Introduction .....	67
3.3 Cloud-tracked winds.....	70
3.3.1 North polar region during $L_s$ 135°-195° .....	70
3.3.2 North polar region during $L_s$ 20°-55° .....	77
3.3.3 South polar region during $L_s$ 337°-10° .....	78
3.4 Zonal mean winds.....	81
3.4.1 North polar region during $L_s$ 135°-195° .....	82
3.4.2 North polar region during $L_s$ 25°-55° .....	85
3.4.3 South polar region during $L_s$ 337°-10° .....	85
3.5 Latitudinal distribution of zonal wind .....	86

3.6 Eddy winds .....	91
3.6.1 Fourier wave components .....	91
3.6.2 Eddy momentum flux and eddy kinetic energy .....	93
3.7 Summary .....	97
3.8 References .....	99
3.9 Acknowledgements .....	101
<b>Chapter 4: Martian Clouds Observed by the Mars Global Surveyor Mars Orbiter Camera. Results for the Second Martian Year.....</b>	<b>102</b>
4.1 Introduction .....	103
4.2 The 2001 global dust storm .....	103
4.2.1 Effects on photometric processing .....	103
4.2.2 Storm evolution .....	105
4.2.3 Effects on surface albedo .....	109
4.2.4 Effects on polar clouds .....	110
4.2.5 Global dust storm initiation .....	112
4.3 Global condensate cloud distribution .....	115
4.4 Recurrent phenomena .....	118
4.4.1 Aster clouds .....	119
4.4.2 Polar clouds .....	120
4.4.3 “Flushing” dust storms .....	122
4.4.4 Spiral clouds .....	123
4.5 Summary .....	125
4.6 References .....	126
Appendix .....	129

## Table of Figures

Plate 1.1 Image processing and daily global map .....	5
Figure 1.1 Seasonal cloud distribution in the equatorial maps .....	11
Figure 1.2 The decaying tropical cloud belt in mid northern summer .....	15
Figure 1.3 (a) Fibrous clouds. (b) Convective clouds. (c) Cloud streets. (d) Actinae clouds .....	17
Figure 1.4 Aster clouds in mid northern summer .....	19
Plate 1.2 Representative north polar stereographic maps .....	21
Plate 1.3 (a) Fraction of cloud covered area between 60°N and 75°N as a function of Ls. (b) North polar map at Ls 164°. (c) Total clouds. (d) Dust clouds. (e) Condensate clouds .....	23
Figure 1.5 Streaks traced in six consecutive north polar maps .....	25
Figure 1.6 Spatial distribution of lee waves in the north and south polar map.....	28
Figure 1.7 Temporal distribution of lee waves in the north and south polar maps...	29
Plate 1.4 Spiral clouds observed by MOC during Ls 134°~360°~111° .....	31
Plate 1.5 Spiral clouds in the north polar region during Ls 160°~185° .....	34
Plate 1.6 Representative south polar stereographic maps .....	36
Figure 1.8 Fraction of cloud covered area as a function of Ls .....	37
Figure 1.9 Dust activity in the south polar region in the southern summer .....	39
Figure 2.1 (ab) Example MGS MOC wide-angle images of southward moving storms. (c) Mid-level air temperatures observed by TES as a function of Ls .....	51

Figure 2.2 Particle distribution maps from a Lagrangian transport analysis for a front (a-c) with and (d-f) without significant southward motion .....	55
Figure 2.3 Mean southward particle transport rate derived from the tracer analysis..	57
Figure 2.4 (a-c) Lagrangian particle maps with interactive particle injection for the Ls ~342° storm. (d) The surface wind stress, lowest level model winds, and surface pressure perturbation at the time when the low pressure center passes 0°E.....	60
Figure 3.1 Consecutive processed global map swaths and the measured winds .....	67
Figure 3.2 Wind vectors collected for the north polar region from mid northern summer to early northern fall.....	71
Figure 3.3 Circulation patterns derived for each panel in Fig. 3.2 .....	73
Figure 3.4 Wind vectors collected in the north polar region during northern spring .	76
Figure 3.5 Circulation patterns derived for each panel in Fig. 3.4 .....	78
Figure 3.6 Wind vectors collected in the south polar region from mid southern summer to early fall .....	80
Figure 3.7 Zonal mean zonal and meridional winds in 60°-70°N/S and 70°-80°N/S .	81
Figure 3.8 (a) Latitudinal distribution of zonal winds within 50°N-75°N. (b) Latitudinal distribution of $u^*/\cos(\text{latitude})$ . (c) Latitudinal distribution of absolute vorticity.....	89
Figure 3.9 GFDL GCM simulated zonal wind $u^*/\cos(\text{latitude})$ and absolute vorticity within 50°-75°N for 3.0 mb and 3.8 mb .....	90
Figure 3.10 (a) Meridional winds at 70°N. (b-d) Longitude-Ls cross sections for Fourier wave 1, 2, and 3.....	93

Plate 3.1 Eddy momentum flux and Eddy kinetic energy derived from the cloud tracked winds.....	96
Plate 3.2 Eddy momentum flux and eddy kinetic energy derived from winds at 224 Pa simulated by the GFDL Mars GCM .....	97
Figure 4.1 Processed red and blue images from the two Martian years .....	105
Figure 4.2 Evolution of the 2001 global dust storm .....	107
Figure 4.3 South polar maps during the 2001 global dust storm .....	108
Figure 4.4 Equatorial maps at Ls 300° for the first and second Martian year .....	110
Figure 4.5 South polar maps for the first and second Martian year .....	111
Figure 4.6 North polar maps for the first and second Martian year .....	112
Figure 4.7 Hellas dust storms in the first Martian year .....	114
Figure 4.8 Hellas dust storms in the second Martian year .....	114
Figure 4.9 Cloud occurrence frequency maps for the second Martian year .....	115
Figure 4.10 Decaying tropical cloud belt in the first and second Martian year ....	118
Figure 4.11 Aster clouds above Arsia Mons in the second Martian year .....	119
Figure 4.12 Comparison for the north polar maps from mid to late northern summer between the two Martian years .....	121
Figure 4.13 Comparison for the south polar maps from mid to late southern winter between the two Martian years .....	121
Figure 4.14 Example “flushing” storms in the first and second Martian year .....	124
Figure 4.15 Example spiral clouds of the first and second Martian year .....	125

Figure 5.1 The brightness of the pixels between Line 700 and Line 900 as a function of the sample number for global map swath m0300717 (Left, red image) and m0300718 (Right, blue image).....	129
Figure 5.2 Distribution of incidence angle (left), emission angle (middle), and phase angle (right) for image m0300717.....	131
Figure 5.3 Least squares fit results for the pixels between Line 700 and Line 900 of the (a) red image m0300717 and (b) blue image m0200381. Black dots are signals in the radiometrically calibrated images, red dots are the corresponding results calculated using parameters derived from least squares fit.....	133

## Overview

We have studied the global cloud distribution on Mars using red and blue global map swaths taken by the Mars Global Surveyor (MGS) Mars Orbiter Camera (MOC).

In Chapters 1 and 4, we summarize the results for the first and second MGS mapping years, respectively. In Chapter 2, we investigate the mechanism for a new type of “flushing” dust storm first observed by MGS. These dust storms moved from the northern high latitudes southward across the equator, and led to a planet-encircling dust storm in the first MGS mapping year (1999). In Chapter 3, we track cloud motion to measure winds using images separated by 2 hours.

The systematic daily global coverage of MGS not only provides us with detailed and coherent pictures of Martian cloud evolution, but also increases the number of cloud-tracked wind vectors by three orders of magnitude. Except for the global dust storm in the second MGS mapping year (2001), Martian weather is highly repeatable. When the 2001 global dust storm initiated, Hellas storms increased in frequency, transporting dust out of the basin daily. When the 1999 planet-encircling dust storm initiated, “flushing” storms also increased in frequency, transporting dust to the southern subtropics daily. These observations suggest that timely dust supply by local or regional storms could have a global impact.

# **Chapter 1: Martian Clouds Observed by Mars Global Surveyor Mars Orbiter Camera. Results for the First Mapping Year**

Huiqun Wang and Andrew P. Ingersoll

Division of Geological and Planetary Sciences,  
California Institute of Technology, Pasadena

Published in modified form in *Journal of Geophysical Research – Planets*, 107, E10, 5078, doi: 10.1029/2001JE001815, 2002.

## 1.1 Abstract

We have made daily global maps that cover both polar and equatorial regions of Mars for  $L_s$  135°-360° and 0°-111° using the Mars Global Surveyor (MGS) Mars Orbiter Camera (MOC) red and blue wide-angle swaths taken from May 1999 to January 2001. We studied the seasonal distribution of condensate clouds and dust clouds during roughly one Martian year using these daily global maps. We present the development and decay of the tropical cloud belt and the polar hoods, the spatial and temporal distributions of lee waves and spiral clouds, and an unusual “aster” cloud above the volcanoes, consisting of rays around a central disk, like the flower. The tropical cloud belt contains mostly fibrous clouds during northern spring/early summer and convective clouds during middle/late northern summer. The detailed development and decay of the tropical cloud belt is non-uniform in longitude. Two distinct stormy periods in late summer precede the formation of the north and south circumpolar hoods. The north polar storms in late summer resemble baroclinic frontal systems on Earth, but contain both dust and condensate clouds. Spiral clouds occur only in the northern high latitudes, and only during northern spring and summer. The north polar hood displays a stationary wavenumber two structure during the fall and winter. The south polar hood has fewer streak clouds and lee wave clouds than the north polar hood. During this particular year, the lee wave cloud abundance in the south had two peaks (in early fall and late winter), and the lee wave cloud abundance in the north had one peak (in early fall).

## 1.2 Introduction

The distribution of clouds is important for the understanding of the Martian atmosphere, and is closely related to the Martian water cycle, dust cycle, and CO<sub>2</sub> cycle. The polar hoods, tropical clouds and dust storms have long been known through telescopic and spacecraft observations [Snyder et al., 1992; Martin et al., 1992]. French et al. [1981] documented the distribution of fogs, dust plumes, streak clouds, cloud streets, wave clouds and lee waves using the Mariner 9 and some Viking Orbiter images. Kahn [1984] added the thin haze, moderate haze and thick haze categories, and constructed a more complete catalog by including all Mariner 9 and Viking images. He further discussed the meteorological implications. Viking Infrared Thermal Mapper (IRTM) data have also been used to map the distribution of water ice clouds [Tamppari et al., 2000]. However, previous spacecraft observations have strong selection effects due to the characteristics of their orbits. For example, of the total of over 49,500 images taken by Viking, only 18 were taken north of 60°N during Ls 270°~325° [Kahn, 1984].

The Mars Global Surveyor (MGS) is in a polar orbit with a period of about two hours. The ascending leg of the orbit crosses the equator of Mars from south to north at about 1400 LT (2 PM local time). The red (575-625nm) and blue (400-450nm) “push broom” wide-angle cameras produce 7.5 km/pixel global map swaths. Twelve consecutive swaths can cover the whole planet in one day at this resolution. The operation of the Mars Orbiter Camera (MOC) is described in Malin and Edgett [2001].

The systematic spatial and temporal coverage of MGS provides us with a good opportunity to monitor clouds on Mars.

Compared with other Martian imagery studies, the MOC has regular two-hour coverage in the red and blue wavelengths. Dust and condensate clouds can be simultaneously identified according to their different colors. The lifecycles of storms and the seasonal distribution of clouds can be easily monitored due to the systematic coverage. However, the observations are largely limited to the early afternoon hours.

We will show the global cloud distribution observed by MOC during the observational period of about one Martian year (May 1999 to January 2001:  $L_s$  135°-360°-111°). Our data set is the same as that used by Cantor et al. [2001] in their comprehensive analysis of dust clouds. Our analysis covers both dust clouds and condensate clouds and the relationship between them. We will describe the development and decay of the tropical cloud belt and the polar hoods, the cloud morphology within the tropical cloud belt and the polar hoods, the evolution of streak clouds, the distribution of polar lee waves and spiral clouds, and the “aster” clouds associated with the volcanoes.

### 1.3 Data processing

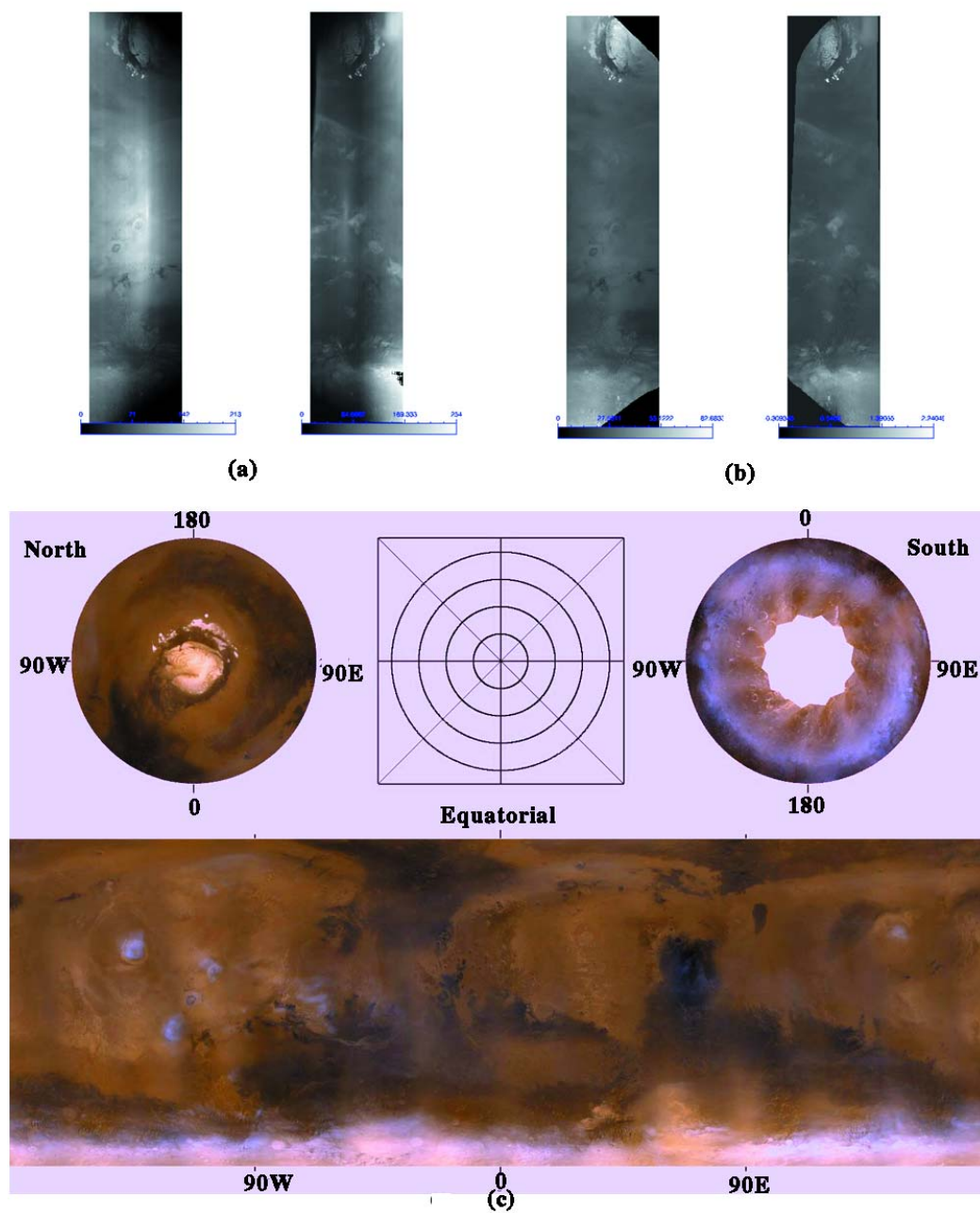


**Plate 1.1** Image processing and daily global map. (a) Raw global map swath pair. Left: red image m02-01707. Right: blue image m02-01708. The blue image is flipped left-right with respect to the red image. (b) Processed global map swath pair. Left: red image m02-01707. Right: Blue image m0201708. (c) Daily global map for  $L_s \sim 154^\circ$ . Upper left: north polar map ( $45^\circ\text{N}$ - $90^\circ\text{N}$ ,  $0.1^\circ \times 0.1^\circ$ )

in polar stereographic projection. Upper right: south polar map (45°S-90°S, 0.1° × 0.1°) in polar stereographic projection. Lower: equatorial map (60°S-60°N, 0.1° × 0.1°) in simple cylindrical equidistant projection. The upper middle Panel shows the pole and the latitudinal circles every 10° for the polar maps.

A raw red and blue global map swath pair taken by MOC is shown in Plate 1.1 (a). The blue image is flipped left-right with respect to the red. The red image is more sensitive to dust clouds. The blue image is more sensitive to ice clouds [James, 1985; Cantor et al., 2001]. Variable summation in the cross-track direction has been applied to these global images to maintain a fixed resolution of 7.5 km/pixel. The dark corners at the top and bottom are within the terminator (in darkness). The bright spot in the middle of each image occurs at 0°-phase angle. This brightness increase towards 0°-phase angle is called the “opposition surge” [Hapke, 1986]. It is a special case of the more general dependence of the observed brightness on the geometry that can be expressed as the bi-directional reflectance. Besides the geometry effect, variations in the camera response can also cause brightness variations in the global map swaths. Variations in the camera response have a low-frequency component and a high-frequency component [Caplinger, 1997]. The low-frequency component refers to the general cross-track brightness variation in an image of an evenly bright target. The high-frequency component refers to the pixel-to-pixel brightness variation (the vertical streaks in Plate 1.1 (a)) due to the sensitivity variation of the camera CCD line array. The raw images are processed (see the next paragraph) so that these effects are minimized (see Plate 1.1 (b)).

To remove the low-frequency brightness variations, including the opposition surge, we calculate the radiometric signal (data number/msec) generated at the focal plane using the MOC response equation in MOC2 calibration report [Caplinger, 1997]. We apply the following empirical function with parameters listed in Table 1.1 to both the red and the blue global map:

$$\begin{aligned}
 DN_{new} &= DN_{old} \frac{r(i_0, e_0, g_0)}{r(i, e, g)} \\
 r(i, e, g) &= \frac{\mu_0}{\mu_0 + \mu} H(\gamma, \mu_0) H(\gamma, \mu) \bullet \\
 &\quad \left[ f \cdot G(k_1, g) + (1 - f) \cdot G(k_2, g) \right] \bullet \\
 &\quad \left[ 1 + \frac{B_0}{1 + h_1 \cdot \tan(g/2)} + \frac{a_1}{\exp(g/\alpha)} \right] \quad (1.1) \\
 H(\gamma, x) &= \frac{1 + 2x}{1 + 2\gamma x} \\
 G(k, g) &= \frac{1 - k^2}{\left[ 1 + k^2 + 2k \cdot \cos(g) \right]^{3/2}}
 \end{aligned}$$

where  $i$  is the incidence angle,  $e$  is the emission angle,  $g$  is the phase angle,  $\mu_0 = \cos(i)$ ,  $\mu = \cos(e)$ .  $DN_{old}$  is the signal after just the gain and offset corrections, and  $DN_{new}$  is the signal after the photometric processing.  $\gamma$  is a parameter used to characterize the brightness dependence on incidence and emission angles,  $B_0$  is the amplitude of the opposition surge, and  $h_1$  is the half-width of the opposition surge [Hapke, 1986].  $a_1$  and  $\alpha$  are additional parameters used to tune the shape of the opposition surge.  $k$  is the parameter used in the Henyey-Greenstein phase function

$G(k, g)$ .  $f$  is the fraction parameter . Appendix 1 explains the derivation of the parameters used in Equation 1.1.

Equation 1.1 is similar to Hapke's bi-directional reflectance function [Hapke, 1986]. In order to derive the values for the parameters in Equation 1.1, we first selected red and blue images with small albedo variations from the early northern fall global map swaths that were available at the time when we developed the photometric calibration. In each image, the emission angle ranges from  $0^\circ$  to  $90^\circ$ , and the incidence angle ranges from  $\sim 20^\circ$  to  $90^\circ$ . The phase angle ranges from  $0^\circ$  to  $115^\circ$ . These ranges are sufficient to determine the eight parameters of our model by the method of least squares. We attach no physical significance to the parameter values. Indeed, these parameter values include contributions from the low frequency response of the MOC as well as the Mars bi-directional reflectance. We use the model only to reduce the effects of viewing geometry and enhance the visibility of the clouds. The fit deteriorates toward the terminator, so the pixels with incident angles greater than  $\sim 87^\circ$  are ignored in our processed images. Experiments with the global map swaths for this study show that in most cases, the opposition surges can be successfully removed, the clouds can be easily distinguished from the surfaces, and the seams between the overlap images in the daily global maps are much less apparent than the clouds and surfaces (see Plate 1.1 (c)).

filter	$\gamma$	$B_0$	$h_1$	$a_1$	$\alpha$ ( $^\circ$ )	$f$	$k_1$	$k_2$
Red	-0.0888	0.515	15.5	0.1	15.0	0.48	0.484	-0.112
Blue	0.615	1.05	17.5	0.8	20.0	0.92	0.82	-0.075

**Table 1.1** Parameters used in Function (1) for red and blue cameras

To remove the high-frequency brightness variations (“streaks,” see Plate 1.1 (a)), we use images in which the low-frequency variations have been removed according to the above prescription. We determine the average brightness of each pixel in the MOC line array for low contrast scenes. The mean of this line array is normalized to unity and stored in a file. To process an image, we divide each line by this normalized line array. Plate 1.1 (b) shows the processed images with the large scale brightness variations and the streaks removed.

We mosaic 13 consecutive global map swath pairs into a red and a blue daily global map. Consecutive maps overlap each other by one swath pair. We use a weighted average to mosaic the global map swaths, i.e., the pixel that has smaller incidence and phase angles and lies farther from the image corners makes a larger contribution to the value in the overlap region, and vice versa. Our currently processed global map swaths cover the period from  $L_s \sim 134^\circ$  of the first Martian year to  $L_s \sim 111^\circ$  of the second Martian year, where  $L_s$  is the areocentric longitude of the sun (Northern summer starts at  $L_s = 90^\circ$ , and northern winter starts at  $L_s = 270^\circ$ ). All our daily global maps have the same  $0.1^\circ$  by  $0.1^\circ$  map grid. The equatorial map is in simple cylindrical equidistant projection and spans  $60^\circ\text{S}$ - $60^\circ\text{N}$ . The polar maps are in polar stereographic projections and extend out to  $\pm 45^\circ$ . If there are missing data in the raw images, then gaps will occur accordingly in the daily global maps. To make three-color daily global maps, we first normalize the average brightness in the relatively cloud-free region between  $10^\circ\text{N}$  and  $40^\circ\text{N}$ ,  $305^\circ$ - $360^\circ\text{W}$  for the equatorial maps, and that in the region

between  $57.5^{\circ}\text{N}$  and  $60^{\circ}\text{N}$ ,  $90^{\circ}$ - $180^{\circ}\text{W}$  for the polar maps. The same linear stretch is applied to all the red maps and likewise for the blue maps. We synthesize the green maps by combining  $1/3$  red and  $2/3$  blue and then apply a common linear stretch. The color daily global map for  $L_s \sim 154^{\circ}$  is shown in Plate 1.1 (c). The terminator circle in the south polar maps is approximately outlined by the  $87^{\circ}$ -incidence angle, and the abnormal color near the terminator is due to the behavior of the photometric function (Equation 1.1) at large incidence and phase angles.

The equatorial and polar maps were animated to show the day to day changes on Mars. Each processed red and blue swath pair was projected and combined into a color image following the same procedure. Since the consecutive projected images in the polar region have relatively large overlaps, they were animated to show changes on a two-hour timescale.

## **1.4 Tropical cloud distribution**

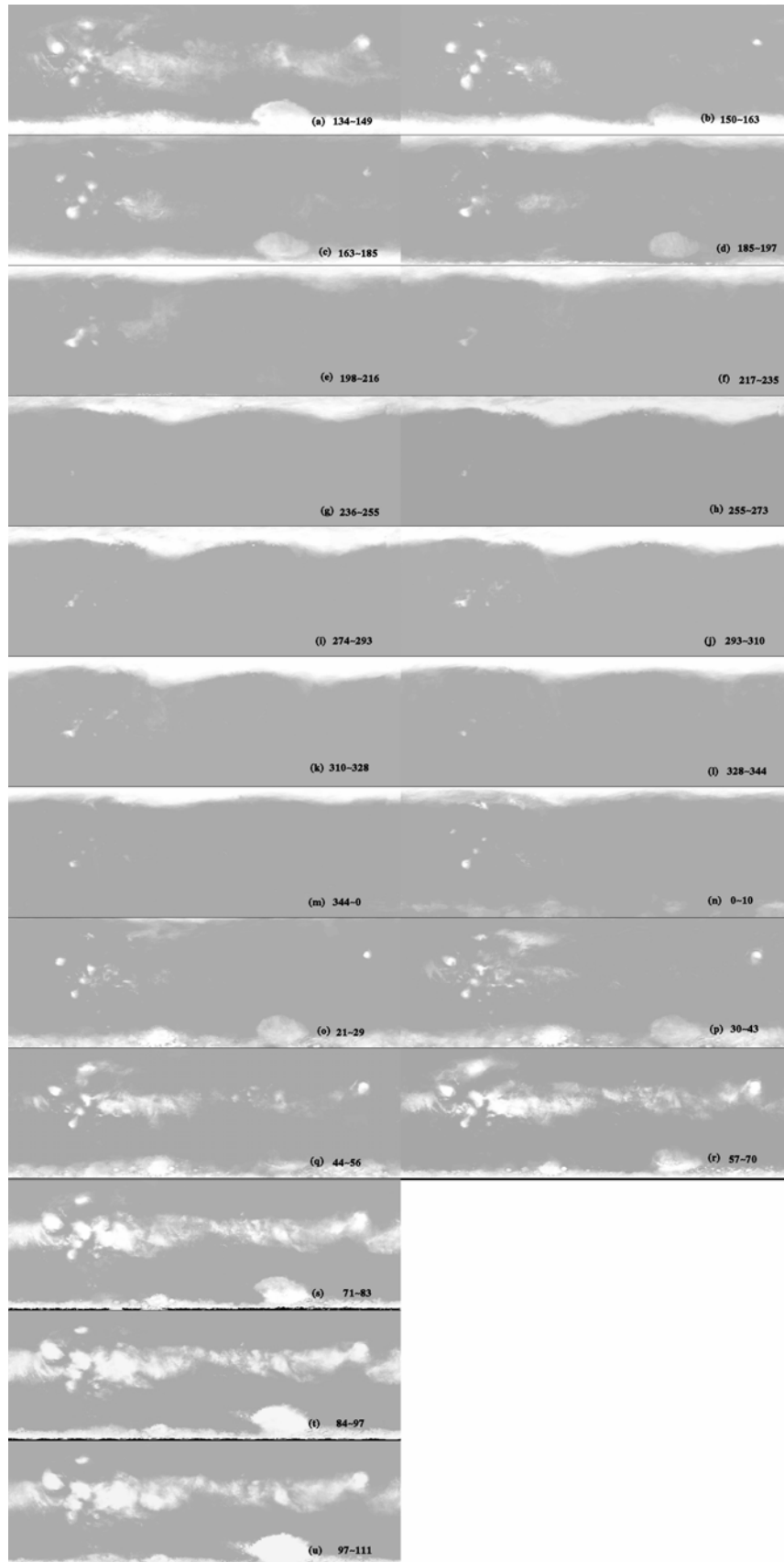


**Figure 1.1** Seasonal cloud distribution in the equatorial maps. Each panel has the same format as the equatorial map shown in Plate 1.1. The panels are averages for the accompanying  $L_s$  intervals. See text for further detail.

The most prominent seasonal cloud variations during the Martian year are the development and decay of the north and south polar hoods and the tropical cloud belt. Figure 1.1 is a summary of cloud occurrence frequency in  $L_s$  intervals  $\sim 15^\circ$  wide. In constructing Fig. 1.1, we select pixels that are more than 25% brighter in the blue filter than the mean brightness of the map. The 25% threshold is valid only for our image processing, and was chosen so that the polar cap and condensate clouds are well identified. In most cases, dust storms are below this threshold. We verify these identifications by visual inspection. To enhance the contrast, we set the selected pixels in each daily equatorial map to the maximum value and other pixels to the mean value of the map. We then average these results over a range of  $L_s$  to get the panels of Fig. 1.1, so the selected pixels in the high latitudes could represent clouds in most cases as well. If there are missing data in a daily equatorial map, we fill in the gap with the values of the corresponding pixels from the previous day's or the next day's map, or it is left blank if no data exist for 3 consecutive days.

### 1.4.1 General features

The tropical cloud belt develops during northern mid spring, peaks around northern summer solstice, and decays during mid northern summer. This evolution is shown in Fig. 1.1. The belt of clouds quickly disintegrates during  $L_s$   $134^\circ\sim 149^\circ$ . As a result, only the topographic clouds associated with the volcanoes and Valles Marineris are left in late northern summer. These clouds keep diminishing until they redevelop

at the beginning of the northern spring. The cloud patch associated with Arsia Mons is the only one that remains throughout the year. The cloud belt begins to develop after  $L_s \sim 44^\circ$  in the second Martian year. It becomes longitudinally continuous during  $L_s 57^\circ \sim 70^\circ$  and remains so until the end of our observational period,  $L_s \sim 111^\circ$ . The fact that the tropical cloud belt appears in the northern spring and summer but not in the southern spring and summer is probably a reflection of the lack of water vapor sources in the southern hemisphere.

The main belt lies between  $\sim 10^\circ\text{S}$  and  $\sim 20^\circ\text{N}$ . It is widest around Valles Marineris, and is only weakly developed around Arabia Terra. Clouds occur most frequently around the volcanoes, Valles Marineris and Syrtis Major. The evolution of the cloud belt this Martian year generally agrees with that of the Viking era water ice clouds [Tamppari et al., 2000]. The differences occur mainly in northern spring around  $L_s \sim 65^\circ$ . Compared with the MGS observations, the Viking era water ice clouds are more extensive near the upland regions including Arabia Terra, and the clouds near Valles Marineris appear poorly developed, compared with those in other longitudes.

#### **1.4.2 Non-uniform decay of the tropical cloud belt**

The decaying phase of the tropical cloud belt in mid northern summer is short but complex. The cloud belt fluctuates on a timescale of days. Gaps appear at different longitudes, and the branches that extend off to higher latitudes fade away at different rates. These changes are shown in Fig. 1.2 (a, b, and c). These are daily maps in contrast to those of Fig. 1.1, which are averages over  $\sim 15^\circ$  of  $L_s$ . The main cloud belt is sinuous and begins to break apart in Amazonis and Arabia Planitia during  $L_s$

134°~142°. Clouds outside the main belt can often be observed at higher latitudes over Acidalia Planitia (see ~55°N, 50°W in Fig. 1.2 (a)), Utopia Planitia (see ~57°N, 275°W in Fig. 1.2 (a)) and Thaumasia Fossae (see ~35°S, 100°W in Fig. 1.2 (a)). The clouds over Acidalia Planitia often appear to be connected with the main tropical cloud belt through a branch of clouds near Tempe Fossae. Sometimes, a faint cloud branch can also be observed extending from southeast Valles Marineris toward Hellas basin. The clouds over Thaumasia Fossae sometimes appear to form a cloud branch as well. However, the clouds over Utopia Planitia remain disconnected from the main belt during our observational period (Fig. 1.2 (a)). There could be a branch of clouds connecting the Utopia clouds with the main belt earlier in the season, but they may have dissipated by the time of our observation. Cloud branches extending from the main belt toward higher latitudes have been observed by Hubble Space Telescope around  $L_s \sim 63^\circ$  [James et al., 1996], and they are simulated by GCM [Richardson and Wilson, 2002]. The clouds in the western hemisphere (0°-90°-180°W) diminish after  $L_s \sim 142^\circ$ . The clouds between Syrtis and Elysium brighten briefly and then quickly disintegrate within about a week.

The developing phase of the cloud belt is non-uniform too. During the MGS year, clouds developed first near Valles Marineris and last near Arabia Planitia (see Fig. 1.1). This is just the opposite of that found by Tamppari et al. [2000] for the Viking era.

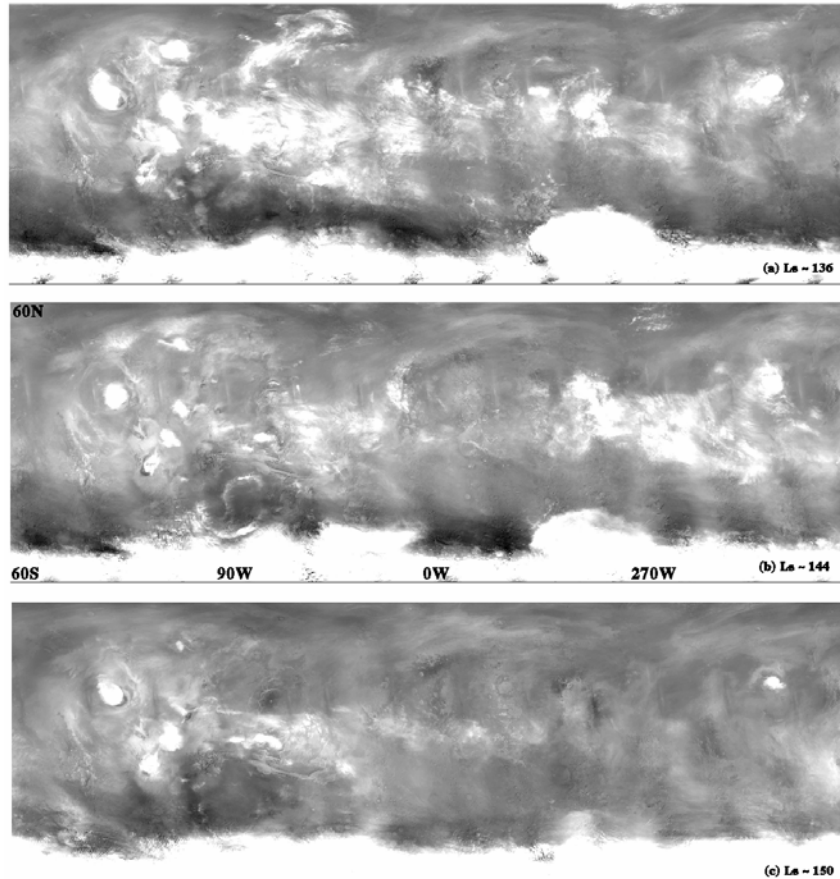


**Figure 1.2** The decaying tropical cloud belt in mid northern summer. The panels have the same format as the equatorial map shown in Plate 1.1. Each panel is the blue filter map for a particular day at the  $L_s$  indicated in the figure.

### 1.4.3 Cloud morphology of the tropical cloud belt

Clouds in the tropical cloud belt belong to two main cloud types. Most of the clouds observed during  $L_s$   $44^\circ$ ~ $111^\circ$  appear fibrous (see Fig. 1.3 (a)) and are similar to cirrus clouds on Earth [Houze, 1993]. However, the fraction of fibrous clouds decreases quickly after  $L_s$ ~ $134^\circ$ . Cloud patches composed of small puffy plumes (see Fig. 1.3 (b)) become dominant from mid to late northern summer. These clouds resemble cumulus clouds on Earth. They indicate atmospheric convection and

relatively weak horizontal winds [Houze, 1993]. Convective clouds are not limited to the main tropical cloud belt; they can be found at high latitudes and even near the polar cap (see Fig. 1.3 (c, d, and e)). Many high latitude convective clouds appear to be related to the main tropical cloud belt through cloud branches. Sometimes, the convective clouds organize into cloud streets with parallel rows (Fig. 1.3 (c, e)). Cloud streets on Earth usually occur in a convective boundary layer with vertical wind shear, and they could align either parallel or perpendicular to the wind [Houze, 1993]. Sometimes, the convective clouds organize into radiating patterns (see Fig. 1.3 (d)) that are similar to "actinae" on Earth [Houze, 1993].

In the Viking era, low latitude streak clouds (fibrous clouds) were observed more often during  $L_s$  45°~130°, while wave clouds and cloud streets (convective clouds) were mainly observed during  $L_s$  80°~130° [Kahn, 1984]. This indicates a change in cloud type in the tropical cloud belt and is consistent with the MOC observations. However, there are some differences. Convective clouds can still be observed in MOC images during  $L_s$  134°~150°, but few during the same period were observed in the Viking data [Kahn, 1984]. Low latitude streak clouds in the Viking era were also observed during  $L_s$  245°~360°, but few condensate clouds are observed in the MOC images during the same period of  $L_s$ .

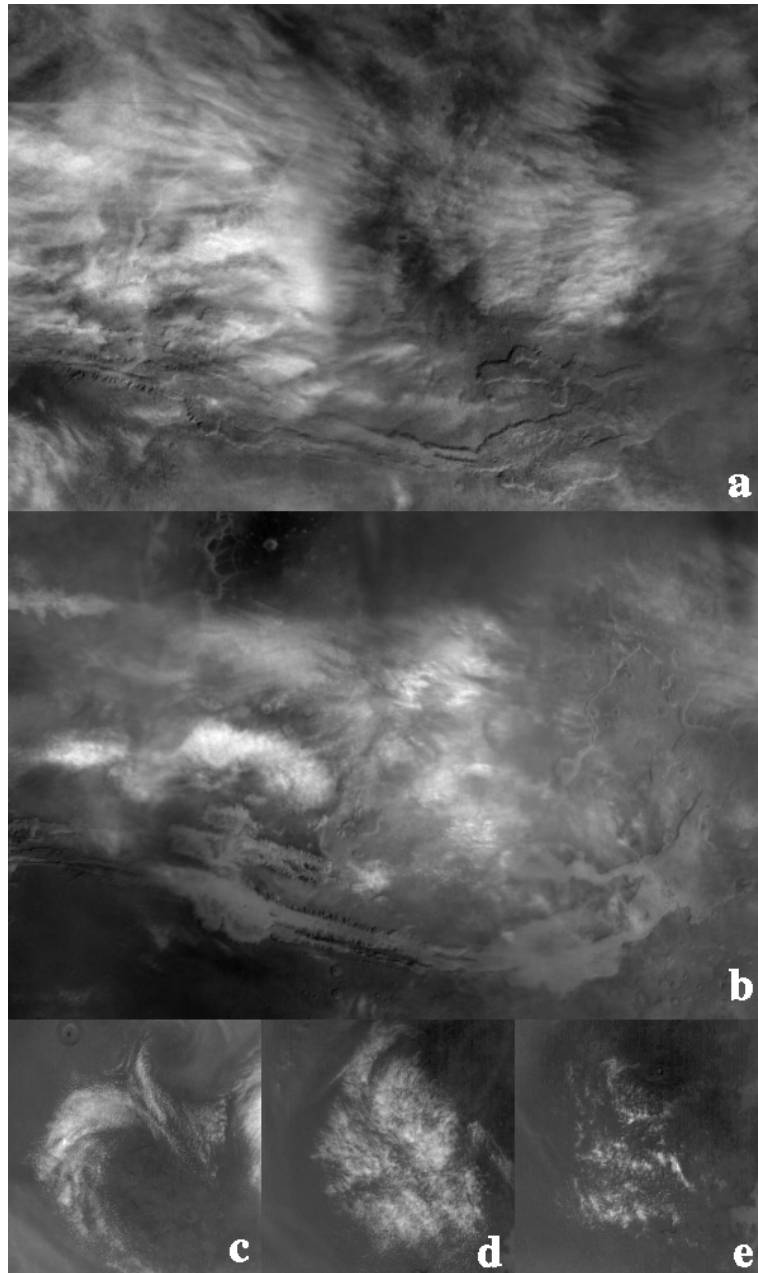


**Figure 1.3** (a) Fibrous clouds north of Valles Marineris around  $L_s \sim 101.2^\circ$ . (b) Convective clouds north of Valles Marineris around  $L_s \sim 149.8^\circ$ . Both (a) and (b) are cropped from the corresponding blue equatorial maps ( $0.1^\circ \times 0.1^\circ$ ), and are composed of  $600 \times 400$  pixels. (c) Cloud streets at  $\sim 53^\circ\text{N}$ ,  $20^\circ\text{W}$  around  $L_s \sim 134^\circ$ . This  $200 \times 200$  (pixel) image is cropped from global map swath m01-00017 (7.5km/pixel). (d) Actinae clouds at  $\sim 56^\circ\text{N}$ ,  $269^\circ\text{W}$  around  $L_s \sim 139^\circ$ . This  $200 \times 200$  (pixel) image is cropped from global map swath m01-01949 (7.5 km/pixel). (e) Cloud streets at

~53°N, 264°W around  $L_s \sim 144^\circ$ . This 200 % 200 (pixel) image is cropped from global map swath m01-03850 (7.5 km/pixel).

Large dust storms such as the mid northern fall cross-equatorial regional dust storms studied by Cantor et al. [2001] interact with the condensate clouds [Smith et al., 2001; Rodin and Clancy, 1999]. Right after these regional dust storms, few condensate clouds are observed in the low latitudes (see Fig. 1.1 (f)). This negative correlation between the dust and condensate is in contrast with that during the formation of the north polar hood. The disappearance of the condensate clouds here is perhaps because dust warms the atmosphere [Smith et al., 2001] or dust particles serve as nucleation sites for ice removal [Rodin and Clancy, 1999]. However, the decrease of condensate clouds is imbedded in the general decline of the tropical cloud belt, so the role played by dust is unclear.

#### **1.4.4 Aster clouds above the volcanoes**

Topographic clouds associated with the volcanoes have been known for a long time through telescopic and spacecraft observations [Martin et al., 1992; Snyder and Moroz, 1992], but only since MGS are daily synoptic observations possible. During mid to late northern summer, the clouds above the volcanoes sometimes take the form of rays around a central disk, like the flower. Some of the best examples are observed above Arsia Mons and are shown in Fig. 1.4. Shadows cast by the ray clouds suggest that they are sometimes 15 km or more above the surface. The rays are usually 200-500 km long and 20-50 km wide. Clouds with similar morphology are also observed on other volcanoes, but are usually less regular in shape. Sometimes the central disk is

missing, and sometimes the rays are parallel instead of radiating. The strong correlation of such clouds with the special topography of large volcanoes suggests that these clouds are related to the up-slope winds that are expected during daytime.

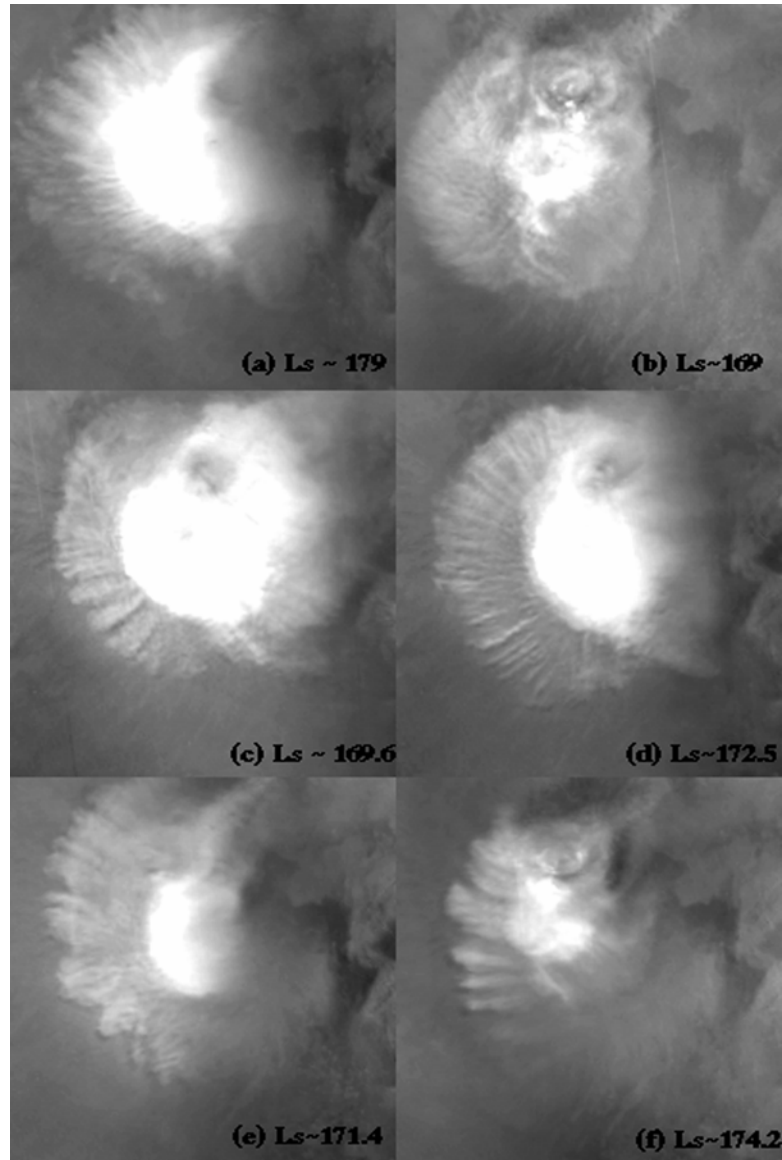


**Figure 1.4** Aster clouds, consisting of rays around a central disk, above Arsia Mons ( $\sim 9^{\circ}\text{S}$ ,  $120^{\circ}\text{W}$ ) in mid northern summer. Each panel has  $200 \times 200$  pixels and is cropped from the corresponding blue equatorial map ( $0.1^{\circ} \times 0.1^{\circ}$ ), simple cylindrical equidistant projection.

## 1.5 North polar clouds

The north polar hood develops from a series of storms that first appear in late northern summer (Plate 1.2). By early northern fall, the polar region is covered by circumpolar clouds. The polar hood grows south of  $\sim 60^\circ\text{N}$  after  $L_s \sim 185^\circ$  and retreats north of  $\sim 60^\circ\text{N}$  after  $L_s \sim 10^\circ$  (see Fig. 1.1). The north polar hood displays a stationary wave number two pattern (Fig. 1.1 (e–n)). Clouds push further south in Acidalia Planitia ( $\sim 30^\circ\text{W}$ ) and Utopia Planitia ( $\sim 250^\circ\text{W}$ ) than in other longitudes, and they can reach latitudes as low as  $\sim 35^\circ\text{N}$ . The north polar hood exhibited a wavy structure also during the Viking era [French et al., 1981], as indicated by the lee waves and streak clouds. The wavy structure shows a strong correlation with topography and agrees well with the GCM simulated winter quasi-stationary eddies [Barnes et al., 1996].

### 1.5.1 North polar hood formation ( $L_s 160^\circ\sim 185^\circ$ )

As the northern fall approaches, the north polar region enters a transitional period ( $L_s 160^\circ\sim 185^\circ$ ) characterized by widespread condensate clouds and dust storms (Plate 1.2 (b, c)). Cantor et al. [2001] documented the emergence of many local dust storms in late northern summer and the development of two regional dust storms that originated at  $L_s 163^\circ$  and  $183^\circ$  respectively. The  $270^\circ\text{--}0^\circ\text{--}90^\circ\text{W}$  sector is especially active during  $L_s 160^\circ\sim 185^\circ$ . Many storms originate here and move eastward as they develop. These storms are associated with fronts. Many fronts form spiral clouds, which are discussed in Section 4.4.

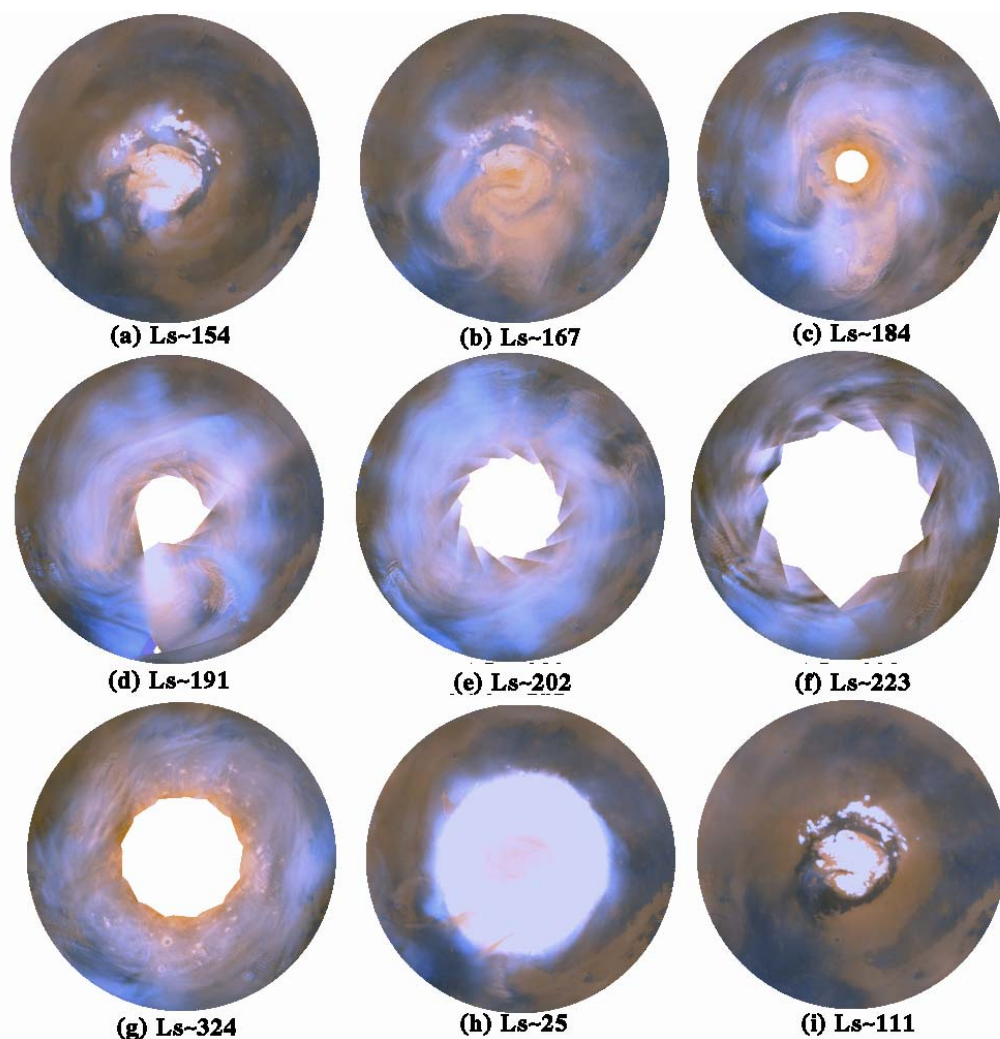


**Plate 1.2** Representative north polar stereographic maps ( $45^{\circ}\text{N}$ - $90^{\circ}\text{N}$ ,  $0.1^{\circ}$  %  $0.1^{\circ}$ ). The  $L_s$  is listed below each panel. The blank circular areas in the centers of the maps during the fall and winter are the areas inside the terminator circles, for which there are no data. The polar cap in (g) is larger than that in (h), but it appears darker because the stretches are different. The abrupt change in brightness north of the triangular area in (d) is related to missing data in one of the global map swaths.

The great increase in cloud cover during  $L_s$   $160^{\circ}$ - $185^{\circ}$  can be seen in Plate 1.3 (a), which shows the fraction of cloud-covered area between  $60^{\circ}\text{N}$  and  $75^{\circ}\text{N}$  as a function of  $L_s$  for three different criteria. (1) The green line represents pixels in the blue north polar map that are more than 75% brighter than the corresponding pixels in the

reference blue map. This criterion selects both condensate and dust clouds (total clouds). (2) The blue line represents pixels in the blue north polar cap that are 125% brighter than the reference blue map. This criterion selects thick condensate clouds. (3) The red line represents pixels in the red north polar cap that are 25% brighter than the reference red map. This criterion selects thick dust clouds. The corresponding areas selected by these criteria are highlighted by the corresponding colors in Plate 1.3 (c, d, and e) for the image shown in Plate 1.3 (b). The spiral dust storm in the image was studied by Cantor et al. [2001].

The sharp increase in the total clouds (the green line in Plate 1.2) around  $L_s \sim 163^\circ$  corresponds to the first regional dust storm described in Cantor et al. [2001]. By the time of the second regional storm ( $L_s \sim 183^\circ$ ), ~95% of the area between  $60^\circ\text{N}$  and  $75^\circ\text{N}$  was covered by clouds. Dust and condensate clouds that are especially thick will be selected both by criterion (2) and by criterion (3), so the sum of the red and blue areas is greater than the green area after  $L_s \sim 173^\circ$ . Although the  $L_s \sim 163^\circ$  regional storm induces an apparent increase in both the total clouds and the thick dust and condensate clouds (see Plate 1.3), the  $L_s \sim 183^\circ$  storm is mainly associated with an increase in the thick clouds because the total cloud cover is already large before  $L_s \sim 183^\circ$ . Between the  $L_s \sim 163^\circ$  and  $183^\circ$  regional storms, the total clouds are significantly greater than the sum of the red and blue clouds, indicating the presence of haze, which does not register in criteria (2) and (3).

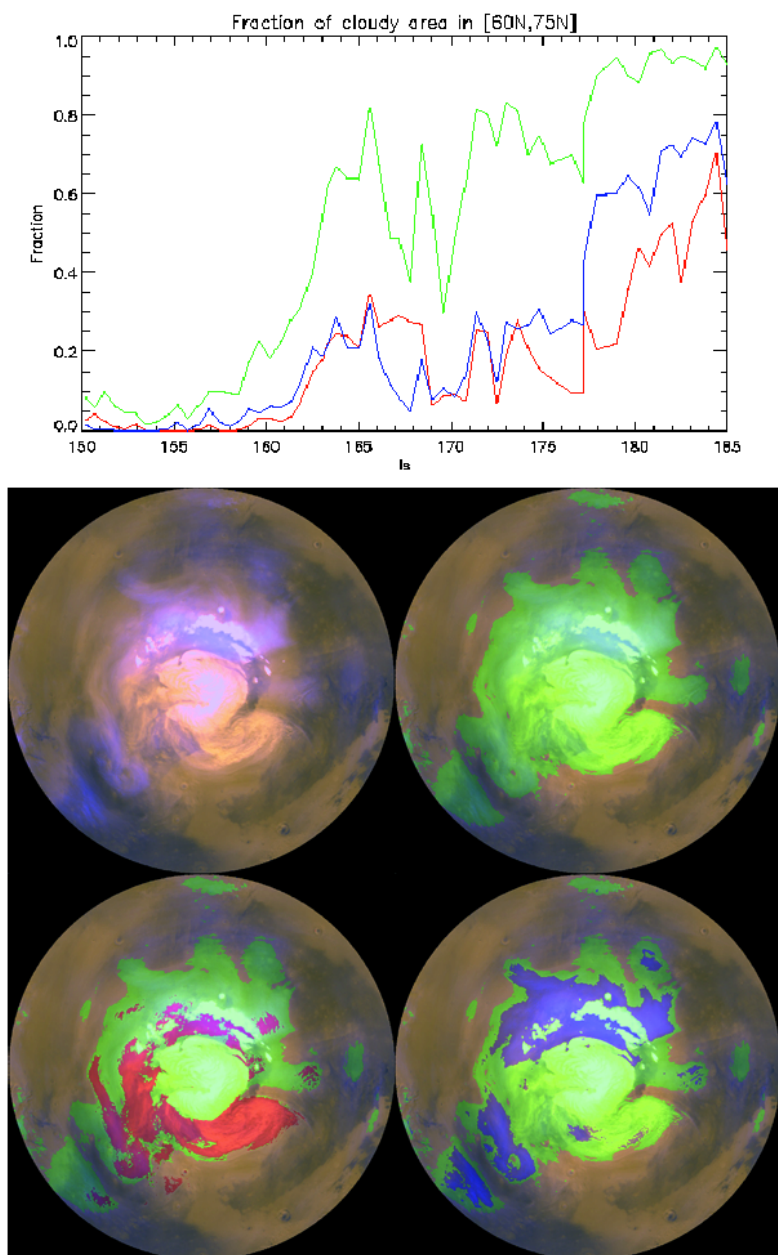


**Plate 1.3** (a) The fraction of cloud covered area between 60°N and 75°N as a function of Ls for three different criteria used to identify clouds. (b) North polar stereographic map (45°N-90°N) at  $L_s \sim 164^\circ$ . (c) The green area highlights the total clouds including both the dust and the condensate clouds. (d) The red area highlights dust clouds. (e) The blue highlights condensate clouds. See text for details.

## 1.5.2 North polar streak clouds

The polar hood contains a wide range of cloud types: condensate and dust hazes, streak clouds, dust storms, clouds associated with frontal systems and lee waves (Plate 1.2 (c-g)). The presence of these clouds is consistent with the low atmospheric temperature, large temperature gradient between the mid and high latitudes, high near-surface static stability, strong wind speed and strong wind shear in the fall and winter [Kahn, 1984; Haberle et al., 1993].

Streak clouds appear to be the most characteristic clouds in the polar hood. Streaks can occur in both condensate clouds and dust clouds [Kahn, 1984]. They usually appear as long curves that can be traced in several consecutive global map swaths for thousands of kilometers. The time interval between the consecutive swaths is about two hours. The fact that coherent streaks span several swaths suggests a lifetime of several hours. The streak clouds are usually associated with strong winds [Kahn, 1984]. Strong winds can advect particles great distances downwind and give a stringy appearance to the clouds [Houze, 1993]. The number of streaks in the north polar maps appear to increase from early to mid northern fall and decrease during the northern winter (see Plate 1.2 (d-g)), although the terminator circles near  $L_s \sim 270^\circ$  obscure a large area. In comparison, Kahn [1984] observed significant decrease of streak clouds during the fall for the Viking era, but this could be related to the non-uniform image coverage at that time.

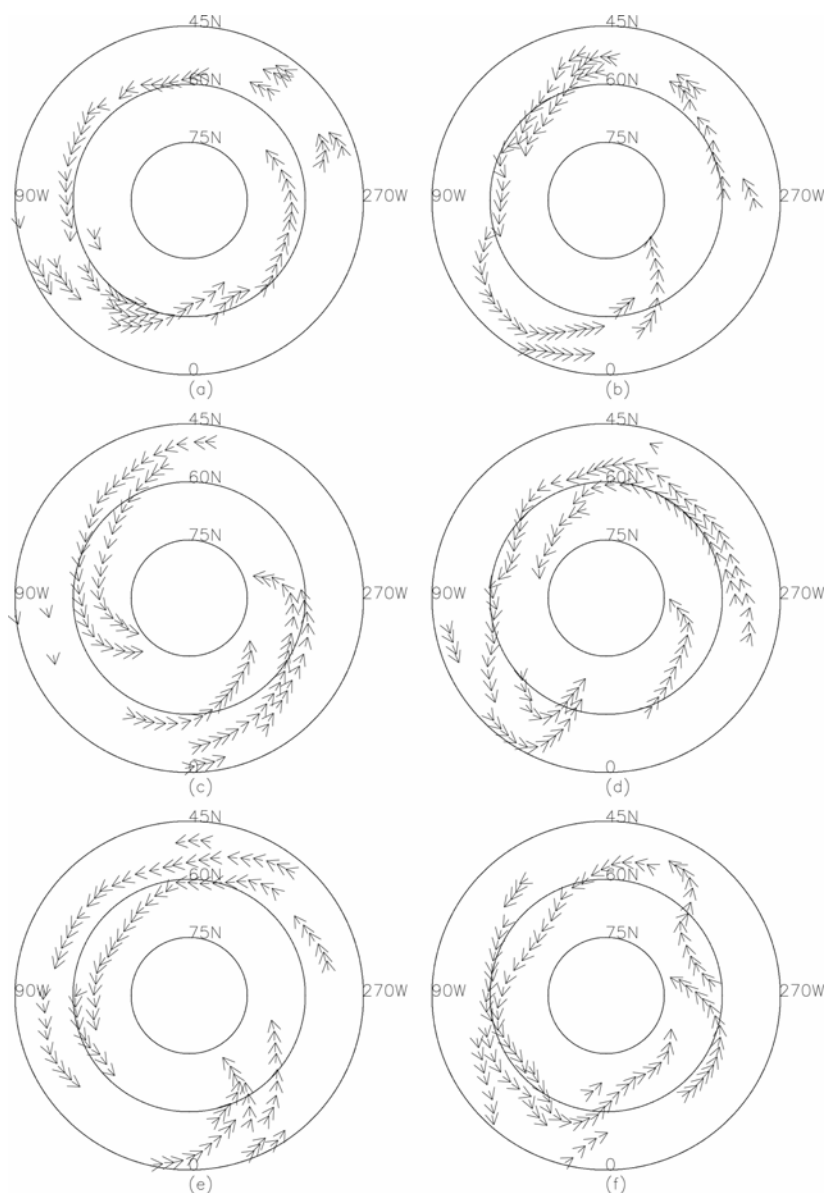


**Figure 1.5** Streaks traced in six consecutive north polar maps (a)-(f) during Ls 202°~205. The arrows point in the wind direction indicated by the lee waves. The length of the arrow is arbitrary.

The streaks observed in the north polar maps often appear to spiral counterclockwise in towards the pole, especially between mid northern fall and mid northern winter, and they seem to delineate a polar vortex that changes daily. Figure 1.5 (a-f) show the streaks traced in six consecutive north polar maps during L<sub>s</sub> 202°~205°. The arrows in

the plot point in the wind directions indicated by the coexistent lee waves. Poleward converging counterclockwise streaks in the fall and winter are consistent with the low-level poleward meridional circulation in high latitudes simulated by GCM's [Haberle et al., 1993]. The streaks usually dip to lower latitudes at Acidalia Planitia, Utopia Planitia or Arcadia Planitia. These areas have been simulated to be the wintertime storm zones on Mars [Hollingsworth et al., 1996]. Cantor et al. [2001] describe three cross-equatorial regional dust storm events during mid northern fall ( $L_s$  210°~230°); another such storm is observed by MOC in mid northern winter ( $L_s$  ~320°). All these storms seem to originate from the northern storm zones and get entrained into the lower branch of the Hadley circulation through the western boundary jets [Cantor et al., 2001]. Each regional dust storm appears to be composed of a series of storm centers that continuously push southward as they replenish dust to the atmosphere [Cantor et al., 2001].

As the amount of streak clouds decreases during the winter, the main clouds in the north polar hood change into haze and cap edge dust storms by  $L_s$  ~0°. The polar hood retreats with the polar cap to high latitudes. The recession of the north polar cap and the circumpolar dust activities are described in James and Cantor [2001]. Most of the areas outside the polar cap appear clear. Cap edge dust storms occur preferably in the 270°-0°-90°W sector during the spring and summer [James and Cantor, 2001]. Individual global map swaths often show cloud activity on the 0200 LT (2AM local time) side of the polar cap [James and Cantor, 2001]. These clouds do not show clearly in the daily north polar map because the 0200 LT side of one swath overlaps with the 1400 LT (2PM local time) side of another swath. More weight is assigned to

the pixels on the 1400 LT side than those on the 0200 LT side when the swaths are merged to make daily north polar maps (see Section 2 and Section 5.2).

### 1.5.3 North polar lee waves

Lee waves are frequently observed in the polar region during fall and winter. They are associated with stationary gravity waves on the lee side of obstacles [Kahn, 1984]. On Earth, lee waves preferably occur in a layer with rapidly decreasing static stability and increasing wind speed with height [Houze, 1993]. The high near-surface static stability and strong wind shear during the fall and winter [Haberle et al., 1993] could provide good conditions for Martian lee wave formation. The observed wavelengths of the lee waves range from ~15 km to ~50 km. Waves with shorter wavelengths cannot be recognized properly because they are not well resolved at 7.5 km/pixel. Lee waves usually appear superimposed on the haze and streak clouds. Examples can be seen near ~45°W, 50°N in Plate 1.2 (e, f).

The spatial distribution of lee waves in the north polar maps (45°N-90°N) is shown in Fig. 1.6 (a). More lee waves are observed between 45°N and 60°N than between 60°N and 90°N. This is largely because no MOC data exist within the terminator circles (see Plate 1.2 (e, f)), which maximize at winter solstice. For comparison, MOLA observed many wave clouds with sloping fronts during the polar night within the terminator circles [Pettengill and Ford, 2001]. While lee waves seem widespread, many of them cluster around topographic features such as fossaes, mensaes and large craters. In late northern summer, lee waves suddenly increase in the 0°-90°-180°W hemisphere, then quickly spread to the opposite hemisphere (not shown).

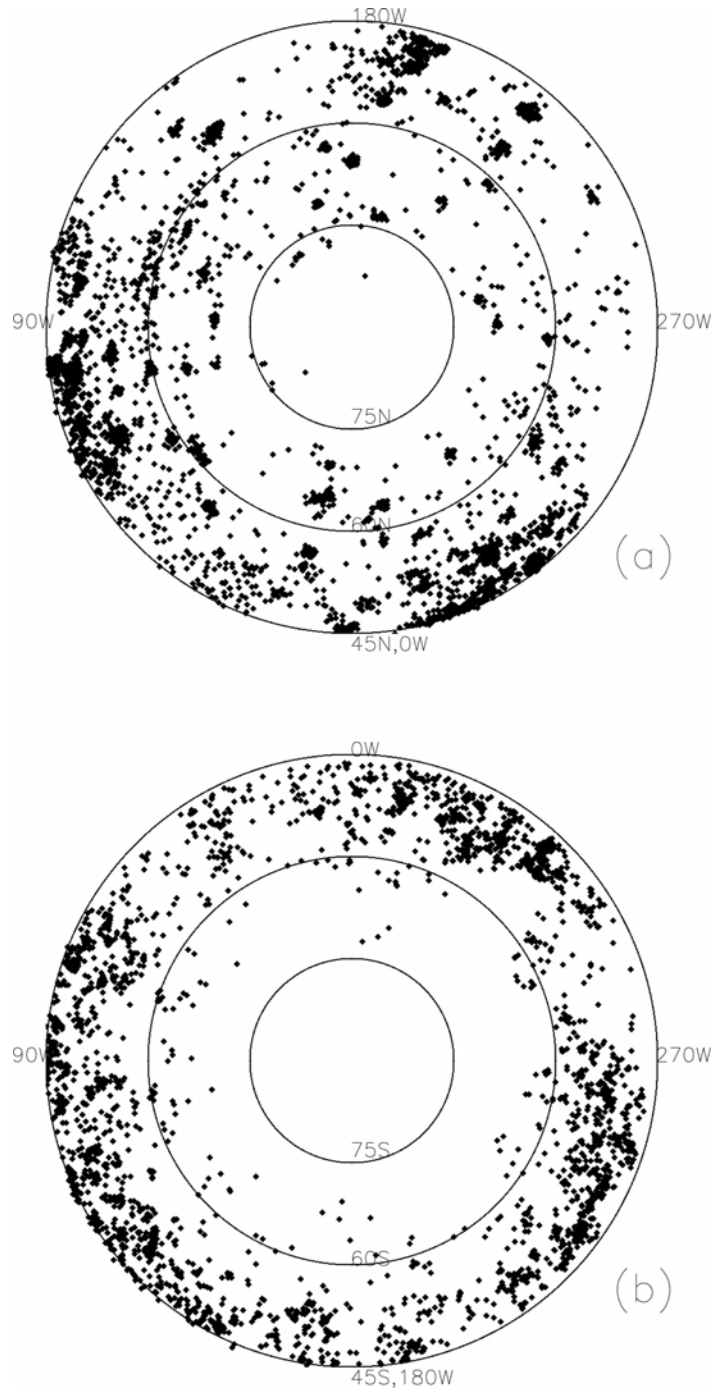


**Figure 1.6** Spatial distribution of lee waves in the (a) north polar maps and (b) south polar maps Each dot represents the position of an observed lee wave.

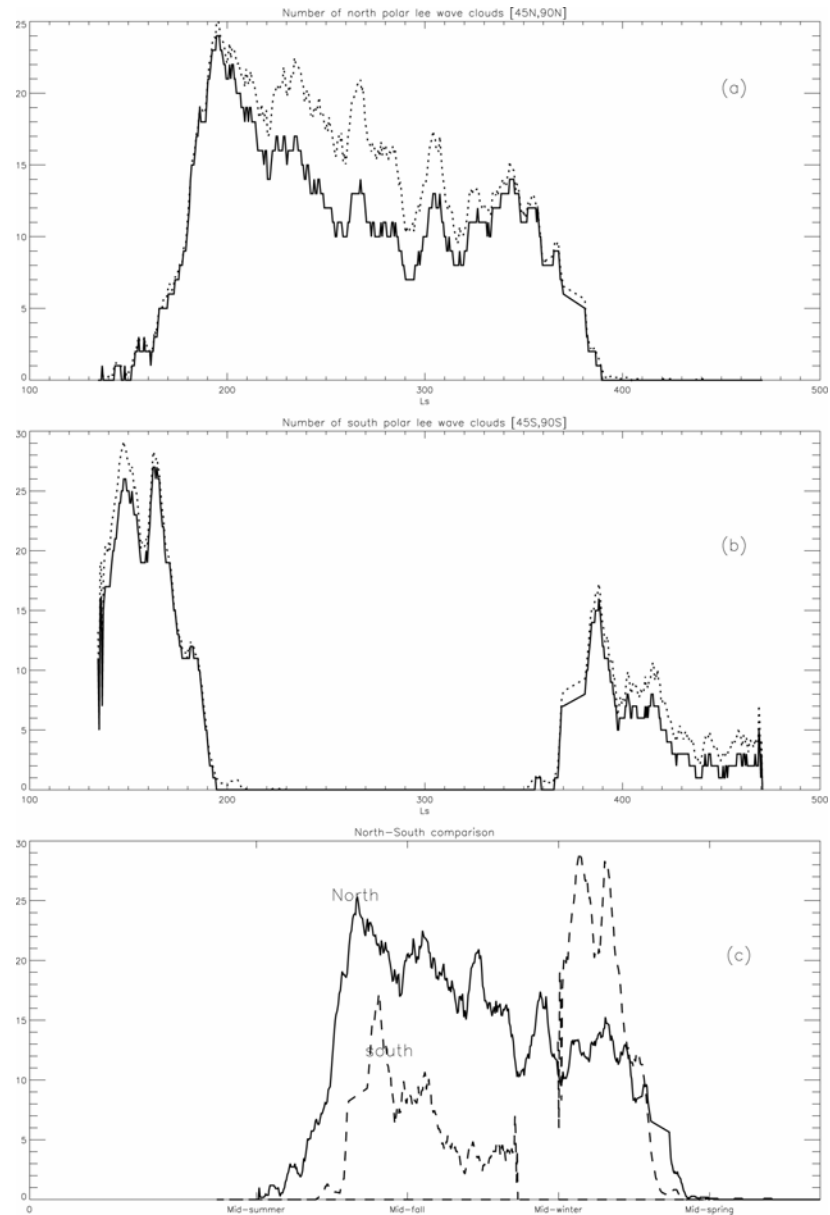


**Figure 1.7** Temporal distribution of lee waves in the (a) north polar and (b) south polar maps. The solid lines in (a) and (b) are the number of lee waves observed in the polar maps as a function of  $L_s$ . The dotted lines in (a) and (b) are from the solid lines scaled by the area outside the terminator circles. (c) The solid line is the scaled time sequence for the north polar region, the same as the dotted line in (a). The dashed line is the scaled time sequence for the south polar region with the  $L_s$  shifted by  $180^\circ$ .

The number of lee waves observed in the north polar maps as a function of  $L_s$  is shown in Fig. 1.7 (a). An eleven-day running mean has been applied to the original daily data to reduce high frequency variation (the solid line). To minimize the effect that no observations exist within the terminator circles which maximize at the winter solstice, the numbers represented by the solid line are then scaled by the area outside the terminator circles (the dotted line), so the number density is proportional to the dotted line. Lee waves sharply increase around  $L_s \sim 170^\circ$ , peak around  $L_s \sim 195^\circ$ , and quickly disappear after  $L_s \sim 20^\circ$  of the second year. The decreasing trend from the early fall to the late winter is probably related to the decreasing amount of water vapor. Significant decrease of lee waves during the fall and winter was documented for the Viking era, although the high latitude coverage near the winter solstice was poor at that time [Kahn, 1984]. Several summertime north polar lee waves were observed in the Viking images [Kahn, 1984], but we observe no summertime lee waves in the MGS north polar maps. This may not necessarily reflect interannual variability, because most Viking images have resolution better than 1.5 km/pixel [Snyder, 1977], and the MOC global map swaths have a resolution of 7.5 km/pixel.

#### **1.5.4 Spiral clouds**

Viking spacecraft imaged a spiral cloud around  $78^\circ\text{N}$ ,  $150^\circ\text{W}$  in early northern summer [Hunt and James, 1979; Gierasch et al., 1979]. Hubble Space Telescope (HST) also observed such a cloud around  $65^\circ\text{N}$ ,  $85^\circ\text{W}$  a few days before our observational period (NASA HST Press release NO. STSc1-PR99-22, May 19, 1999). These two pre-MGS spiral clouds were composed mainly of water ice and had cloud-free centers. However, the spiral clouds observed by MOC are mainly composed of

dust, and many of them have associated spiral arms or fronts (see Plate 1.4). Some of them have associated condensate clouds during their developing phase (see Plate 1.5).

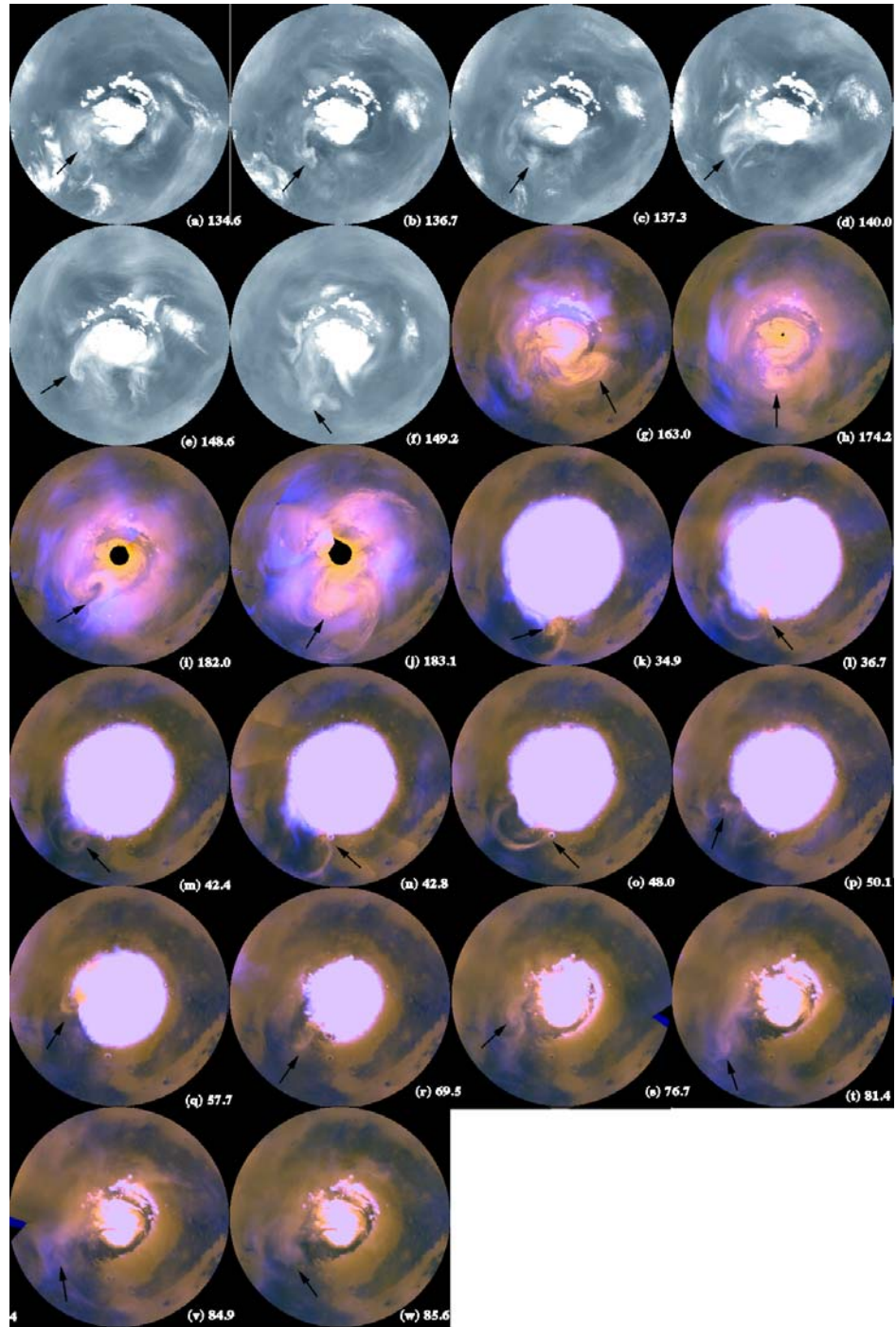


**Plate 1.4** Spiral clouds observed by MOC during the observational period ( $L_s$  134°~360°~111°). All the spiral clouds occur in the north polar region from mid spring to early fall. The panels are north polar stereographic maps (45°N-90°N, 0.1° % 0.1°) with the corresponding  $L_s$  shown below them.

All the spiral clouds observed during our observational period are summarized in Plate 1.4. Plates 1.4 (g) and (f) were discussed in Cantor et al. [2001], and Plates 1.4 (k, m, o) were discussed in James and Cantor [2002]. All the spiral clouds observed by MGS occur in the northern high latitudes from mid northern spring to early northern fall ( $L_s$  30°~185°). The fact that no spiral clouds are observed in the south indicates different conditions of the two polar regions during the corresponding season (see Section 5). The spiral cloud in Plate 1.4 (g) lies in the 270°-360°W sector, and all the others lie in the 0°-90°W sector. This preference for the 0°-90°W sector may be related to the special local topography or thermal inertia. All of the 22 storms in Plate 4 spiral inward in the counterclockwise direction. Developing baroclinic disturbances on Earth have the same sense of rotation in the northern hemisphere. However, the center of the spiral (“comma-cloud,” Houze, 1993) is usually to the north, where the cold front (on the western side) and warm front (on the eastern side) merge to form an occluded front. Some of the Martian storms have this property (e.g. Plate 1.4 (f)). In other Martian storms, the center of the spiral is to the south and appears to belong to the putative cold front (e.g. Plate 1.5 (a-c)). The large temperature gradient between the polar cap and the circumpolar surface during the spring and summer [Barnes et al., 1993; James et al., 1999] is consistent with the occurrence of spiral clouds.

The location of the condensate cloud in relation to the spiral dust clouds provides further support for the baroclinic disturbance hypothesis. Plate 1.5 shows two

examples of cyclogenesis observed by MOC. Each leads to a regional spiral dust storm that is described in detail by Cantor et al. [2001]. The first row in Plate 1.5 shows three consecutive views (spanning 4 hours) of a storm around  $L_s \sim 163^\circ$ . The spiral arm south of the cap sweeps eastward at  $\sim 20$  m/s and approaches the dust front at  $\sim 315^\circ$ W. Bluish condensate clouds can be seen just north of the dust front. Our interpretation is that the relatively warm, moist air south of the dust front is forced upward as it pushes northward over the colder polar air. Water vapor condenses above the condensation level and produces the observed condensate clouds. The dust front and the associated condensate cloud at  $\sim 315^\circ$ W are analogous to a terrestrial warm front. The fast-moving spiral arm is analogous to a terrestrial cold front, but it has more curvature and a hook shape.

The second row shows a storm around  $L_s \sim 182^\circ$ . Two dust arms appear to be connected by a cyclonic spiral cloud to the north. The center of the spiral cloud moves eastward at  $\sim 15$  m/s. The northern parts of the two dust arms appear to be colliding (Plate 1.5 (f, g)). The southern tips of the two arms sweep eastward at  $\sim 20$  m/s. Condensate clouds can be seen just east of the leading (eastern) dust arm in the  $0^\circ$ - $45^\circ$ W sector. This development process resembles the typical baroclinic storm genesis on the Earth [Leovy et al., 1972], with the eastern arm being a warm front, the western arm a cold front, and the spiral cloud an occluded front.

The spiral clouds from mid to late spring tend to occur right at the cap edge, and they sometimes have associated fronts that extend southward (Plate 1.4). The spiral clouds from early to mid summer usually lie south of the cap edge, and they have

associated fronts that extend northward toward the cap (Plate 1.4). Interestingly, the associated front in Plate 1.4 (c) has a wavy nature to it, with a wavelength of  $\sim 400\text{km}$ , with additional spiral clouds trying to develop behind the main spiral cloud. The observed spiral clouds from late summer to early fall are well developed and larger in size (Plate 1.4). Condensate clouds are involved in these storms, and the storm development process resembles the baroclinic cyclogenesis on Earth (Plate 1.5).

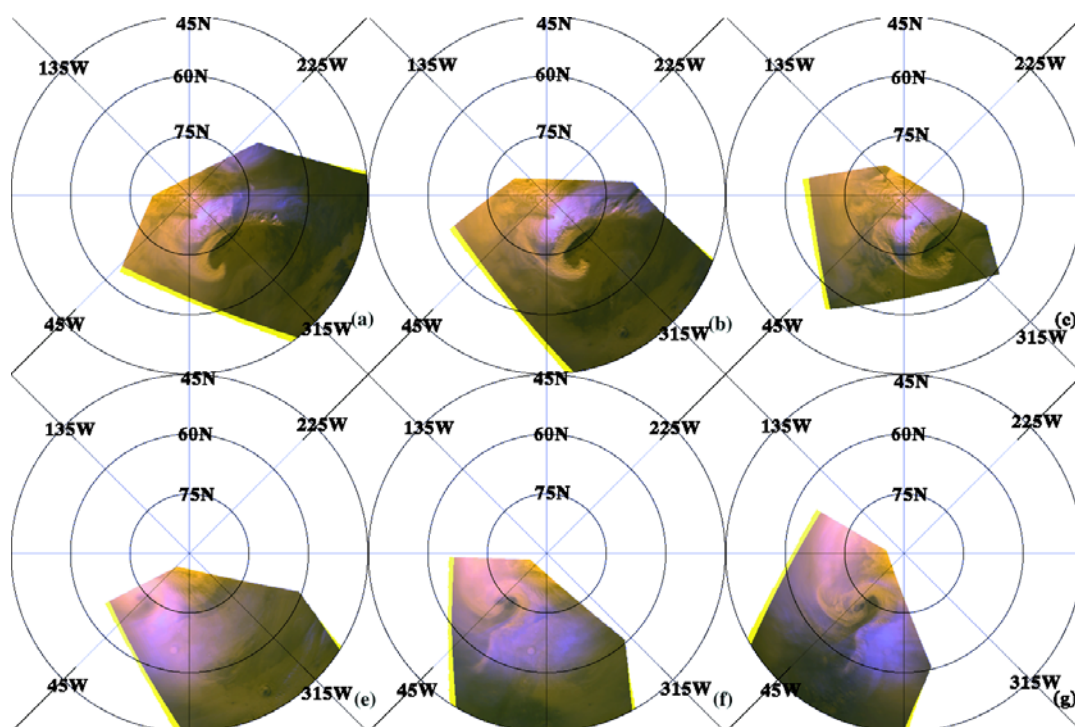


**Plate 1.5** Spiral clouds in the north polar region during the transitional period ( $L_s$   $160^\circ\sim 185^\circ$ ). Note the condensate clouds associated with the dust fronts. (a)-(c) Consecutive two-hour sequence at  $L_s \sim 163^\circ$ . (e)-(g) Consecutive two-hour interval sequence at  $L_s \sim 182^\circ$ .

## 1.6 South polar clouds

As in the north, the south polar hood develops from a series of storms that first appear in late southern summer (Plate 1.6). By southern fall equinox, the south polar

region is covered by circumpolar clouds. The south polar cap and hood grow northward from  $\sim 60^{\circ}\text{S}$  to  $\sim 45^{\circ}\text{S}$  during  $L_s$   $21^{\circ}\sim 111^{\circ}$ , and they retreat southward from  $\sim 45^{\circ}\text{S}$  to  $\sim 60^{\circ}\text{S}$  during  $L_s$   $134^{\circ}\sim 197^{\circ}$  (see Fig. 1.1). This result suggests faster retreat than growth in the latitudinal range from  $45^{\circ}\text{S}$  to  $60^{\circ}\text{S}$ .

### **1.6.1 Development of the south polar hood**

The south polar hood begins to develop around  $L_s \sim 340^{\circ}$ . It evolves through two distinct stormy periods in late southern summer, and finally becomes circumpolar around the southern fall equinox (Plate 1.6 (g-f)). The development of the south polar hood is shown in Fig. 1.8 as the fraction of cloud-covered area between  $70^{\circ}\text{S}$  and  $80^{\circ}\text{S}$ . The cloud-covered area is defined by the pixels in the red south polar map that are more than 75% brighter than the corresponding pixels in the reference red map. This criterion is different from the one used in the north, because different stretch was applied for the north and south polar maps. Both dust and condensate clouds can satisfy this criterion and are included in Fig. 1.8. The first stormy period spans  $L_s$   $340^{\circ}\sim 345^{\circ}$  (Fig. 1.8 and Plate 1.6 (g)). The second stormy period starts from  $L_s \sim 352^{\circ}$  (Fig. 1.8 and Plate 1.6 (h)), and becomes circumpolar around  $L_s \sim 0^{\circ}$ . The cloud-covered area then decreases before additional dust storms occur in southern fall.

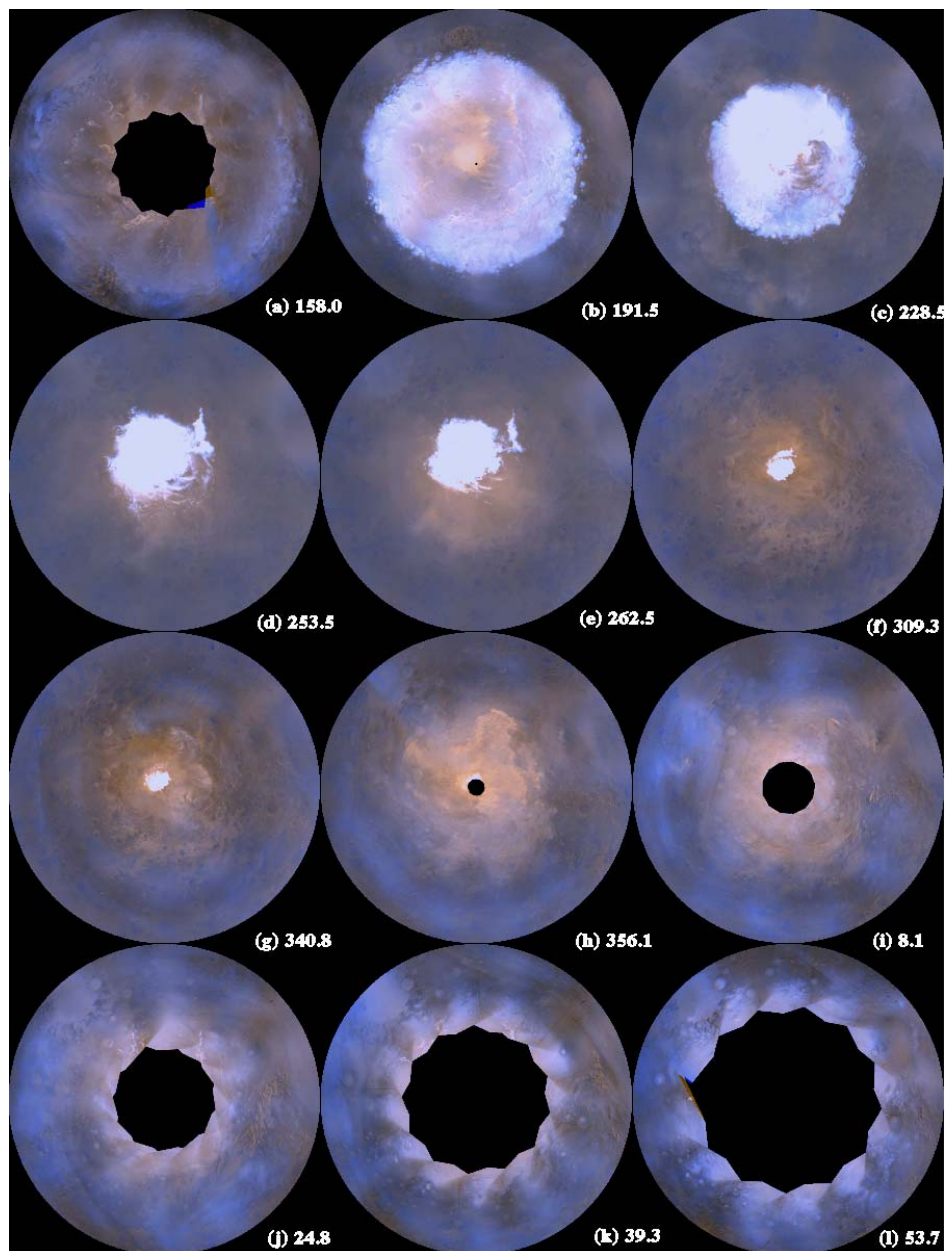


**Plate 1.6** Representative south polar stereographic maps ( $45^{\circ}\text{S}$ - $90^{\circ}\text{S}$ ,  $0.1^{\circ} \times 0.1^{\circ}$ ).  $L_s$  is indicated below each panel. The blank circular areas at the centers of the maps during the fall and winter are the areas inside the terminator circles. The polar cap in (a) is larger than that in (b), but it appears darker because the stretches are different.

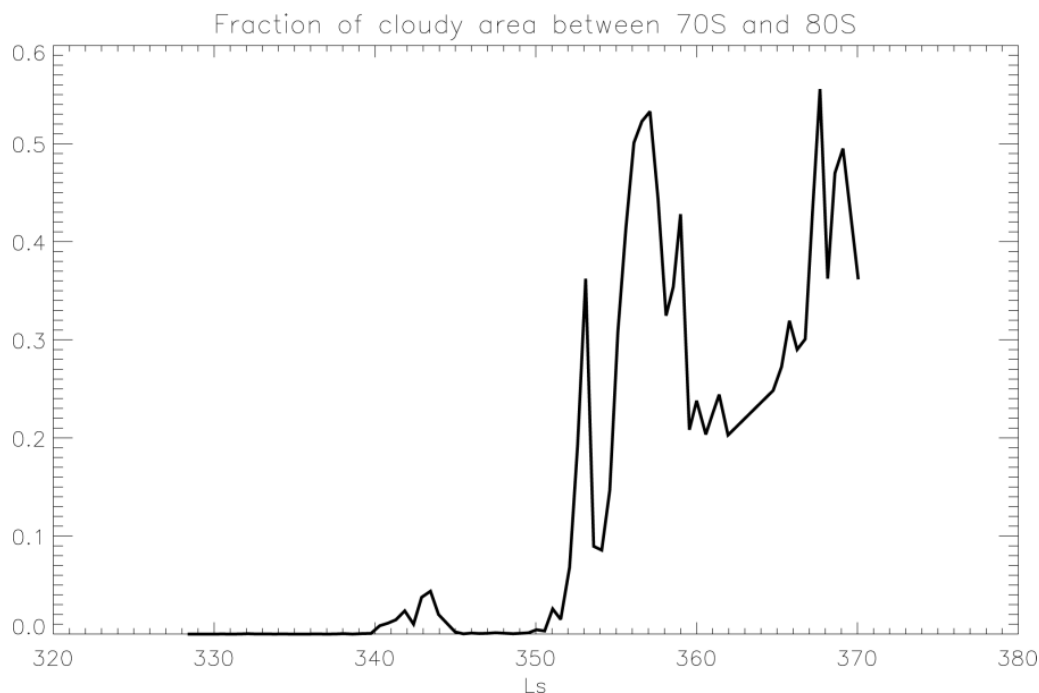


**Figure 1.8** Fraction of cloud covered area within 70°S and 80°S as a function of Ls.

The timing of these storms resembles the north polar hood development during the transitional period  $L_s$  160°~180°, where two regional dust storms precede the formation of the north polar hood. However, the southern dust storms are much smaller in size, and appear to involve few condensate clouds. Furthermore, none of the southern storms appear to display the characteristic fronts and spiral structures of the baroclinic storms seen in the north. Baroclinic instability usually requires large temperature contrast. Since the residual south polar cap is very small (see Plate 1.6 (g)) it probably does not serve as a sustaining source of cold air.

Although the types of clouds in the winter are similar in the south polar region and the north polar region (compare Plate 1.2 (g) with Plate 1.6 (a)), clouds in the south polar region during the fall appear much thinner (compare Plate 1.2 (e, f) with Plate

1.6 (j, k)). Faint streak clouds surrounding the polar region can be seen in the south polar hood (Plate 1.6 (j-l)), but the number of streaks appears much less than that in the north polar region during the northern fall. Lack of water vapor in the southern hemisphere [Jakosky and Farmer, 1982] could contribute to this discrepancy.

### **1.6.2 South polar clouds from mid winter to mid summer**

The dominant clouds in the south polar hood change from streak clouds (Plate 1.6 (a)) to haze and cap edge dust storms (Plate 1.6 (b)) around southern spring equinox. Cantor et al. [2001] documented poleward recession of the cap edge dust storms before  $L_s \sim 274^\circ$ . Kahn [1984] documented the same phenomenon for the Viking era. Before mid southern spring, the south polar cap recedes symmetrically [James et al., 2001], and the local dust storms observed by MOC are evenly distributed around the polar cap [Cantor et al., 2001]. However, after mid southern spring, the south polar cap recedes asymmetrically [James et al., 2001], and the cap edge dust storms tend to occur in the  $90^\circ$ - $180^\circ$ - $270^\circ$ W sector (Plate 1.6 (d, e)) [Cantor et al., 2001]. A regional dust storm in the southern high latitudes observed by MOC during 1999 occurred at the beginning of the asymmetric recession phase around  $L_s \sim 234^\circ$  [Cantor et al., 2001]. These storms have settled by  $L_s \sim 274^\circ$ .

Clearer conditions (Plate 1.6 (f)) after the southern summer solstice last until  $L_s \sim 340^\circ$ . However, summer is not cloud-free. Individual global map swaths show that arc-shaped clouds often occur near the terminator (the 0200 LT side) during the summer (Fig. 1.9). However, the early afternoon side (the 1400 LT side) is generally calm. Small dust storms occur only occasionally, and the exposed polar layered terrain

appears to be a preferred area for them. The clouds near the terminator usually do not show clearly in the daily south polar map because the cloudy 0200 LT side of one image is merged with the 1400 LT side of another image.

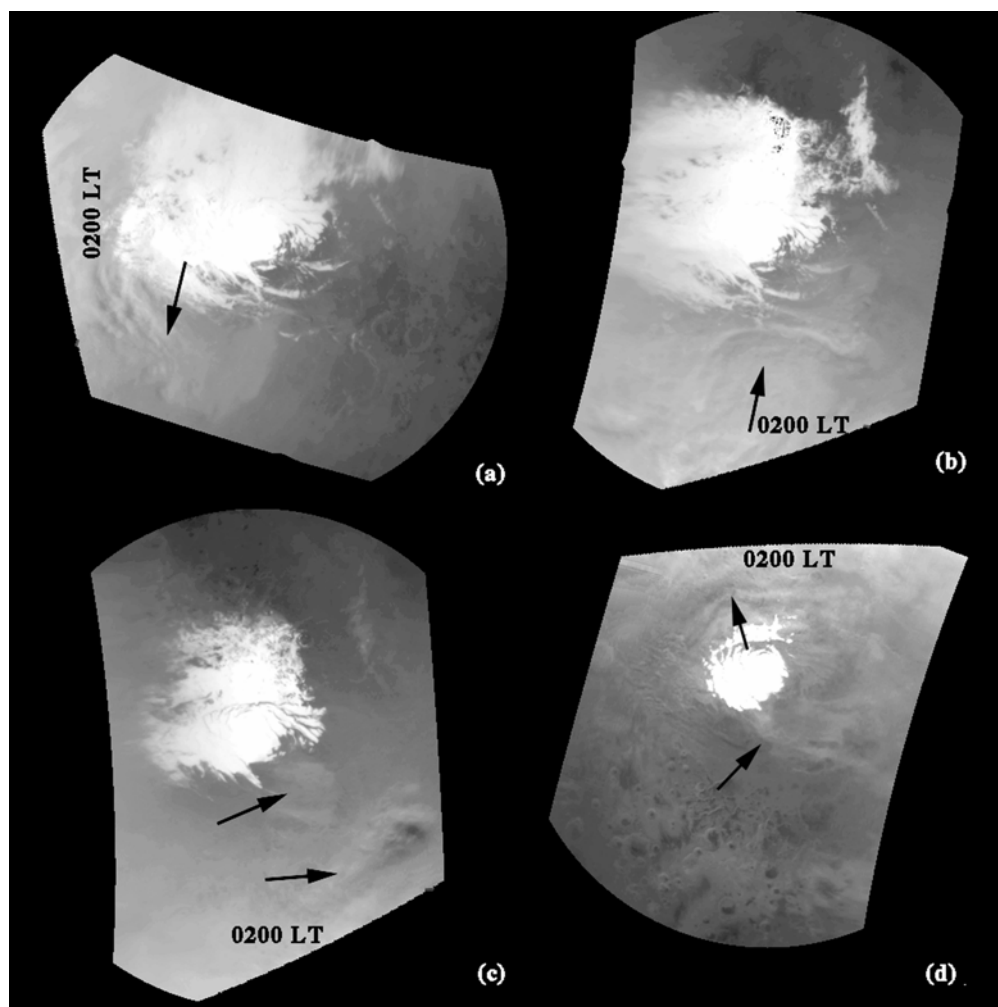


**Figure 1.9** Dust activity in the south polar region in the southern summer. Each image is a stereographic projected red global map swath ( $65^{\circ}\text{S}$ - $90^{\circ}\text{S}$ ,  $0.1^{\circ}$  %  $0.1^{\circ}$ ). Note the dust activity near the terminator (0200 LT). (a) from m10-00784 at  $L_s \sim 258^{\circ}$ . (b) from m10-00892 at  $L_s \sim 259^{\circ}$ . (c) from m11-00687 at  $L_s \sim 276^{\circ}$ . (d) from m12-02041 at  $L_s \sim 304.5^{\circ}$ .

### 1.6.3 South polar lee waves

Despite of the general lack of condensate clouds in the southern hemisphere, many lee waves are still observed in the south polar region. They preferably lie around the south polar cap during the fall and winter. Their spatial distribution is shown in Fig. 1.6 (b). As in the north polar region, more lee waves are observed between 45°S and 60°S largely because of the lack of data within the terminator circles. The observed lee waves are roughly evenly distributed except in Hellas and Argyre. The lack of lee waves in these basins could be related to their relatively flat bottom topographies and compressional heating of the air. There are 2998 lee waves observed in the south polar region, and 4573 lee waves observed in the north polar region. The fact that more lee waves exist in the north polar region is consistent with more water vapor in the northern hemisphere [Jakosky and Farmer, 1982].

The number of south polar lee waves as a function of  $L_s$  is shown in Fig. 1.7 (b). To facilitate comparison in Fig. 1.7 (c), the scaled time sequence for the south polar region (the dotted line in Fig. 1.7 (b)) has been shifted by  $180^\circ L_s$  (the dashed line in Fig. 1.7 (c)) and overplotted with the original scaled time sequence for the north polar region (the solid line in Fig. 1.7 (c)). The number of south polar lee waves in the second Martian year suddenly increases around  $L_s \sim 5^\circ$  and peaks around  $L_s \sim 30^\circ$ . These events are about  $15^\circ$ - $25^\circ$  of  $L_s$  later in the season than their northern counterparts, and are consistent with the scarceness of water vapor in the south polar region. The number of south polar lee waves then decreases from mid southern fall to the end of our observational period  $L_s \sim 111^\circ$ . Interestingly, the number of south polar

lee waves in the first Martian year shows another set of sharp peaks around  $L_s \sim 150^\circ$  and  $160^\circ$  respectively. These peaks are not only larger than the early fall peak in the south polar region, but they are also larger than the early fall peak in the north polar region. Due to the large extent of the seasonal south polar cap, some cap edge lee waves are observed at latitudes lower than  $45^\circ\text{S}$  in the equatorial maps, especially from mid fall to mid winter. These low latitude lee waves were not included in Fig. 1.7. Further study is needed to see how they would influence the north-south difference shown in Fig. 1.7 (c) and to understand the global distribution of lee waves.

## 1.7 Conclusion

In this study, we have processed MGS MOC global map swaths taken from May 1999 ( $L_s \sim 134^\circ$ ) to January 2001 ( $L_s \sim 111^\circ$ ). We have made Mars daily global maps from these data for the roughly one Martian year period and studied the cloud distribution. The maps show the evolution of the tropical cloud belt and the north and south polar hoods, and reveal the similarities and differences between the two polar hoods, including dust storms, streak clouds and lee waves. We describe a new type of “aster” cloud above the volcanoes, and we show the relation between the condensate and dust clouds in the spiral storms in the north polar region.

The tropical cloud belt quickly disintegrates during  $L_s 134^\circ\sim 149^\circ$  of the first Martian year. Only the clouds associated with the volcanoes exist in the low latitudes during the northern fall and winter. The tropical cloud belt begins to develop around  $L_s \sim 44^\circ$  of the second Martian year and becomes longitudinally continuous by  $L_s 57^\circ\sim 70^\circ$ . The cloud types change from convective clouds in mid northern summer to

fibrous clouds in mid northern spring/early northern summer. The decaying phase and the developing phase of the cloud belt are non-uniform in longitude. The general behavior of the tropical cloud belt observed by MGS is similar to that derived for the Viking era [Kahn, 1984; Tamppari et al., 2000], but differences in the developing and decaying phases exist.

A new “aster” cloud pattern, consisting of rays around a central disk, is observed above the volcanoes in mid northern summer. Such clouds can be observed on all the main volcanoes, though they are best shown above Arsia Mons. Shadows indicate that rays are sometimes ~15 km or more above the surface. The time when such clouds are observed and the morphology of the clouds indicate that they form under weak atmospheric static stability and weak large-scale background flow, and they are probably related to the local upslope winds associated with the volcanoes.

Following the observations by Viking and Hubble Space Telescope, MGS also observed spiral clouds. All the spiral clouds observed up to now occur in high northern latitudes from mid northern spring to early northern fall. The spiral clouds observed by MGS are different from the previous ones in that they are mainly composed of dust instead of water ice, and they sometimes have associated fronts or spiral arms. The dust clouds and condensate clouds occur in distinctly different parts of the spiral structure, supporting baroclinicity as the mechanism for the storm development. Baroclinic fronts and spiral clouds occur less frequently in the south, perhaps because the small residual south polar cap cannot supply enough cold air.

Both the north polar hood and the south polar hood begin to develop in late summer about  $20^\circ L_s$  before the equinoxes. They both experience two stormy periods before the formation of the circumpolar clouds in early fall. However, there are significant differences between the two polar hoods. Condensate clouds appear common during the development of the north polar hood, but they seem rare during the development of the south polar hood. A wavenumber two stationary wave structure shows clearly in the north but not in the south. Perhaps because of the low abundance of water vapor in the south, streak clouds and lee wave clouds are less abundant in the south than in the north. In both polar regions, lee waves are observed mainly in the fall and winter, and the number of lee waves shows a peak in early fall. However, the temporal distributions for the northern and southern lee waves are quite different during this year. The south polar lee waves emerge about  $15^\circ$ - $25^\circ L_s$  later than the north polar lee waves, and they show the largest peak in late winter.

## **1.8 Acknowledgments**

This work is supported by the Mars Global Surveyor project and by NASA grant number NAG5-11288. We would like to thank the USGS astrogeology team for providing us with an early version of the software for calculating the geometry backplanes. We thank Shawn Ewald for testing the code for mosiacing the daily global maps. We thank Arden Albee, Zhiming Kuang, and an anonymous referee for helpful comments and suggestions.

## 1.9 References

- Barnes, J. R., J. B. Pollack, R. M. Haberle, C. B. Leovy, R. W. Zurek, H. Lee, and J. Schaeffer, Mars atmospheric dynamics as simulated by the NASA Ames general circulation model, 2, Transient baroclinic eddies, *J. Geophys. Res.*, 98, 3125-3148, 1993.
- Barnes, J. R., R. M. Haberle, J. B. Pollack, H. Lee and J. Schaeffer, Mars atmospheric dynamics as simulated by the NASA Ames general circulation model, 3, Winter quasi-stationary eddies, *J. Geophys. Res.*, 101, 12,753-12,776, 1996.
- Cantor, B. A., P. B. James, M. Caplinger, M. J. Wolff, Martian dust storms: 1999 Mars Orbiter Camera observations, *J. Geophys. Res.*, 106, 23,653-23,687, 2001.
- Caplinger, M., Mars Observer Camera MOC2 calibration report, MSSS internal document, version 1.3, October 1997.
- French, R., P. Gierasch, B. Popp, and R. Yerdon, Global patterns in cloud forms on Mars, *Icarus*, 45, 468-493, 1981.
- Gierasch, P., P. Thomas, R. French, J. Veverka, Spiral clouds on Mars: A new atmospheric phenomenon, *Geophys. Res. Lett.*, 6, 405-408, 1979.
- Haberle, R. M., J. B. Pollack, J. R. Barnes, R. W. Zurek, C. B. Leovy, J. R. Murphy, H. Lee, and J. Schaeffer, Mars atmospheric dynamics as simulated by the NASA Ames general circulation model, 1. The zonal mean circulation, *J. Geophys. Res.*, 98, 3093-3123, 1993.

- Hapke B., Bidirectional reflectance spectroscopy, 4, Extinction and the opposition effect, *Icarus*, 67, 264-280, 1986.
- Hollingsworth, J. L., R. M. Haberle, J. R. Barns, A. F. C. Bridger, J. B. Pollack, H. Lee, and J. Schaeffer, Orographic control of storm zones on Mars, *Nature*, 380, 413-416, 1996.
- Houze, Jr., R. A., *Cloud dynamics*, pp. 573, Academic Press, San Diego, 1993.
- Hunt, G. E. and P. B. James, Martian extratropical cyclones, *Nature*, 278, 531-532, 1979.
- James, P. B., Martian local dust storms, in Recent advances in planetary meteorology, edited by G. Hunt, pp. 85-100, Cambridge Univ. Press, New York, 1985.
- James, P. B., J. F. Bell, R. T. Clancy, S. W. Lee, L. J. Martin, and M. J. Wolff, Global imaging of Mars by Hubble space telescope during the 1995 opposition, *J. Geophys. Res.*, 101, 18,883-18,890, 1996.
- James, P. B., B. A. Cantor, and S. Davis, Mars Observer Camera observations of the Martian south polar cap in 1999-2000, *J. Geophys. Res.*, 106, 23,635-23,652.
- James, P. B. and B. A. Cantor, Martian north polar cap recession: 2000 Mars Orbiter Camera observations, *Icarus*, 154, 131-144, 2001.
- Kahn, R., The spatial and seasonal distribution of Martian clouds and some meteorological implications, *J. Geophys. Res.*, 89, 6671-6688, 1984.

- Leovy, C. B., G. Briggs, A. Young, B. Smith, J. Pollack, E. Shipley, and R. Widley, The Martian atmosphere: Mariner 9 television experiment progress report, *Icarus*, 17, 373-393, 1972.
- Malin, M. C., and K. S. Edgett, The Mars Global Surveyor Mars Orbiter Camera: Interplanetary Cruise through Primary Mission, *J. Geophys. Res.*, 106, 23,429-23,570, 2001.
- Martin, L. J., P. B. James, A. Dollfus, and K. Iwasaki, Telescopic observations: visual, photographic, polarimetric, in Mars edited by Kieffer, H. H., B. M. Jakosky, C. W. Snyder, and M. S. Matthews, pp. 34-70, Univ. Arisona Press, 1992.
- Pettengill, G. H., and P. G. Ford, Winter clouds over the north Martian polar cap, *Geophys. Res. Lett.*, 27, 609-612, 2000.
- Richardson, M. I., and R. J. Wilson, Water ice clouds in the Martian atmosphere: General Circulation Model experiments with a simple cloud scheme, submitted to *J. Geophys. Res.*
- Rodin, A. V., R. T. Clancy and R. J. Wilson, Dynamical properties of Mars water ice clouds and their interactions with atmospheric dust and radiation, *Adv. Space. Res.*, 23, 1577-1585, 1999.
- Smith, A. D., J. C. Pearl, B. J. Conrath, P. R. Christensen, Thermal emission spectrometer results: Mars atmospheric thermal structure and aerosol distribution, *J. Geophys. Res.*, 106, 23,929-23,945, 2001.

Snyder, C. W., The mission of the Viking Orbiters, *J. Geophys. Res.*, 82, 3971-3983, 1977.

Snyder, C. W. and V. I. Moroz, Spacecraft exploration of Mars, in Mars edited by Kieffer, H. H., B. M. Jakosky, C. W. Snyder, and M. S. Matthews, pp. 71-119, Univ. Arisona Press, 1992.

Tamppari L. K., R. W. Zurek, and D. A. Paige, Viking era water-ice clouds, *J. Geophys. Res.*, 105, 4087-4107, 2000.

## **Chapter 2: Cyclones, Tides, and the Origin of a Cross-Equatorial Dust Storm on Mars**

Huiqun Wang<sup>1</sup>, Mark I. Richardson<sup>1</sup>, R. John Wilson<sup>2</sup>, Andrew P. Ingersoll<sup>1</sup>,  
Anthony D. Toigo<sup>3</sup>, Richard W. Zurek<sup>4</sup>

<sup>1</sup>Division of Geological and Planetary Sciences, California Institute of Technology, MC 150-21, Pasadena, CA 91125, USA.

<sup>2</sup>NOAA/Geophysical Fluid Dynamics Laboratory, P.O. Box 308, Princeton, NJ 08542, USA.

<sup>3</sup>Center for Radiophysics and Space Research, Cornell University, Ithaca, NY 14853, USA.

<sup>4</sup>Jet Propulsion Laboratory / California Institute of Technology, Pasadena, California, 91109, USA.

Published in modified form by Geophysical Research Letters, 30, doi: 2002GL016828, 2003.

## 2.1 Abstract

We investigate the triggering mechanism of a cross-equatorial dust storm observed by Mars Global Surveyor in 1999. This storm, which had a significant impact on global mean temperatures, was seen in visible and infrared data to commence with the transport of linear dust fronts from the northern high latitudes into the southern tropics. However, other similar transport events observed in northern fall and winter did not lead to large dust storms. Based on off-line Lagrangian particle transport analysis using a high resolution Mars general circulation model, we propose a simple explanation for the diurnal, seasonal and interannual variability of this type of frontal activity, and of the resulting dust storms, that highlights the cooperative interaction between northern hemisphere fronts associated with low pressure cyclones and tidally-modified return branch of the Hadley circulation.

## 2.2 Introduction

Global and large regional dust storms represent an important component of the main martian climate cycles. They have been observed in the southern spring/summer "dust storm" season, and can increase the mid-level air temperatures by tens of Kelvin. The standard view of such storms assumes initiation and growth in the southern hemisphere, involving feedback between atmospheric circulation and radiative heating of dust [Zurek et al., 1992]. Stochastic and surface dust redistribution processes have been invoked to explain the interannual variability of these storms [Haberle, 1986; Pankine and Ingersoll, 2002], yet a clear linkage between different processes and the triggering of storms is still missing. Daily global mapping by the Mars Global Surveyor (MGS) Mars Orbiter

Camera (MOC) has yielded an unprecedented view of the martian atmosphere [Cantor et al., 2001; Wang and Ingersoll, 2002]. These and other observations have shown that different types of global and large regional dust storms occur. While some apparently originate near topographic slopes in the southern hemisphere, others have more complex histories, involving low-pressure cyclones in the northern hemisphere [Cantor et al., 2001].

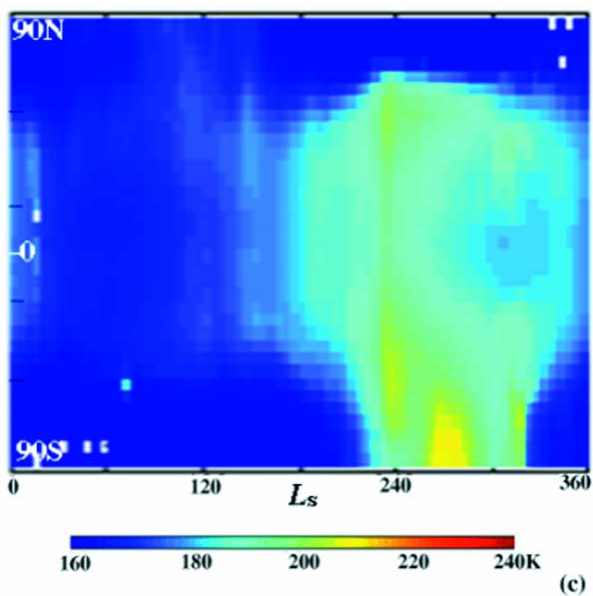
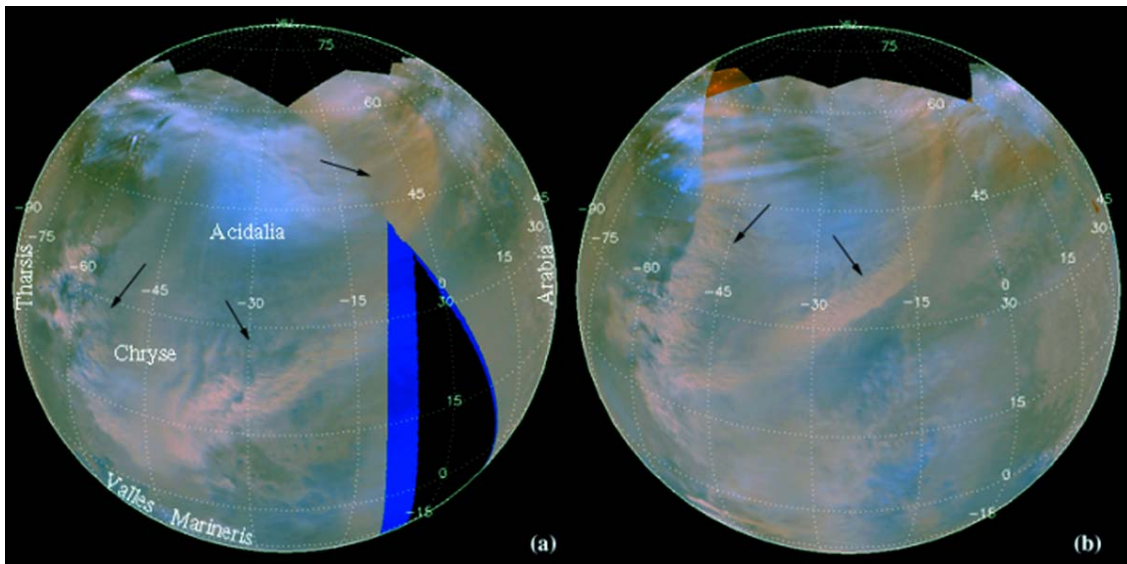


**Figure 2.1 (ab)** Example MGS MOC Wide-angle images of southward moving storms. These storms lead to the largest dust storm in the first MGS mapping year ( $L_s=220^\circ$ - $226^\circ$ ). **(c)** Mid-level ( $\sim 20$ km) air temperatures observed by TES in MGS mapping year 1 as a function of latitude and  $L_s$ .

The largest dust storm in the first MGS mapping year ( $L_s=220^\circ$ - $226^\circ$ ) was an event that produced a significant increase (5-10K) in midlevel atmospheric temperature (Fig. 2.1) [Smith et al., 2001; Liu et al., 2003]. This particular event originated in the northern hemisphere. The development was associated with several bands of dust that were transported southward through Acidalia-Chryse across the equator, possibly augmented by additional dust lifting during transit (Fig. 2.1) [Cantor et al., 2001]. These successive transport events resulted in increased dust opacity in the region southeast of Valles Marineris. The dust was then rapidly spread in longitude to encircle the planet by the strong southern hemisphere subtropical jet [Liu et al., 2003] which results from the deflection of air moving into the Hadley cell convergence zone [Haberle et al., 1993]. The strong correlation between the arrival of dust in the upwelling branch of the Hadley cell and the generation of strong temperature increases observed by the MGS Thermal Emission Spectrometers (TES) (Fig. 2.1c) [Smith et al., 2001; Liu et al., 2003] suggests that this event resulted from the cumulative effect of the southward moving storms. This is consistent with general circulation model (GCM) simulations, which suggest that accumulation of dust in the Hadley convergence zone will lead to atmospheric warming and intensification of the global circulation [Haberle et al. 1982; Wilson, 1997]. MGS observed other southward moving dust fronts that did not generate significant impact on global air temperature. However, they were more isolated in time, and/or failed to penetrate as far south. Observationally, then, the repeated transport of dust into the

Hadley convergence zone appears to be the key to the development of the largest dust storm of the first MGS mapping year. In this paper, we focus on the triggering mechanism, i.e. what differentiates northern hemisphere fronts that penetrate southward to low latitudes and generate storms of global impact from the common frontal systems that remain confined to mid latitudes?

Figure 2.1 illustrates two southward moving dust storms that lead to the large dust storm described above. Fronts are indicated by linear belts of dust presumably lofted by strong near surface winds. Fronts stretch across Acidalia on the lee side of Tharsis as they propagate eastward at 20-28 m/sec. The fronts appear to be associated with low pressure cyclones [James et al., 1999], associated with baroclinic waves [Barnes et al., 1993]. The propagation speeds are consistent with a zonal wave 1 (a single wave cycle around a latitudinal circle) with a period of  $\sim 6$ sols or a wave 3 with a period of  $\sim 2$ sols. These periods agree with other observations and simulations [Barnes et al., 1993; Hinson and Wilson, 2002; Wilson et al., 2002]. While frontal dust storms are common in the northern high latitudes in southern spring and summer, only a small subset are observed to transport dust significant distances southwards.

Southward moving dust fronts occurred multiple times during southern spring and summer in MGS mapping year 1 and 2 (from 1999 to 2001), but were limited to two seasonal periods:  $L_s=210^\circ-230^\circ$  and  $L_s=310^\circ-350^\circ$ . About a dozen individual events have been observed within each seasonal window. All of them have occurred in low-elevation channels in the northern hemisphere, most are associated with Acidalia-Chryse, and some with Arcadia-Amazonis and Utopia. In MGS mapping year 1, most events were concentrated in the  $L_s=210^\circ-230^\circ$  period, with several after  $L_s=310^\circ$ . In MGS mapping

year 2, following the 2001 global dust storm ( $L_s \sim 185^\circ$ ) [Smith et al., 2002], all such events were observed in the  $L_s=310^\circ$ - $350^\circ$  period. The observations pose a number of questions: What causes frontal storms to move southward? Why do only some frontal storms move southward? Why are there two seasonal windows for such events? Why do they follow three primary low-elevation channels? Why do some southward moving dust fronts lead to dust storms of global impact? Why is there interannual variability in large dust storms generated by southward moving fronts?

### **2.3 Analysis with GCM**

This study uses a high resolution ( $2^\circ \times 2.4^\circ$ ) version of the Geophysical Fluid Dynamics Laboratory (GFDL) Mars GCM, which was run for a full martian year [Wilson and Hamilton, 1996; Richardson and Wilson, 2002]. In order to understand the southward moving dust fronts, we used an off-line Lagrangian particle transport model [Eluszkiewicz et al., 1995] to analyze the transport capacity of the 92 simulated low pressure cyclones that passed through Acidalia during  $L_s=200^\circ$ - $355^\circ$ . For each traveling wave system that passed through this region, weightless passive particles were initialized from the surface to 2.5km in the box from  $-94.7^\circ\text{E}$  to  $-63.7^\circ\text{E}$  and from  $49.5^\circ\text{N}$  to  $71^\circ\text{N}$ , and were subsequently advected by the GCM wind field. The particles do not affect the wind field and the wind field does not pick up extra particles. The evolving particle distributions show that the simulated winds can concentrate particles into linear belts similar in shape, size, and propagation speed to the dust fronts observed by MOC (Fig. 2.1, 2.2), suggesting that southward moving dust fronts are associated with eastward traveling baroclinic storms.

In some experiments, a significant number of particles are advected into the low latitudes within 1 sol and into the southern hemisphere within a little over 2 sols (Fig. 2.2a-c). In other experiments, the particles did not extend to the low latitudes, and were eventually advected back to the northern high latitudes (Fig. 2.2d-f). The average rate of southward particle transport was derived by dividing the southward distance traveled by the time spent when the low pressure center passes  $0^{\circ}\text{E}$ . This rate depends upon a number of factors, but the most important ones were local solar time and  $L_s$  (Fig. 2.3). Storms with significant southward motion only occurred when the low-pressure center passed  $0^{\circ}\text{E}$  during the local time interval from 9am to 7pm at  $-35^{\circ}\text{E}$  in Acidalia. At these times, the tidal winds in Acidalia-Chryse are southward, and can interfere constructively with the frontal winds, generating strong southward transport. In other words, these storms passed through Acidalia through an opened "tidal gate", and the particles are advected into the southern hemisphere in  $\sim 2$  tidal cycles. At other local times, tidal winds oppose frontal winds (Fig. 2.2d-f), corresponding to a closed "tidal gate" that prohibits effective southward frontal motion.

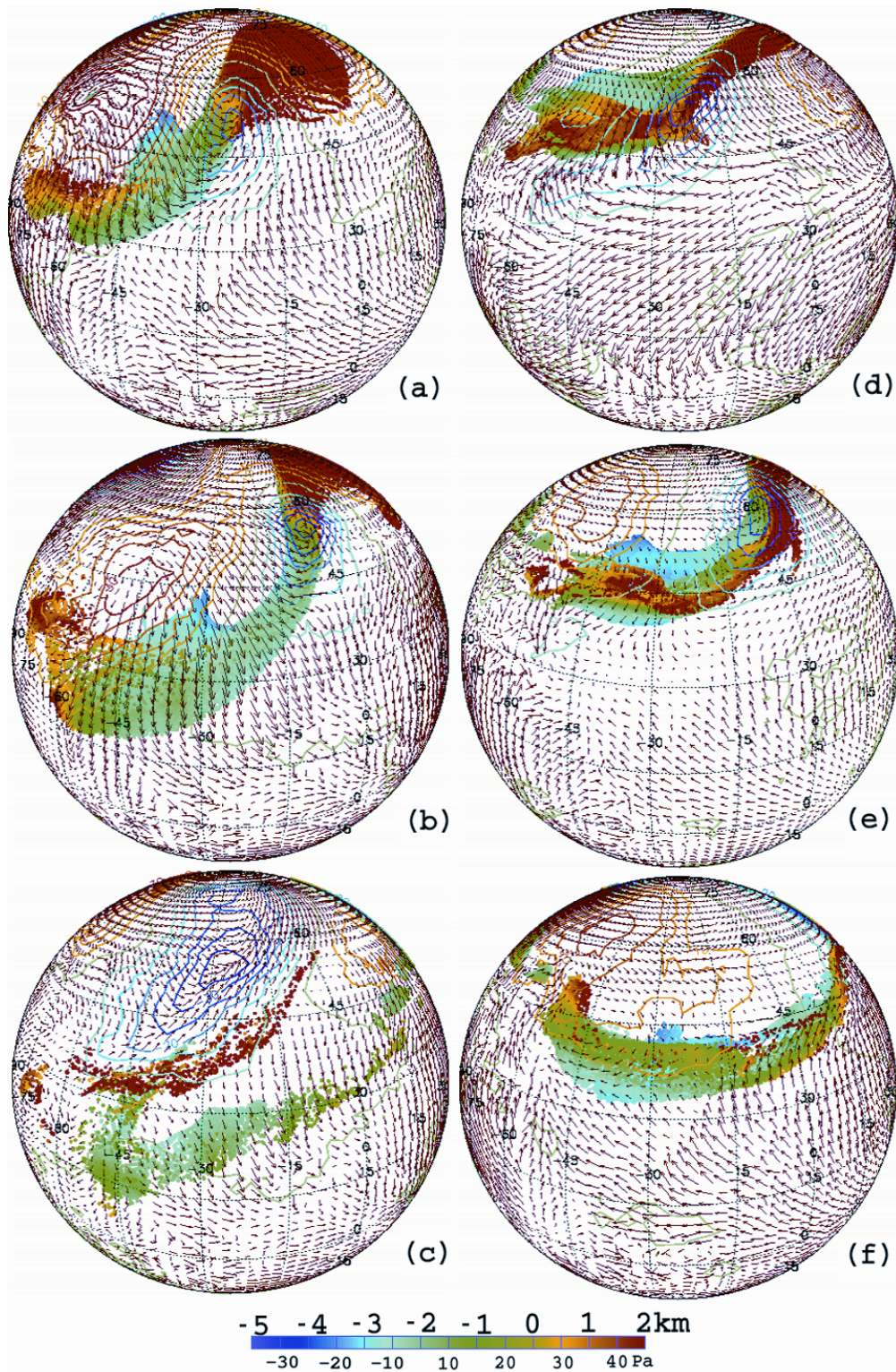


**Figure 2.2** Particle distribution maps from a Lagrangian transport analysis for a front (a-c) with significant southward motion at  $L_s \sim 342^\circ$  and (d-f) without significant southward motion at  $L_s \sim 354^\circ$ . The same map

projection as that used in Fig. 2.1 is applied. The altitudes of the particles are shown as points color-coded above the color bar. High particles are plotted on top of low particles. Simultaneous lowest level (~130m) model winds (vectors) and surface pressure perturbation (Pa, color contours, color-coding below the color bar) are also shown. The particles have been passively advected for (a) 16, (b) 24, (c) 48 hours for the Ls ~342° storm, and (d) 16, (e) 28, (f) 48 hours for the Ls ~354° storm. Low pressure centers pass 0°E in (b) and (e). The local time at -35°E is (b) 11:40am and (e) 3:40am. The particles in the Ls ~342° event get into the southern hemisphere ~50hours after the start of Lagrangian experiment.

The seasonality of the simulated southward transport event is shown in Fig. 2.3b. The distinct decrease in such storms around solstice was found to be associated with a transition from a simulated zonal wave 2 or 3 away from the solstice, to a dominant wave 1 at solstice. Since simulated frontal winds associated with zonal wave 1 are usually weaker than those associated with wave 2 and 3, they do not interact strongly with the tidal winds. The longer periods [Wilson et al., 2002] also result in fewer opportunities for fronts to interact with an "open gate". Wavelet analysis of the simulated mid-level wind field shows that before and after northern winter solstice, there is eddy activity with periods ranging from 2 – 7 sols extending from the northern midlatitude storm zone to the equator. The general interaction of the wave 1 fronts with the tides in multiple model years and the relationship between the mid-level eddy activity and the modeled southward particle motion will be investigated in the future. The southward extension of fronts is influenced by other factors such as the latitude of the low pressure center, and the strength and timing of the trailing high pressure. However, when the southward motion rate is plotted against these factors, we found no systematic trends. So, the "tidal gate" and "seasonal window" provide the most important necessary conditions for southward transport of particles.

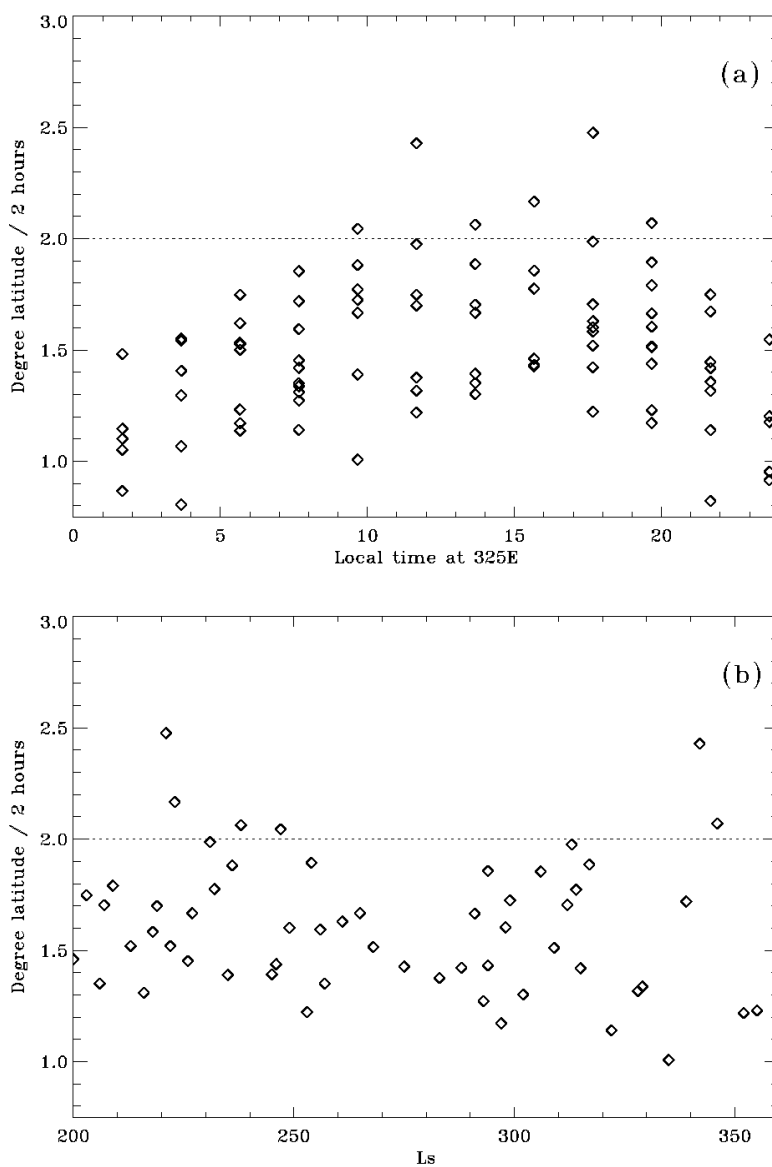


**Figure 2.3** The mean southward particle transport rate ( $^{\circ}$  latitude / 2 hours) derived from the Lagrangian analysis. The points in (a) represent the southward flushing rate of the simulated low pressure storms that pass through Acidalia during  $L_s=200^{\circ}$ - $355^{\circ}$ . The local time at  $-35^{\circ}$ E shown corresponds to the time at which the low pressure center passes  $0^{\circ}$ E. An empirically-derived line is drawn at  $2^{\circ}/2$ hours, which corresponds to the rate necessary to transport particles to the southern hemisphere within  $\sim 2$ sols. (b) The

seasonal dependence of southward motion rates for those storms that traversed Acidalia between 0900-1900LT.

Examination of the simulated surface stresses shows that storms with significant southward motion are associated with coherent broad regions of high surface wind stresses in Acidalia-Chryse (Fig. 2.4d). This results from the constructive interference between the tidal and frontal winds. To investigate the potential for dust lifting, we performed off-line Lagrangian particle experiments with the particles injected whenever the simulated surface stress exceeds a threshold ( $0.0275\text{N/m}^2$ , Fig. 2.4). A curved belt-shaped front can still be identified within the first sol with similar southward motion rate. This particular event was associated with a wave 3 pattern. Many particles are picked up along the way by the front, consistent with the secondary storm centers in some southward moving dust fronts observed by MOC [Cantor et al., 2001]. Similar experiments for fronts without significant southward motion show that particles associated with the baroclinic fronts tend to stay at northern high latitudes. Although there are occasional particle injections in Acidalia-Chryse, the injection areas are small and particles are separate from those in the baroclinic fronts. They appear as isolated small dust storms, instead of a part of a continuous southward moving front.

Both the modeled and observed southward moving storms develop in three channels: Acidalia-Chryse, Arcadia, and Utopia Planitias. These regions correspond with the location of strong Hadley return flow during the daytime, i.e., the western boundary currents [Wilson and Hamilton, 1996]. They are also associated with strong storm tracks [Hollingsworth et al., 1996]. The coincidence of strong frontal storm development and enhanced Hadley/tidal flow in these regions allows southward motion of fronts

associated with low pressure storms. Lower-resolution GCM simulations show interannual variability in the strength of the Acidalia-Chryse eddies between pre- and post-solstice seasonal windows, and indicate variability of the timing of strong southward frontal motion within these windows. The likely number of storms with significant southward motion can be estimated as the following. The seasonal windows are continuously open for only ~50 sols (~30° of Ls). If we take the period of the baroclinic disturbances to be ~2sols, then ~25 storms will pass through Acidalia in each seasonal window. The "tidal gate" is open for ~10 hours each day, or ~40% of the time. This suggests that ~10 storms will have the opportunity to flush particles to the low latitudes. Of these, some will not have a timely strong trailing high pressure, some will lie at too high of a latitude. The model suggests that this will happen about half of the time, generating ~5 events per window. This is in roughly agreement with the MGS observations.

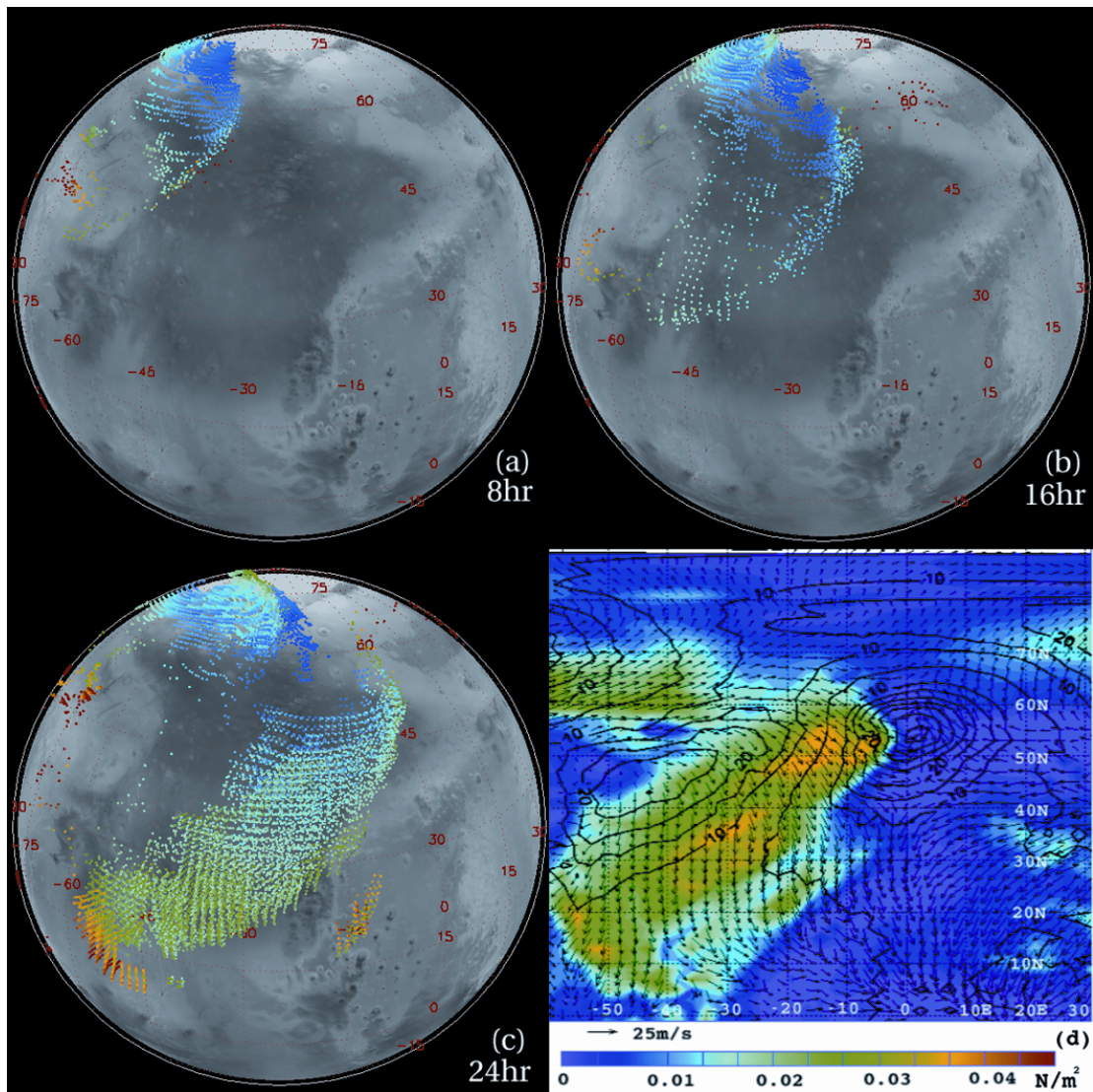


**Figure 2.4** (a-c) Lagrangian particle maps with interactive particle injection for the simulated Ls  $\sim 342^\circ$  storm. This experiment started at the same time as that in Fig. 2.2a-c. The frames are at (a) 8, (b) 16, and (c) 24hr after the beginning. The same map projection and height color-coding as those in Fig. 2.2 are applied. Note the particle number density used here is much less than that in Fig. 2.2. (d) The surface wind stress ( $\text{N/m}^2$ , background color shading), lowest level ( $\sim 130\text{m}$ ) model winds ( $\text{m/s}$ , vector), and surface pressure perturbation ( $\text{Pa}$ , contour) at the time when the low pressure center passes  $0^\circ\text{E}$  for the storm shown in Fig. 2.2b.

## 2.4 Discussion

The largest dust storm in MGS mapping year 1 is associated with several southward moving dust fronts, occurring within days of each other in Acidalia-Chryse. The observations suggest that such fronts in rapid succession can be responsible for the development of large dust storms. GCM simulations suggest that the determinants of whether fronts move southward are local time and season. Local time determines whether the frontal winds synchronously mesh with the tidal winds to generate southward transport. The season determines whether suitable fronts develop. As the seasonal windows are short, and the shortest period of the baroclinic waves is  $\sim 2$  sols [Wilson et al., 2002], there exist few cycles within a given seasonal window for baroclinic storms to synchronize with the tidal flow. Variability within these windows can therefore be generated by the random initial phase and particular synoptic meteorology of the storms. If fronts do not become well synchronized with the tidal flow, southward frontal motion will be diminished or even inhibited. On the other hand, if the phasing and meteorology are favorable, several successive dust fronts could be transported into the southern subtropics. Haberle et al. [1982] and Wilson et al. [1997] demonstrated that injection of dust into the Hadley convergence zone enhances the Hadley circulation, spreading the dust deep into the atmosphere, increasing mid-level air temperatures, and producing global dust storm signatures. The stochastic aspect, resulting from frontal phasing and meteorology then provides a mechanism for interannual variability in this type of large dust storms. Newman et al. [2002] have shown that if surface winds are coupled to dust injection, global models can generate southward moving storms similar to those observed in Acidalia-Chryse, with year-to-year variability.

This paper suggests a mechanism for large dust storm triggering. It provides an example of the interaction of major circulation systems on Mars. Nonetheless, important issues, such as radiative-dynamical feedbacks and a quantitative estimate of the amount of dust needed in the southern tropics for the development of "global impact," have not been addressed. In addition, we only explain the largest dust storm occurred in the first MGS mapping year, and the particular mechanism does not apply generally to all the martian dust storms.

## 2.5 References

- Barnes, J.R., et al., Mars Atmospheric Dynamics as Simulated by the Nasa Ames general-circulation model .2. Transient Baroclinic Eddies, *J. Geophys. Res.*, 98 (E2), 3125-3148, 1993.
- Cantor, B.A., P.B. James, M. Caplinger, and M.J. Wolff, Martian dust storms: 1999 Mars Orbiter Camera observations, *J. Geophys. Res.*, 106 (E10), 23653-23687, 2001.
- Eluszkiewicz, J., R.A. Plumb, N. Nakamura, Dynamics of wintertime stratospheric transport in the Geophysical Fluid-Dynamics Laboratory SKYHI general circulation model, *J. Geophys. Res.*, 100 (D10), 20883-20900, 1995.
- Haberle, R.M., C.B. Leovy, and J.B. Pollack, Some Effects of Global Dust Storms on the Atmospheric Circulation of Mars, *Icarus*, 50 (2-3), 322-367, 1982.
- Haberle, R.M., Interannual variability of global dust storms on Mars, *Science*, 234 (4775), 459-461, 1986.
- Haberle, R.M., et al., Mars Atmospheric Dynamics as Simulated by the NASA Ames General-Circulation Model .1. The Zonal-Mean Circulation, *J. Geophys. Res.*, 98 (E2), 3093-3123, 1993.

- Hinson, D.P. and R.J. Wilson, R.J., Transient eddies in the southern hemisphere of Mars, *Geophys. Res. Lett.*, 29(7), 10.1029/2001GL014103, 2002.
- Hollingsworth, J.L., R.M. Haberle, J.R. Barnes, A.F.C. Bridger, J.B. Pollack, H. Lee, J. Schaeffer, Orographic control of storm zones on Mars, *Nature*, 380, 413-416, 1996.
- James, P.B., J.L. Hollingsworth, M.J. Wolff, and S.W. Lee, North polar dust storms in early spring on Mars, *Icarus*, 138 (1), 64-73, 1999.
- Liu, J., M.I. Richardson, and R.J. Wilson, An assessment of the global, seasonal, and interannual spacecraft record of Martian climate in the thermal infrared, *J. Geophys. Res.*, in press, 2002JE001921.
- Newman, C.E., S.R. Lewis, P.L. Read, and F. Forget, Modeling the Martian dust cycle. 2: Multi-annual radiatively active dust transport simulations, *J. Geophys. Res.*, 107(E12), 5124, doi: 10.1029/2002JE101910, 2002.
- Pankine, A.A. And A.P. Ingersoll, Interannual variability of martian global dust storms- Simulations with a low order model of the general circulation, *Icarus*, 155 (2), 209-323, 2002.
- Richardson, M. I., and R. J. Wilson, Investigation of the nature and stability of the Martian seasonal water cycle with a general circulation model, *J. Geophys. Res.*, 107(E5), 5031, doi: 10.1029/2001JE001536, May 2002.
- Smith, M.D., J.C. Pearl, B.J. Conrath, and P.R. Christensen, Thermal emission spectrometer results: Mars atmospheric thermal structure and seasonal aerosol distribution, *J. Geophys. Res.*, 106 (E10), 23929-23945, 2001.

- Smith, M.D., R.J. Conrath, J.C. Pearl, and P.R. Christensen, Thermal Emission Spectrometer observations of Martian planet- encircling dust storm 2001A, *Icarus*, 157 (1), 259-263, 2002.
- Wang, H., and A.P. Ingersoll, Martian clouds observed by Mars Global Surveyor Mars Orbiter Camera, *J. Geophys. Res.*, 107 (E10), doi: 10.1029/2001JE001815, 2002.
- Wilson, R.J., and K. Hamilton, Comprehensive model simulation of thermal tides in the Martian atmosphere, *J. Atmos. Sci.*, 53 (9), 1290-1326, 1996.
- Wilson, R.J., A general circulation model simulation of the Martian polar warming, *Geophys. Res. Lett.*, 24 (2), 123-126, 1997.
- Wilson, R.J., D. Banfield, B. J. Conrath, and M. D. Smith, Traveling waves in the northern hemisphere of Mars, *Geophys. Res. Lett.*, 29 (14), (10.1029/2002GL014866): art. no. 1684, 2002.
- Zurek, R.W., et al, Dynamics of the atmosphere of Mars, in *Mars*, edited by H.H. Keiffer, B.M. Jakosky, C.W. Snyder, and M.S. Matthews, pp. 835-933, Univ. Arizona Press, Tucson, 1992.

## **Chapter 3: Cloud-tracked winds for the first Mars**

### **Global Surveyor mapping year**

Huiqun Wang and Andrew P. Ingersoll

Division of Geological and Planetary Sciences

California Institute of Technology

Accepted in modified form for publishing by Journal of Geophysical Research – Planets, 108, E9, doi: 2003JE002107, 2003.

### 3.1 Abstract

We have measured winds using cloud motion in consecutive Mars Global Surveyor (MGS) Mars Orbiter Camera (MOC) wide angle global map swaths taken during the first mapping year ( $L_s$  135°-360°-111°). We present a total of ~11,200 wind vectors collected in the north polar region during  $L_s$  135°-195° (late summer/early fall) and  $L_s$  20°-55° (mid spring), and in the south polar region during  $L_s$  337°-10° (late summer/early fall). For cases with good coverage, we also present the derived mean zonal and meridional winds and the associated eddies. The speed of the zonal winds in 60°N-70°N increases at  $\sim 0.6$  m/s/° $L_s$  in late northern summer, and that in 60°S-70°S increases at a rate of  $\sim 0.7$  m/s/° $L_s$  in late southern summer. The latitudinal distribution of zonal wind within 50°N-75°N from mid northern summer to early northern fall indicates that winds at higher latitudes are generally weaker than those at lower latitudes, but the rate of increase with time is faster at higher latitudes. There is a cyclonic gyre in the 90°W-0°-30°E sector in the north polar region. There are large-scale waves in the weekly mean meridional wind and in the bi-weekly mean eddy momentum flux and eddy kinetic energy fields in the north polar region from mid to late summer. The cloud-tracked winds in the north are generally consistent with winds calculated by general circulation model at the water condensation level derived from MGS Thermal Emission Spectrometer (TES) observations, but appear stronger than the gradient winds derived from TES assuming no flow at the surface.

## 3.2 Introduction

Wind measurements provide important constraints for general circulation models (GCM's). The two Viking landers recorded winds continuously at an altitude of 1.6 m [Hess et al., 1977]. Pathfinder measured wind speeds at three heights within 1.2 m of the surface [Sullivan et al., 2000]. However, these measurements are limited to only three locations. Kahn [1983] documented global wind directions derived from Mariner 9 and Viking data. However, wind speed has been deduced in only ~20 cases [e.g. Kahn and Gierasch, 1982; Mischna et al., 1998]. In this paper, we report 11,219 wind vectors derived from cloud tracking for the first MGS mapping year.

Mars Global Surveyor (MGS) is in a polar (2AM-2PM) orbit with a period of about two hours. The red (575-625 nm) and blue (400-450 nm) “push broom” wide-angle Mars Orbiter Cameras (MOC) on board MGS produce 7.5 km/pixel or 3.75 km/pixel global map swaths [Malin and Edgett, 2001]. Twelve consecutive swaths can cover the whole planet in one day. The large overlap of successive orbits in the polar regions provide an opportunity to gather wind measurements through cloud tracking.

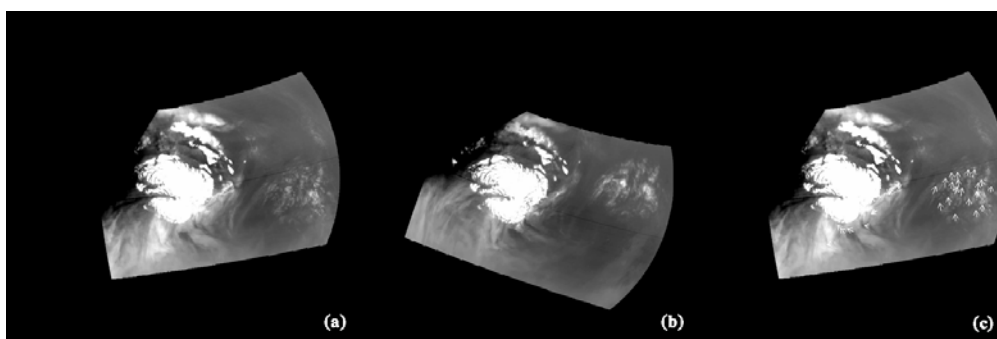


**Figure 3.1** Consecutive processed MOC global map swaths (45N-90N) (a) m01-01743 and (b) m01-01756. (c) Wind vectors superimposed on the image in (a).

Winds can be measured from cloud motion when cloud features can be tracked in two or more images. For this study, we first process the raw global map swaths into polar stereographic images [Wang and Ingersoll, 2002]. We identify the same cloud feature in two images by eye, and draw a vector from the initial to the final position (Fig. 3.1). We divide the distance between them by the time interval to get the velocity. We use two swaths separated by two hours. Most of our tracking is performed in areas where surface features register within 1 pixel between consecutive images. If we miss the true positions of the cloud features by four pixels, we will be ~30 km off in distance and ~4 m/s off in calculated velocity. Errors in the cloud-tracked winds can be reduced by tracking the same cloud feature in two frames separated by many orbits, but this depends on the lifetime of the recognizable features and the paths traveled by the cloud.

The coverage of the wind measurements is far from uniform because the measurement depends on both the overlap area and the presence of clouds that are suitable for tracking. Due to the small overlap of the swaths in the equatorial region, we only track clouds in the north and south polar regions ( $45^{\circ}$ - $90^{\circ}$ N/S). There are generally more clouds in the north than in the south. Cloud amount sharply increases from mid summer to early fall, and greatly decreases from mid spring to early summer in both hemispheres [Wang and Ingersoll, 2002]. Stationary lee waves can only be used for wind direction. Haze is too diffuse for feature recognition. Streaks and fronts can be tracked in the perpendicular direction, but features are hard to identify along them. As a result, polar hood clouds that include haze, streaks, and lee waves are not good candidates for cloud tracking. Moreover, the large terminator circles in the polar

stereographic mosaics during the fall and winter [Wang and Ingersoll, 2002] reduce the image overlap and useful data. These limitations confine the effective cloud tracking period in the first MGS mapping year ( $L_s$  135°-360°-111°) to  $L_s$  135°-195° and 20°-55° in the north polar region, and  $L_s$  337°-10° in the south polar region.

Uncertainty in cloud heights will limit the application of cloud-tracked winds, because both wind velocity and direction change with altitude. Smith [2002] derived the water vapor condensation level for the first MGS mapping year. His results show that during the three effective cloud tracking periods mentioned above, the cloud condensation level is ~10 km above the surface. However, the condensation level only indicates the cloud base of water ice clouds, and is not necessarily related to the height of the optically thick clouds used for tracking. The tracked clouds probably occurred at a variety of levels that spanned many kilometers. In order to derive circulation patterns from the collected wind vectors, we averaged weekly data in this paper and assumed that clouds observed on a weekly timescale formed under similar conditions and had similar cloud heights. In order to compare our measurements with GCM results, we used the NASA Ames GCM winds [Haberle et al., 1993] at the condensation level derived by Smith [2002].

We present cloud-tracked winds and the associated circulation patterns for each week in Section 2. We derive zonal mean winds (zonal and meridional components) for each week in Section 3. We analyze the latitudinal distribution of zonal winds in northern high latitudes during  $L_s$  135°-195° in Section 4. We show the Fourier wave

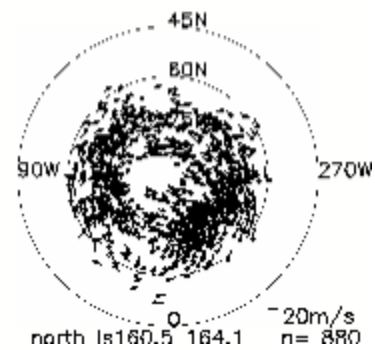
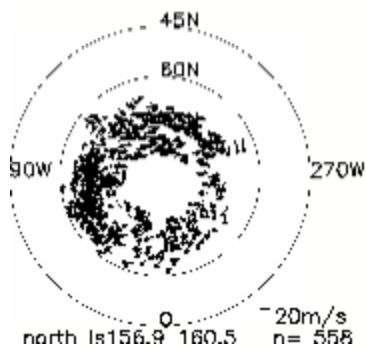
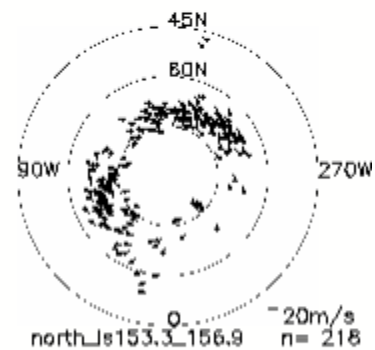
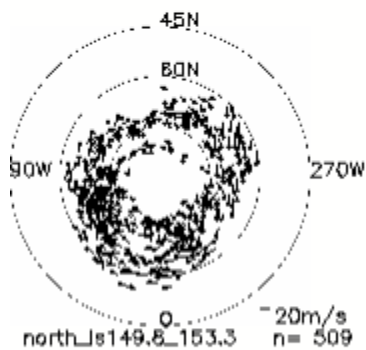
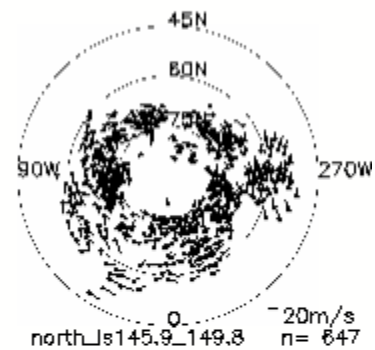
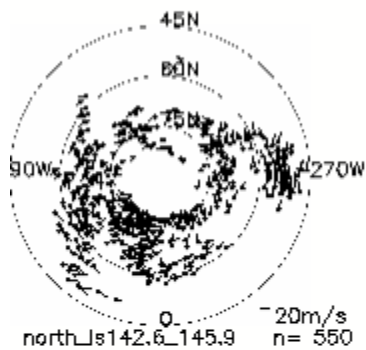
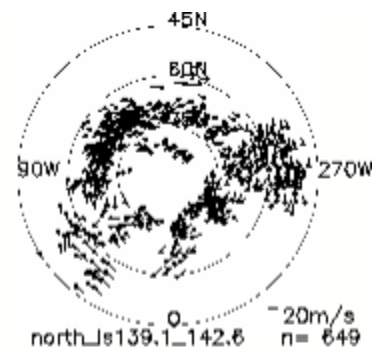
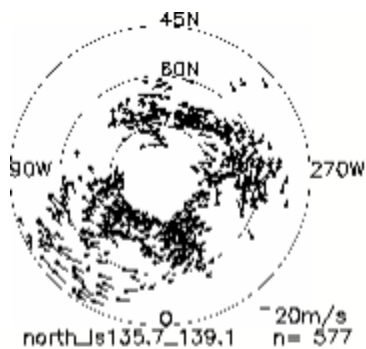
components in meridional wind, and the eddy momentum flux and eddy kinetic energy maps for the north polar region in Section 5. We summarize in Section 6.

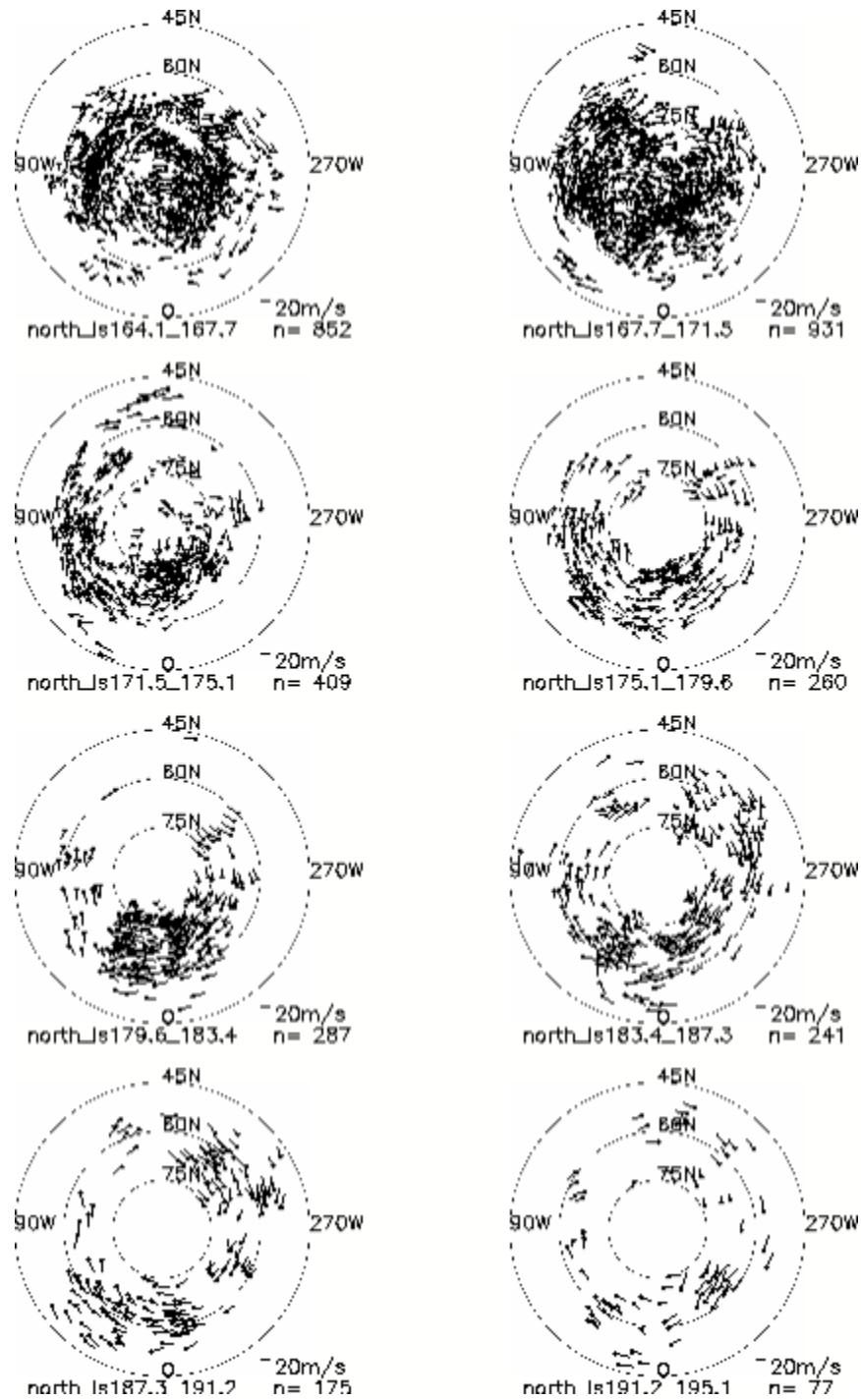
### 3.3 Cloud-tracked winds

#### 3.3.1 North polar region during $L_s$ 135°-195°

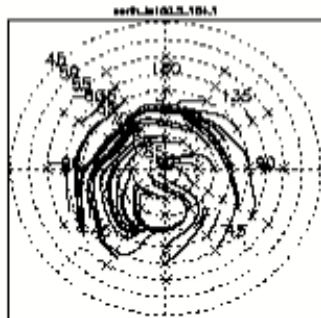
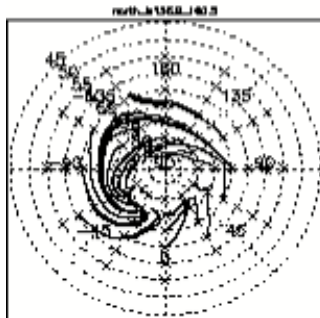
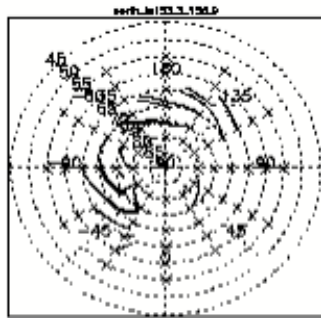
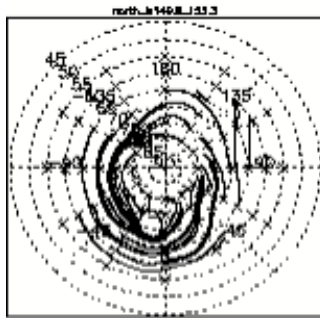
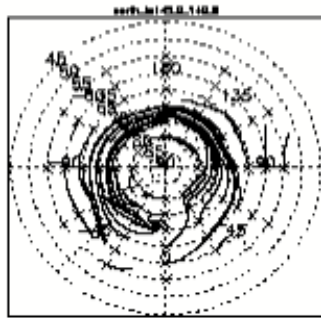
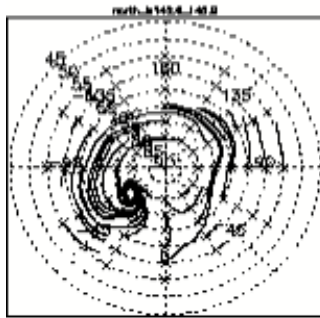
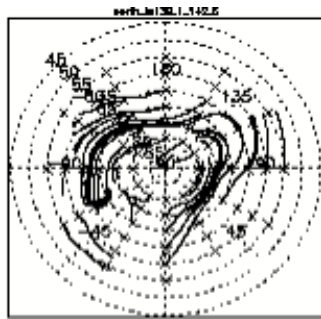
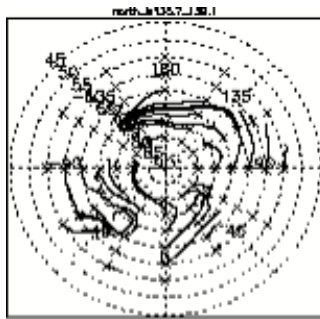
Cloud-tracked winds for the north polar region (45°-90°N) during  $L_s$  135°-195° are shown in Fig. 3.2. Each panel contains results obtained from the 84 blue images taken during the period indicated below the panel (~1 week). A square dot in the panel represents the initial position of a cloud feature. A bar starts from the dot and ends at the final position of the same feature in the next image (~2 hours later). The total number of measurements is indicated below each panel. It depends on the amount and type of cloud during the period, the overlap area of consecutive images, and the seasonal distribution of sunlight. The number of measurements generally increases from ~500/week before  $L_s$  ~160.5° to more than 800/week during  $L_s$  160.5°-171.5°, then sharply decreases afterwards.

Winds south of 75°N generally blow eastward and increase in strength with time during  $L_s$  135°-195°. Before  $L_s$  ~170°, winds north of ~75°N in the 90°W-0°-30°E sector blow westward. Cap edge winds in other sectors generally blow eastward. A number of vectors are collected over the polar cap during  $L_s$  164°-171°, and generally point from the eastern to the western hemisphere (north at ~270°W, south at ~90°W).





**Figure 3.2** Wind vectors collected for the north polar region from mid northern summer to early northern fall. The Ls, total number of vectors, and scale bar are indicated below each panel. The circles represent 45°N, 60°N, and 75°N respectively. West longitudes and north latitudes are indicated in each panel.



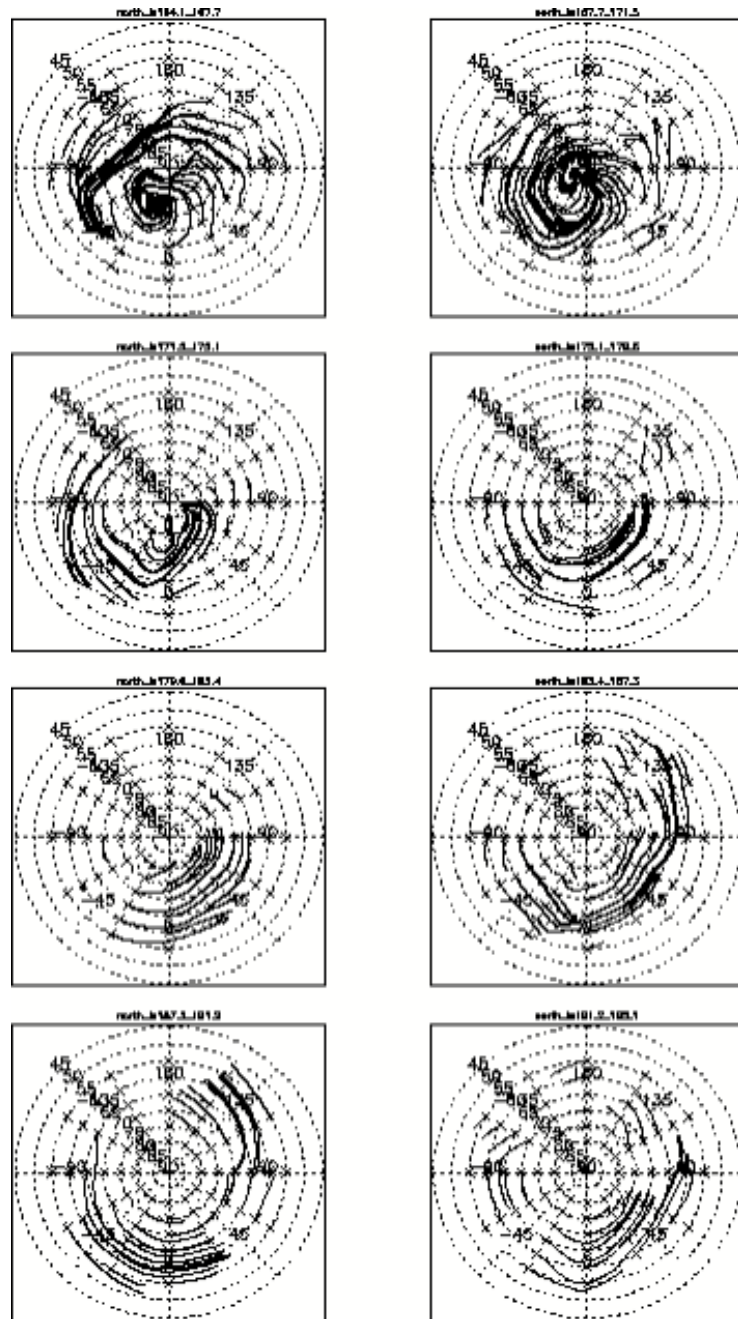
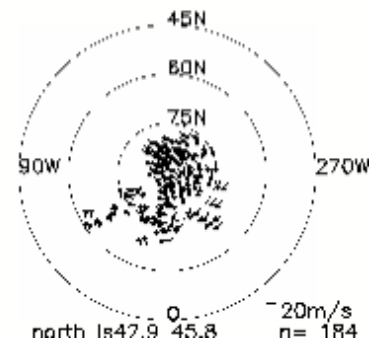
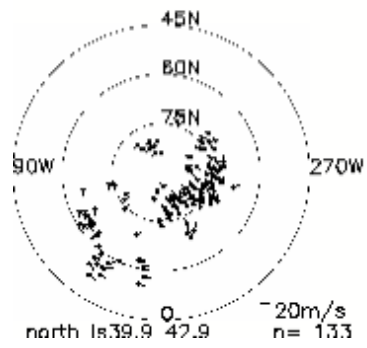
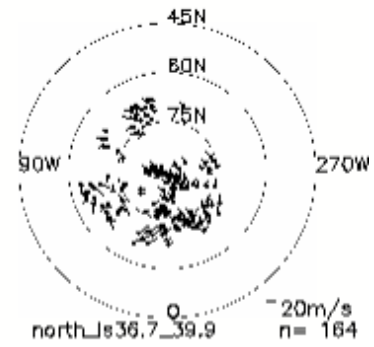
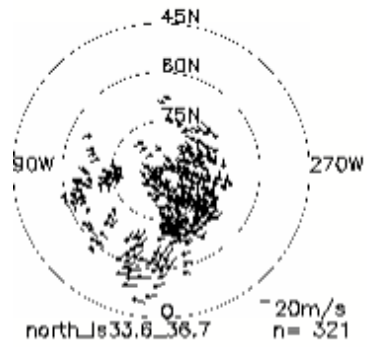
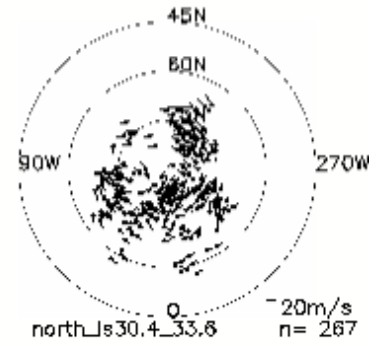
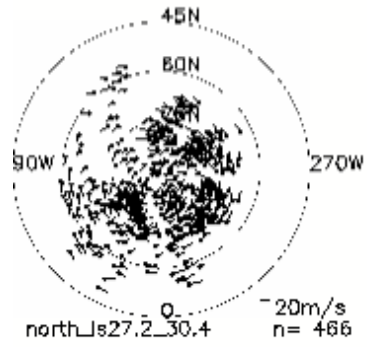
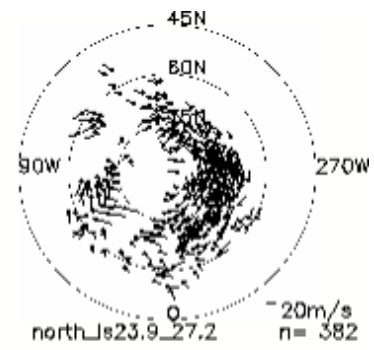
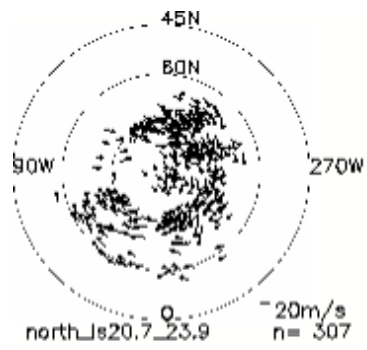


**Figure 3.3** Circulation patterns derived for each panel in Fig. 3.2. See Section 3.2.1. for details. East longitudes and north latitudes are indicated in each panel.

The circulation patterns resulting from the wind measurements can be seen from Fig. 3.3. The lines in each panel start from the crosses and represent “averaged trajectories” of air parcels initially at the positions of the crosses. We first calculate

the average wind speed within a radius (typically 250 km,  $\sim 4.2^\circ$  of latitude) of an initial position represented by a cross, and integrate forward to the next position (the time step varies with the mean velocity, and is typically minutes). We then take this new position as the starting point and integrate one more step. This process is repeated until no further integration is possible due to lack of measurements. A line is formed by sequentially connecting the resulting positions. Each cross represents a starting point of such an integration process. The lines only represent wind direction. Closely spaced lines mainly reflect that many measurements are collected in the neighborhood. The spacing between the lines is not inversely proportional to wind velocity, as would be the case if the lines were streamlines. Fig. 3.3 shows the changing north polar vortex on a weekly timescale. The vortices deviate from the latitudinal circles, and are usually elongated along an axis (which changes with time).

Before  $L_s \sim 170^\circ$ , there is a cyclonic gyre in the  $90^\circ\text{W}-0^\circ-30^\circ\text{E}$  sector. It results from the westward wind at the cap edge in this sector and the eastward winds further south. This area lies north of Acidalia Planitia, and corresponds to the strongest “storm zone” simulated by the NASA Ames GCM [Hollingsworth et al., 1997]. Many frontal clouds have been observed in this sector [Wang and Ingersoll, 2002], indicating that the special circulation pattern may be favorable for baroclinic storm development.



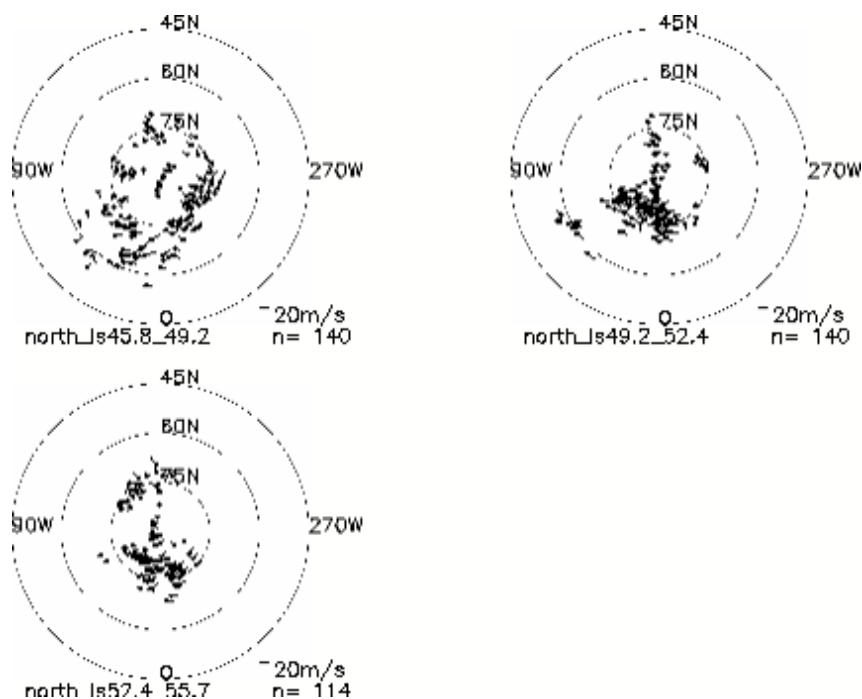


**Figure 3.4** Wind vectors collected in the north polar region during northern spring. The  $L_s$ , total number of vectors, and scale bar are indicated below each panel. West longitudes and north latitudes are indicated in each panel.

### 3.3.2 North polar region during $L_s$ 20°-55°

Cloud-tracked winds for the north polar region during  $L_s$  20°-55° are shown in Fig. 3.4, and the derived air parcel trajectories for selected weeks are shown in Fig. 3.5. The number of vectors gathered each week during this period is much less than that during  $L_s$  160.5°-171.5°, reflecting the decreased number of clouds suitable for tracking. The number of measurements quickly decreases from ~300/week before  $L_s$  ~36° to ~150/week afterwards. Winds south of ~75°N generally blow eastwards and weaken with time. A cyclonic gyre in the 0°-90°W sector is derived for the week of  $L_s$  27.2°-30.4°. Vectors over the polar cap generally point from the eastern to western hemisphere (north at ~270°W, south at ~90°W) before  $L_s$  ~52°. However, they change

to the opposite direction afterwards, suggesting a circulation transition from spring to summer.

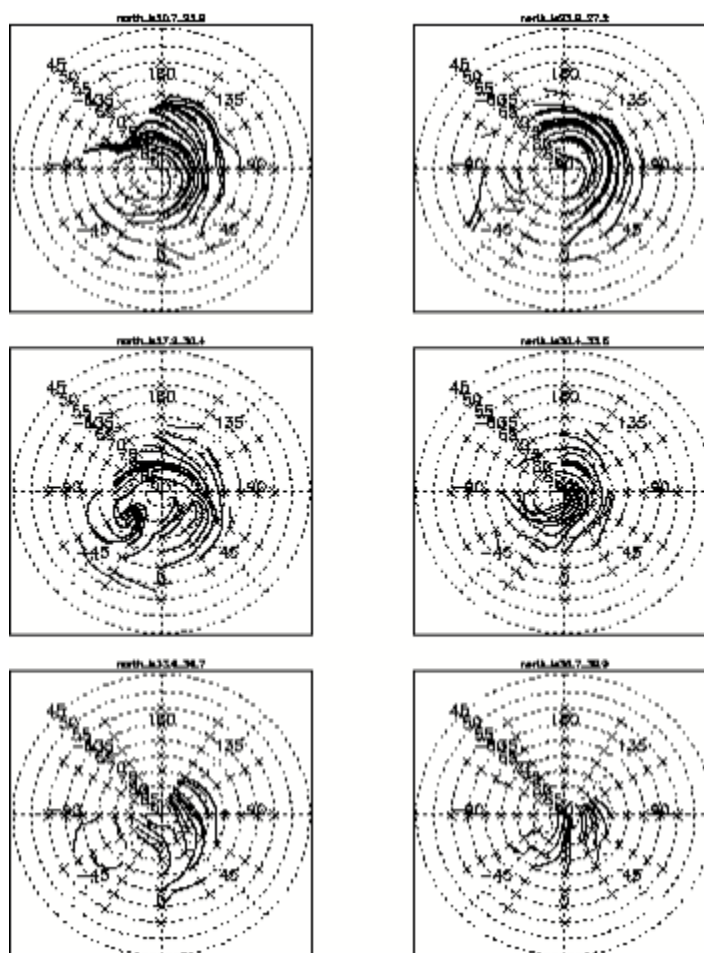


**Figure 3.5** Circulation patterns derived for each panel in Fig. 3.4. See Section 3.2.1. for details. East longitudes and north latitudes are indicated in each panel.

### 3.3.3 South polar region during $L_s$ 337°-10°

Cloud-tracked winds for the south polar region ( $45^\circ$ - $90^\circ$ S) during  $L_s$  337°-10° are shown in Fig. 3.6. Since most of the good candidates for cloud tracking in the south are dust clouds that appear most clearly through the red filter, each panel here contains measurements from 84 red images taken during a week. Note that dust clouds

may be at a different altitude than water ice clouds. The number of measurements is much fewer than that in the north polar region, reflecting the relative lack of clouds and water vapor in the southern hemisphere. Winds north of  $75^{\circ}\text{S}$  generally blow eastward and increase in strength from southern summer to fall. Southwestward winds are sometimes observed south of  $75^{\circ}\text{S}$ , especially in the  $180^{\circ}\text{W}$ - $270^{\circ}\text{W}$  sector. Circulation patterns are not shown for these measurements because of the poor spatial coverage.

Sparse measurements are also collected for the south polar region in mid ( $L_s$   $216^{\circ}$ - $238^{\circ}$ ) and late southern spring ( $L_s$   $254^{\circ}$ - $262^{\circ}$ ) (not shown). Results show that during mid spring, there are eastward winds (10-15 m/s) north of  $75^{\circ}\text{S}$ . As summer approaches, dust storm activities in the south polar maps decrease greatly, and the only tractable features are the arc-shaped cap edge clouds near the terminator [Wang and Ingersoll, 2002]. The motion of these clouds shows off-cap winds in the early evening before southern summer solstice. Our results are roughly consistent with the Viking and Mariner 9 wind directions derived by Kahn [1983].

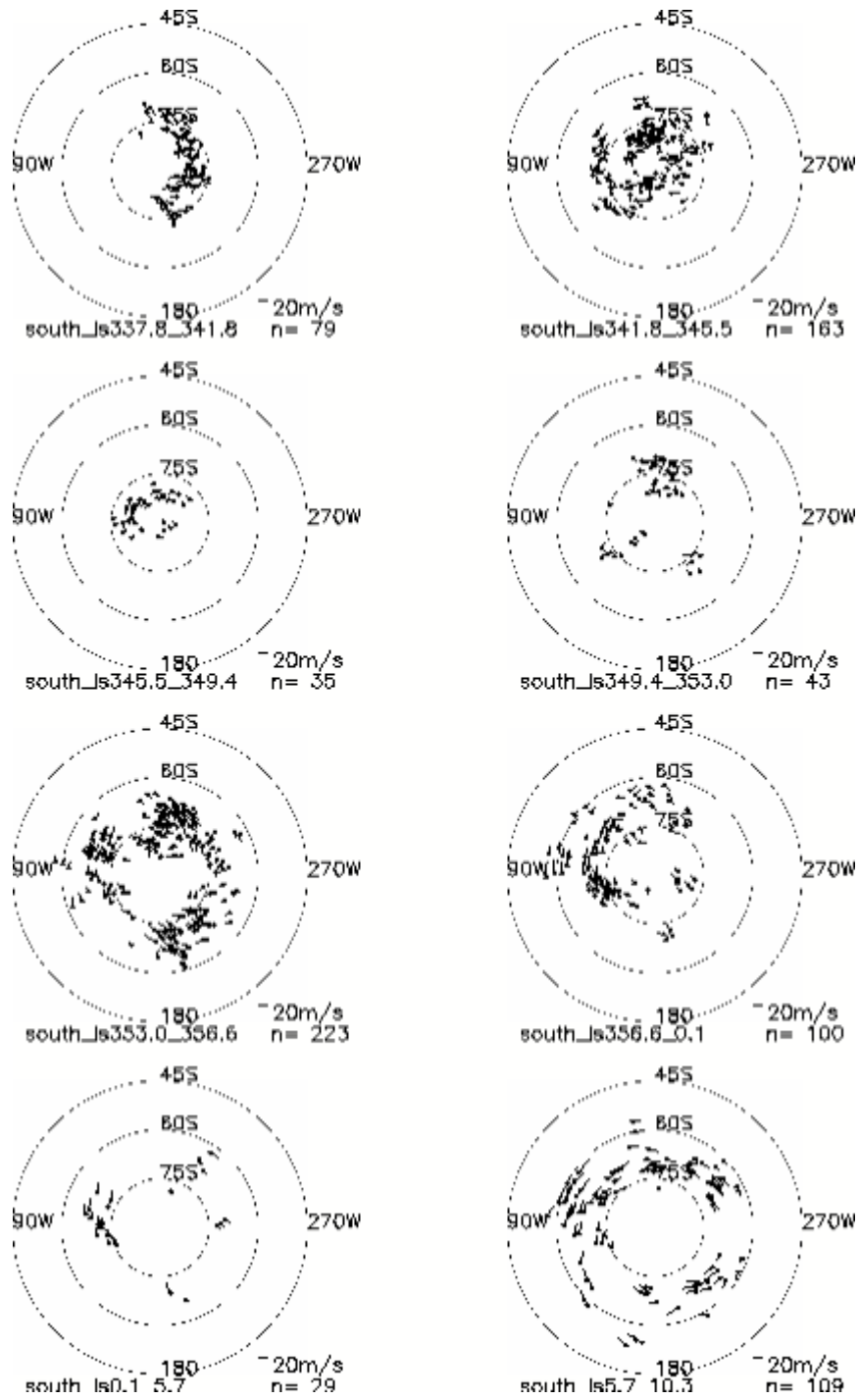


**Figure 3.6** Wind vectors collected in the south polar region from mid summer to early fall. West longitudes and south latitudes are indicated in each panel.

### 3.4 Zonal mean winds

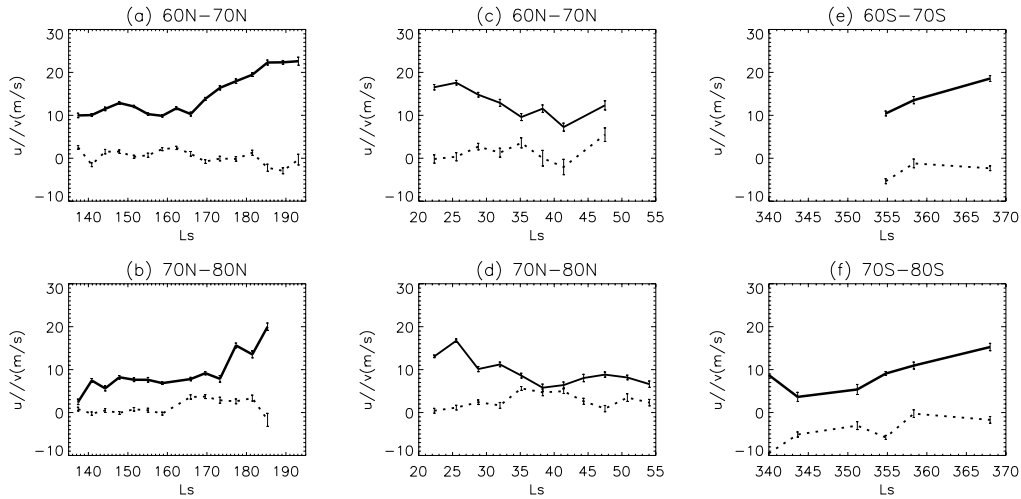


**Figure 3.7** Zonal mean zonal ( $u^*$ , m/s) and meridional ( $v^*$ , m/s) winds in  $60^\circ$ - $70^\circ$ N/S and  $70^\circ$ - $80^\circ$ N/S derived from Fig. 3.2, 3.4, and 3.5. The error bars represent the standard deviation of the mean. See Section 3 for detail.

Fig. 3.7 shows the mean zonal ( $\bar{u}$ ) and meridional ( $\bar{v}$ ) winds for  $60^\circ$ - $70^\circ$ N/S and  $70^\circ$ - $80^\circ$ N/S as a function of  $L_s$  for the three cloud tracking periods presented above. Each data point is derived from a panel in Fig. 3.2, 3.4, or 3.6.  $L_s > 360^\circ$  represents the next Martian year. The error bars represent standard deviation of the mean, i.e.  $\sigma/\sqrt{n}$ , where  $\sigma^2$  is the variance,  $\sigma^2 = \sum (x - \bar{x})^2 / (n - 1)$ ,  $x$  represents  $u$  or  $v$  ( $u > 0$  for eastward wind,  $v > 0$  for northward wind),  $\bar{x}$  is the mean of  $x$ , and  $n$  is the total number of measurements within the latitudinal bin. Cases with  $n < 20$  are neglected.  $\sigma$  is typically  $\sim 5$  m/s. The small error bars for the period  $L_s$   $135^\circ$ - $195^\circ$  reflect the large number of vectors gathered for each week. Since the longitudinal distribution of measurements are non-uniform, the calculated  $\bar{u}$  and  $\bar{v}$  are biased toward the velocity of the areas with dense coverage. For example, if most of the measurements are

concentrated within areas where winds are weak, then the calculated  $\bar{u}$  and  $\bar{v}$  will be smaller than their true values. This bias is expected to be small for most of the cases in Fig. 3.7, but data such as those for 60°N-70°N during  $L_s$  40°-55° and many south polar results should be used with caution. We will assume that  $\bar{u}$  and  $\bar{v}$  represent the true values in the following discussion.

### 3.4.1 North polar region during $L_s$ 135°-195°

The zonal wind ( $\bar{u}$ ) in 60°N-70°N fluctuates within 10-13 m/s during  $L_s$  135°-166°, then smoothly increases at  $\sim 0.6$  m/s/° $L_s$  to  $\sim 23$  m/s by  $L_s \sim 185^\circ$  (Fig. 3.7a). Haberle et al. [1993] presented latitude-altitude cross sections of zonal wind simulated by the NASA Ames GCM. Their Fig.12 shows that during  $L_s$  140°-166°,  $\bar{u}$  in 60°N-70°N increases with height and decreases with latitude. In the simulations, the altitude range where the winds are 10-13 m/s is 4-8 km at 60°N and 8-11 km at 70°N, suggesting a height of  $7.5 \pm 3.5$  km for our cloud-tracked winds during a similar period. Many cloud-tracked winds are subject to local or regional circulations that could not be represented by GCM. Nonetheless, the height range above is consistent with the <10 km condensation level near the cap edge during this period [Smith, 2002]. Smith et al. [2001] derived gradient winds (balancing pressure gradient force, Coriolis force, and centrifugal force) from atmospheric temperatures retrieved from MGS TES, assuming zero winds at 7.1 mb. Their results for  $L_s = 135^\circ$  show that the winds are less than 10 m/s below 10 km, which is the condensation level derived by Smith [2002]. This speed is less than the 10-13 m/s speeds that we measure, indicating that one of the assumptions, e.g. zero winds at the surface or measured winds below 10 km altitude, is wrong. For comparison, the gradient wind calculation gives winds of 10-13

m/s at altitudes of 12-14 km, which is above the condensation level according to Smith [2002]. It should be noted, however, TES retrievals are uncertain in the lower atmosphere [Smith et al., 2001], and errors in the derived wind field are probably significant.

The rapid increase of  $\bar{u}$  during  $L_s$  166°-185° is expected from the increasing latitudinal temperature gradient and is consistent with GCM simulations and TES data [Haberle et al., 1993; Smith et al., 2001]. The increasing trend in wind velocity could also be related to systematic increase in cloud height. The water vapor condensation level near the north polar cap sharply increases from <10 km to >40 km in early northern fall [Smith, 2002], indicating increasing height of water ice clouds with time. Since zonal winds increase with both height and  $L_s$ , larger values of  $\bar{u}$  after  $L_s \sim 185^\circ$  are expected from cloud tracking. However, the observed  $\bar{u}$  levels off at  $\sim 23$  m/s. Many vectors in early northern fall are derived from streak clouds which are the most representative features in the polar hood [Wang and Ingersoll, 2002]. Since we only track the wind component that is perpendicular to the streak clouds, the true wind velocity could be larger.

Zonal wind in 70°N-80°N follows a similar trend as that in 60°N-70°N. However, the velocity is generally smaller and the rapid strengthening of wind occurs  $\sim 7^\circ L_s$  later (Fig. 3.7b). The water vapor condensation level in this latitudinal band is lower than that in 60°N-70°N, indicating lower water ice clouds. Zonal wind cross section simulated by NASA Ames GCM for  $L_s$  140°-166° [Haberle et al., 1993] show that the northern hemisphere zonal jet in the height range of 5-10 km peaks around 55°N with

decreasing wind strength toward the north pole and equator. Since  $\bar{u}$  increases with height at fixed latitude and decreases with latitude at fixed height, the factors mentioned above would contribute to weaker zonal wind in 70°-80°N than that in 60°-70°N. The timing of the rapid strengthening of winds can be affected by changes in both the wind field structure and the cloud height.

The meridional wind ( $\bar{v}$ ) in 60°N-70°N is on average +1.2 m/s during  $L_s$  135°-166°, ~0 during  $L_s$  166°-185°, and -1.8 m/s during  $L_s$  185°-195° (Fig. 3.7a).  $\bar{v}$  in 70°N-80°N remains at 0 during  $L_s$  135°-160°, +3 m/s during  $L_s$  165°-180°, -1.7 m/s afterwards. Negative  $\bar{v}$  (southward) is derived only for cases with poor longitudinal coverage. Large meridional winds are associated with the cyclonic gyres in the circulation (Fig. 3.2 and 3.3). On-cap winds in the eastern part of the gyre generally have higher velocity than off-cap winds in the western part of the gyre, resulting in average northward flow. Column water vapor abundance derived from TES decreases with latitude in northern mid and high latitudes during  $L_s$  150°-195° [Smith, 2002]. If the same latitudinal trend holds at the height of our measurements, then our data suggest poleward transport of water vapor by the gyre at least during  $L_s$  150°-180°. In contrast to our observations, the GCM simulated  $\bar{v}$  in 60°N-70°N for  $L_s$  140°-160° is southward at the levels where water ice clouds are expected (5-10 km) [Haberle et al., 1993]. However, since the spatial coverage of our measurements is non-uniform, the derived mean meridional wind is probably biased, and the direction of water vapor transport by the polar circulation remains unclear.

### 3.4.2 North polar region during $L_s$ 25°-55°

The zonal wind ( $\bar{u}$ ) in 60°N-70°N quickly decreases from ~20 m/s to ~10 m/s during  $L_s$  25°-35°, and then fluctuates around 10 m/s in mid northern spring (Fig. 3.7c). Haberle et al. [1993] simulated 20 m/s zonal wind in 60°N-70°N at ~8 km for  $L_s$  0°-23°. This height is consistent with the <10 km water vapor condensation level near the north polar cap in early northern spring [Smith, 2002]. The condensation level gradually increases to 10-12 km in mid spring, indicating higher water ice clouds and thus stronger winds [Smith, 2002]. This effect must be counteracted by the decreasing latitudinal temperature gradient which decreases the zonal wind.

A similar trend is observed for  $\bar{u}$  in 70°N-80°N, but the velocities are smaller and the decreasing trend lasts until  $L_s$  ~38° (Fig. 3.7d). The meridional wind ( $\bar{v}$ ) in 70°N-80°N is positive (northward) during  $L_s$  20°-55°, and can reach +5 m/s during  $L_s$  35°-42° (Fig. 3.7d). Haberle et al. [1993] simulated northward wind in 70°N-80°N within the 5-10 km altitude range for  $L_s$  0°-23°. The meridional wind ( $\bar{v}$ ) in 60°N-70°N is generally positive with exceptions during  $L_s$  40°-45°. Examining Fig. 3.4, we find that measurements after  $L_s$  ~40° are much sparser, and are concentrated within certain longitudinal sectors especially south of 75°N.

### 3.4.3 South polar region during $L_s$ 337°-10°

The zonal winds in 60°S-70°S increase from ~10 m/s to 19 m/s during  $L_s$  355°-8° (Fig. 3.7e). This increase with  $L_s$  (~0.7 m/s/° $L_s$ ) is a little faster than the 0.6 m/s/° $L_s$  for  $\bar{u}$  in 60°N-70°N during  $L_s$  166°-185°. The zonal winds in 70°S-80°S generally increase with  $L_s$  as well (Fig. 3.7f). (The data for  $L_s$  337.8°-341.8° are probably biased

due to the poor coverage (see Fig. 3.6)). The latitude-height cross section of zonal wind for  $L_s$   $0^\circ$ - $23^\circ$  simulated by NASA Ames GCM shows that 10-15 m/s winds occur within  $\sim 3$  km of the surface at southern high latitudes [Haberle et al., 1993]. In comparison, the water vapor condensation level is 5-10 km [Smith, 2002]. Since most clouds we tracked for the south polar region are dust clouds in red images, the discrepancy between the cloud height indicated by the NASA Ames GCM and that indicated by the water condensation level can be explained if the dust clouds are near the surface. The meridional wind in southern high latitudes are southward (poleward) during  $L_s$   $340^\circ$ - $10^\circ$ . This agrees with the lower branch of a meridional circulation cell with air rising near the pole and sinking in mid latitudes as the NASA Ames GCM has simulated for  $L_s$   $0^\circ$ - $23^\circ$  [Haberle et al., 1993].

### 3.5 Latitudinal distribution of zonal wind

The latitudinal distribution of zonal wind ( $\bar{u}$ ) in  $50^\circ\text{N}$ - $75^\circ\text{N}$  for four consecutive 4-week periods during  $L_s$   $135.7^\circ$ - $195.1^\circ$  is shown in Fig. 3.8a. Each data point in Fig. 3.8a is calculated by averaging all measured zonal winds within  $2.5^\circ$  of the central latitude. Cases when the number of measurements is less than 60 are neglected. The error bar represents the standard deviation of the mean which is defined in the previous section. To investigate to what degree the data can be explained by solid body rotation, we calculated  $\bar{u}/\cos(\text{latitude})$  for each latitudinal bin. The results for each week are shown in Fig. 3.8b. Pure solid body rotation will result in a horizontal line, with larger values corresponding to faster rotation. To investigate the possibility of inertial instability and barotropic instability, we plotted the absolute vorticity of the

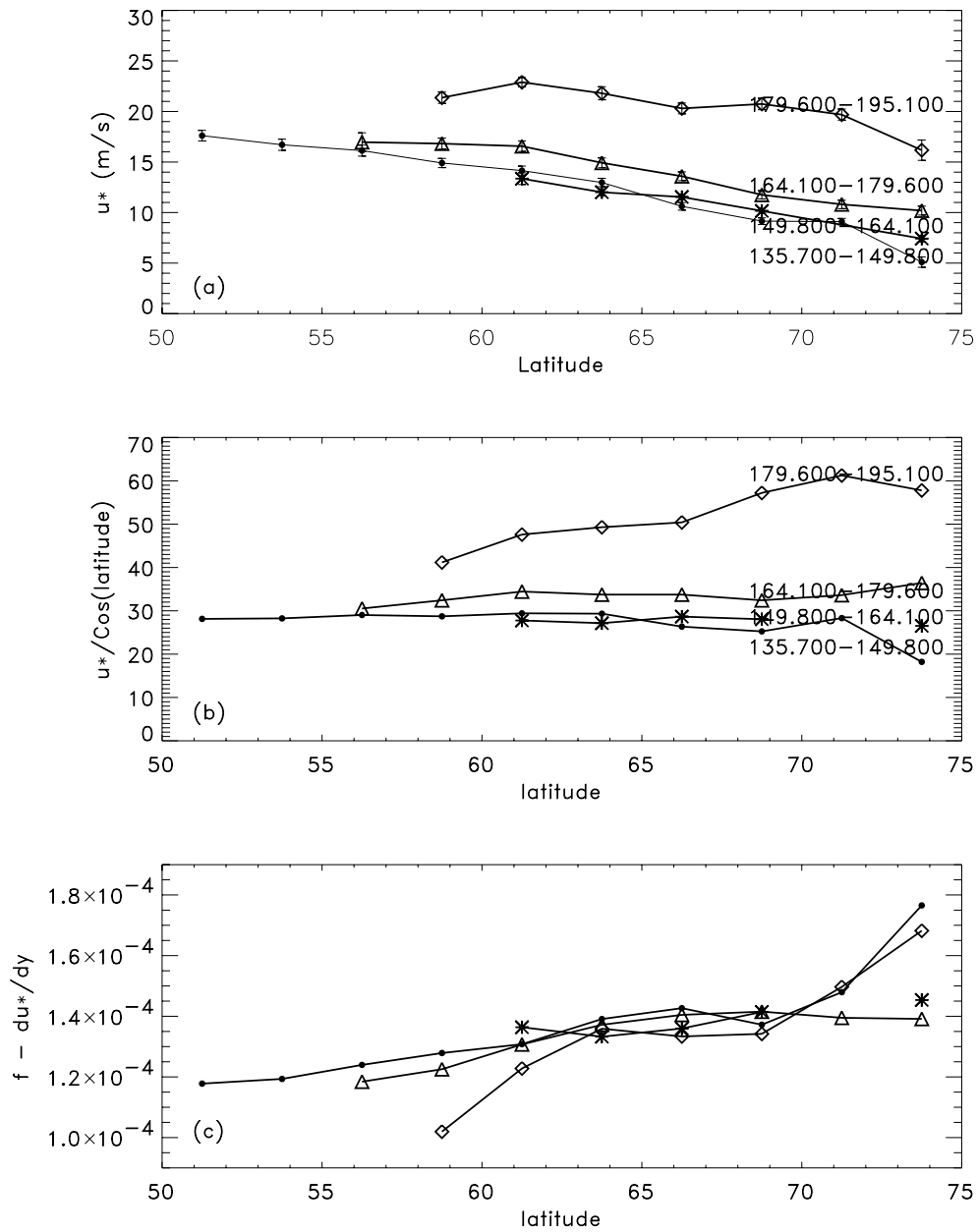
mean flow ( $Q = f - d\bar{u}/dy$ ) in Fig. 3.8c for each period, where  $y$  is the distance between the latitudinal intervals, and  $f$  is the Coriolis parameter. Zonal flow is inertially stable if the absolute vorticity is positive [Salby, 1996]. A necessary condition for barotropic instability is that  $dQ/dy$  changes sign somewhere in the interior [Salby, 1996]. We have assumed that all the measurements were at the same height in this section.

Fig. 3.8a shows that  $\bar{u}$  generally decreases with latitude at least before  $L_s \sim 180^\circ$ , indicating that the data are located on the poleward side of the jet stream. Fig. 3.8a also shows that  $\bar{u}$  for each latitudinal bin increases with  $L_s$  from mid northern summer to early northern fall. The increase becomes faster with time. Moreover, the increase at higher latitudes is larger than that at lower latitudes, resulting in a shallower slope of  $d\bar{u}/dy$  at later times. The mean slopes for the four consecutive periods are -0.52, -0.46, -0.44, and -0.33 m/s/ $^\circ$ latitude respectively. Both the simulated  $\bar{u}$  for  $L_s$  165.2 $^\circ$ -176.5 $^\circ$  (Fig. 3.9a) and the observed  $\bar{u}$  for  $L_s$  164.1 $^\circ$ -179.6 $^\circ$  (Fig. 3.8a) remain roughly constant with latitude south of  $\sim 61^\circ\text{N}$ , with the observed  $\bar{u}$  falling between the simulated 3mb and 3.8mb  $\bar{u}$ . Opposite to the observation, the simulated 300 mb  $\bar{u}$  decreases with latitude first slowly within  $61^\circ\text{N}$ - $67^\circ\text{N}$  then quickly north of  $\sim 67^\circ\text{N}$ , and the simulated 380 mb  $\bar{u}$  even increases slightly within  $61^\circ\text{N}$ - $67^\circ\text{N}$ . Difference in zonal wind structure could lead to different eddy activities and eddy-mean flow interactions [Barnes et al., 1993].

Most data before  $L_s \sim 180^\circ$  are roughly consistent with solid body rotation (Fig. 3.8b), with an apparent increase in angular velocity during  $L_s$  150 $^\circ$ -180 $^\circ$ . The exceptionally low value at  $74^\circ\text{N}$  for  $L_s$  135.7 $^\circ$ -149.8 $^\circ$  results from the westward

(negative) winds near the polar cap in the 90°W-0°-30°E sector (see Fig. 3.2 and 3.3). The rate of rotation greatly increases during  $L_s$  180°-195° at all latitudes where data exist. The increase is larger at higher latitudes, leading to the deviation from solid body rotation in Fig. 3.8b. The observed increase of rotation with latitude within 59°N-66°N for  $L_s$  179.6°-195.1° (Fig. 3.8b) is simulated by the GCM (Fig. 3.9b). However, the GCM results show increase throughout 50°N-75°N, while the observed value at ~74°N is lower than that at ~71°N. Moreover, the simulated rotation rates are much larger than the observed values.

All the derived absolute vorticities in Fig. 3.8c are positive, indicating inertially stable zonal flows. The latitudinal slope of  $dQ/dy$  changes from positive to negative to positive with increasing latitude during  $L_s$  135.7°-149.8° and  $L_s$  179.6°-195.1°. It changes from positive to negative during  $L_s$  164.1°-179.6°, and from negative to positive during  $L_s$  149.8°-164.1°. In summary,  $dQ/dy$  changes sign somewhere in 60°N-70°N during  $L_s$  135°-195°, suggesting possible barotropic instabilities in this region. If the curvature of the vertical profile of  $\bar{u}$  is large, vertical shear can become the dominant factor in potential vorticity ( $P$ ), and change the sign of the slope of  $dP/dy$  (where  $\frac{dP}{dy} = \frac{dQ}{dy} - \frac{1}{\rho} \frac{\partial}{\partial z} \left( \frac{f^2}{N^2} \rho \frac{\partial \bar{u}}{\partial z} \right)$ ,  $\rho$  is atmospheric density,  $N^2$  is Brunt-Vaisalla frequency), signaling possible baroclinic instability [Salby, 1996].



**Figure 3.8** (a) Latitudinal distribution of zonal winds ( $u^*$  m/s) within 50°N-75°N for Ls 135.7°-149.8° (dot), Ls 149.8°-164.1° (star), Ls 164.1°-179.6° (triangle), and Ls 179.6°-195.1° (diamond). (b) Latitudinal distribution of  $u^*/\cos(\text{latitude})$  for each curve in (a). (c) Latitudinal distribution of absolute vorticity  $Q=f-du^*/dy$  for each curve in (a).

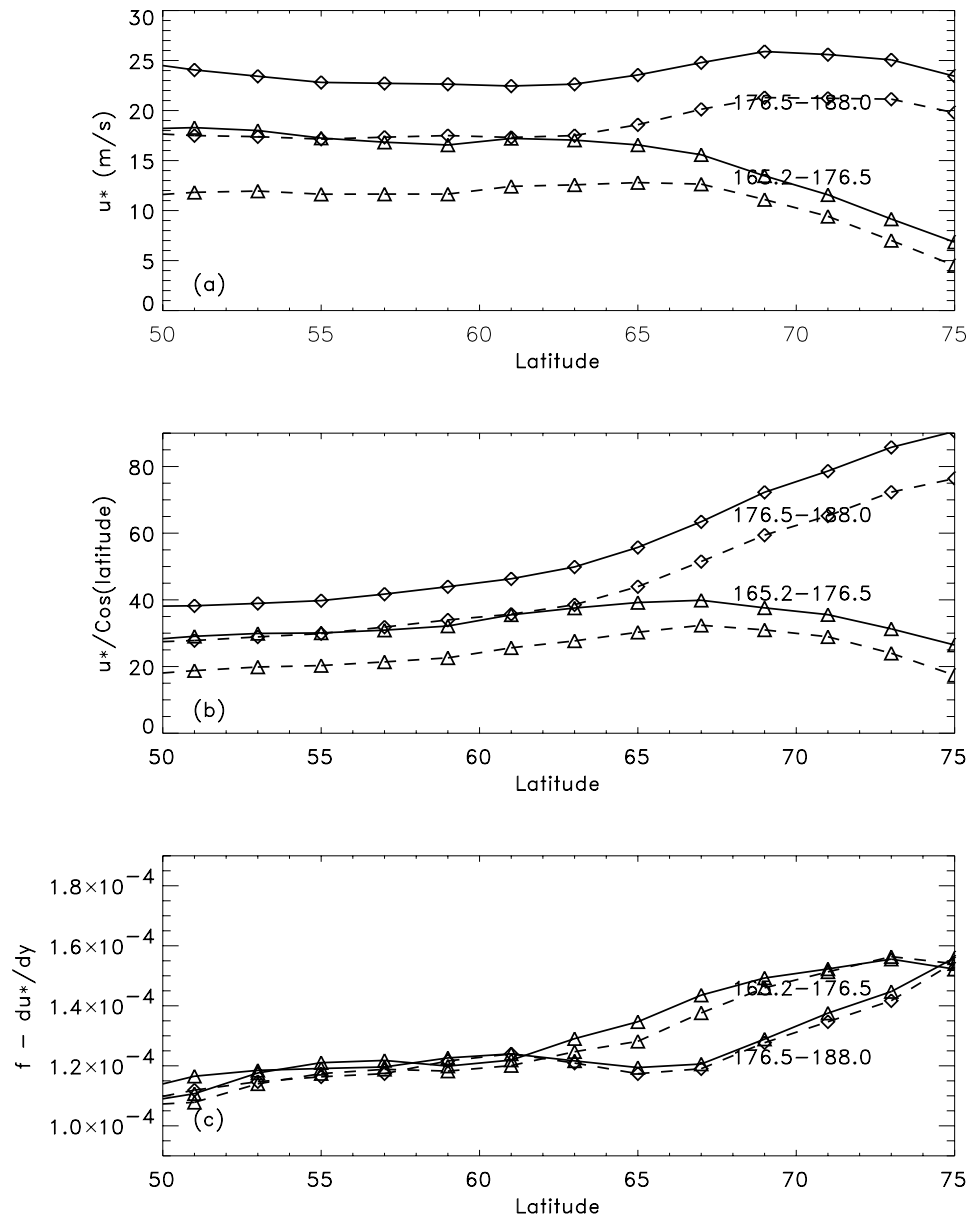


**Figure 3.9** GFDL Mars GCM simulated zonal wind ( $u^*$ ),  $u^*/\text{Cos}(\text{latitude})$ , and absolute vorticity ( $Q=f-du^*/dy$ ) within 50°N-75°N for 3.0 mb (solid line) and 3.8 mb (dashed line) during Ls 176.5°-188.0° (diamond) and Ls 165.2°-176.5° (triangle).

## 3.6 Eddy winds

### 3.6.1 Fourier wave components

Based on the data coverage, we analyze the Fourier wave components at  $70^\circ\text{N}$  during  $L_s$   $135^\circ$ - $172^\circ$ . We choose 48 uniformly distributed grid points ( $\sim 150$  km spacing) along the  $70^\circ\text{N}$  latitudinal circle, and calculate the local average meridional wind  $v^*$  by averaging the measurements within 300 km of each grid point for each week. If the number of measurements near a grid point is less than 6, then  $v^*$  is labeled missing. If the total number of missing points along the latitudinal circle is less than 12, then linear interpolation is performed to fill in the missing data. The results are displayed as dots in Fig. 3.10a. The dashed lines denote 0 m/s for the week. The interval between the tick marks on the vertical axis is 5 m/s. The over plotted solid lines in Fig. 3.10a are composed from Fourier components up to wave 3. The general longitudinal variations are well represented by the first three waves. The longitude- $L_s$  cross sections for Wave 1, 2, and 3 are shown in Fig. 3.9b, c, and d respectively (with the same shading scheme as the bar next to the Wave 1 panel).

Before  $L_s \sim 160^\circ$ , Wave 1 has a mean amplitude of  $\sim \pm 2$  m/s, with northward  $v^*$  at  $\sim 335^\circ\text{W}$  and southward  $v^*$  at  $\sim 155^\circ\text{W}$ . After  $L_s \sim 160^\circ$ , the amplitude of Wave 1 is in the range of 4-8 m/s, and the northward and southward  $v^*$  rotate eastward to  $\sim 265^\circ\text{W}$  and  $\sim 85^\circ\text{W}$  respectively. Referring to Fig. 3.3, we see that larger amplitude Wave 1 is related to the polar vortex whose center is farther away from the pole. The amplitudes of Wave 2 range from  $\pm 1$  to  $\pm 5$  m/s during  $L_s$   $135^\circ$ - $172^\circ$ , and those of Wave 3 range from  $\pm 1$  to  $\pm 3$  m/s. Referring to Fig. 3.3, we see that large amplitude Wave 2 during  $L_s$

139.1°-142.6° and 149.8°-153.3° corresponds to elliptical trajectories. Northward  $v^*$  for Wave 2 is usually found at  $\sim 170^\circ\text{W}$  and  $\sim 350^\circ\text{W}$ . Northward  $v^*$  for Wave 3 is usually found at  $\sim 90^\circ\text{W}$ ,  $210^\circ\text{W}$ , and  $330^\circ\text{W}$ . Both the amplitude and phase of Wave 2 and 3 appear to oscillate with time, with the oscillation period of amplitude being approximately half of the period of phase. Fig. 3.10cd indicate that the phase of Wave 2 oscillates with a period of  $\sim 10$  weeks and an amplitude of  $\sim 25^\circ$  in longitude, while the phase of Wave 3 oscillates with a period of  $\sim 5$  weeks and an amplitude of  $\sim 15^\circ$  in longitude. The locations of southward (negative) eddy meridional wind for Wave 3 appear to coincide with low topography.

Since each data point in Fig. 3.10a represents the mean of all the measurements collected near a grid point during a week, contributions from shorter period ( $< 7$  sols) traveling waves are expected to be averaged out. Banfield et al. [2003] show that the 2PM-2AM sampling strategy of MGS can result in certain thermal tides and stationary waves being aliased to appear identical. Discrimination between different modes is difficult since most of our measurements are collected in the early afternoon (we did not record the exact local time for each vector). Based on discussions in Banfield et al. [2003], what MGS sees as wave 1 is probably dominated by stationary wave 1 with contributions from several non-migrating semidiurnal tides, what MGS sees as wave 2 at high latitudes is probably dominated by stationary wave 2. Banfield et al. [2003] find only small amplitude for wave 3, but it is likely that wave 3 is confined to the lower atmosphere where TES retrieval is not accurate enough (Don Banfield, personal communication).

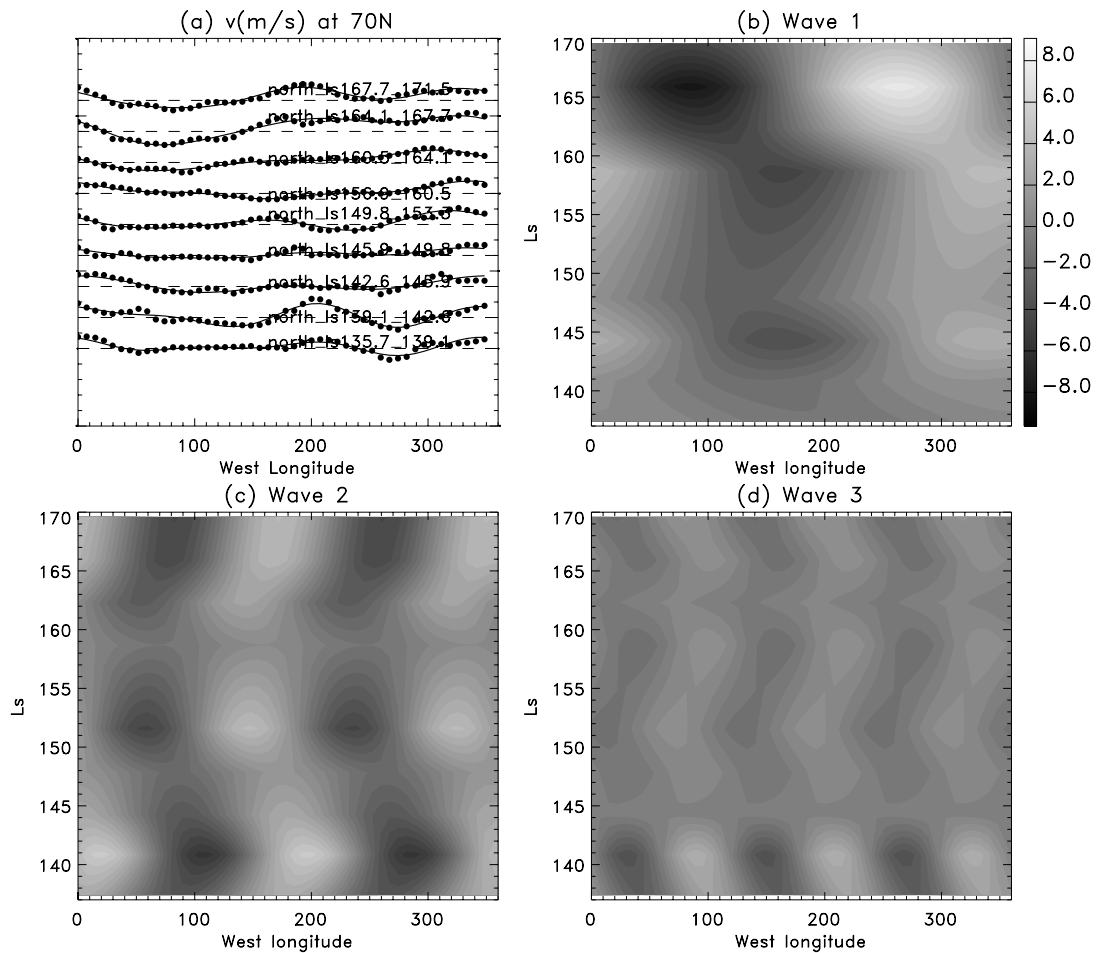


**Figure 3.10** (a) Meridional winds ( $v$ , m/s, dots) at  $70^\circ\text{N}$ . The curves are derived from Fourier components up to Wave 3. The dashed lines represent 0 m/s for each set of data. The Ls for each period is indicated in the plot. The longitude (west)-Ls cross sections for Wave 1, 2, and 3 are displayed in (b), (c) and (d). They use the same color bar next to (b).

### 3.6.2 Eddy momentum flux and eddy kinetic energy

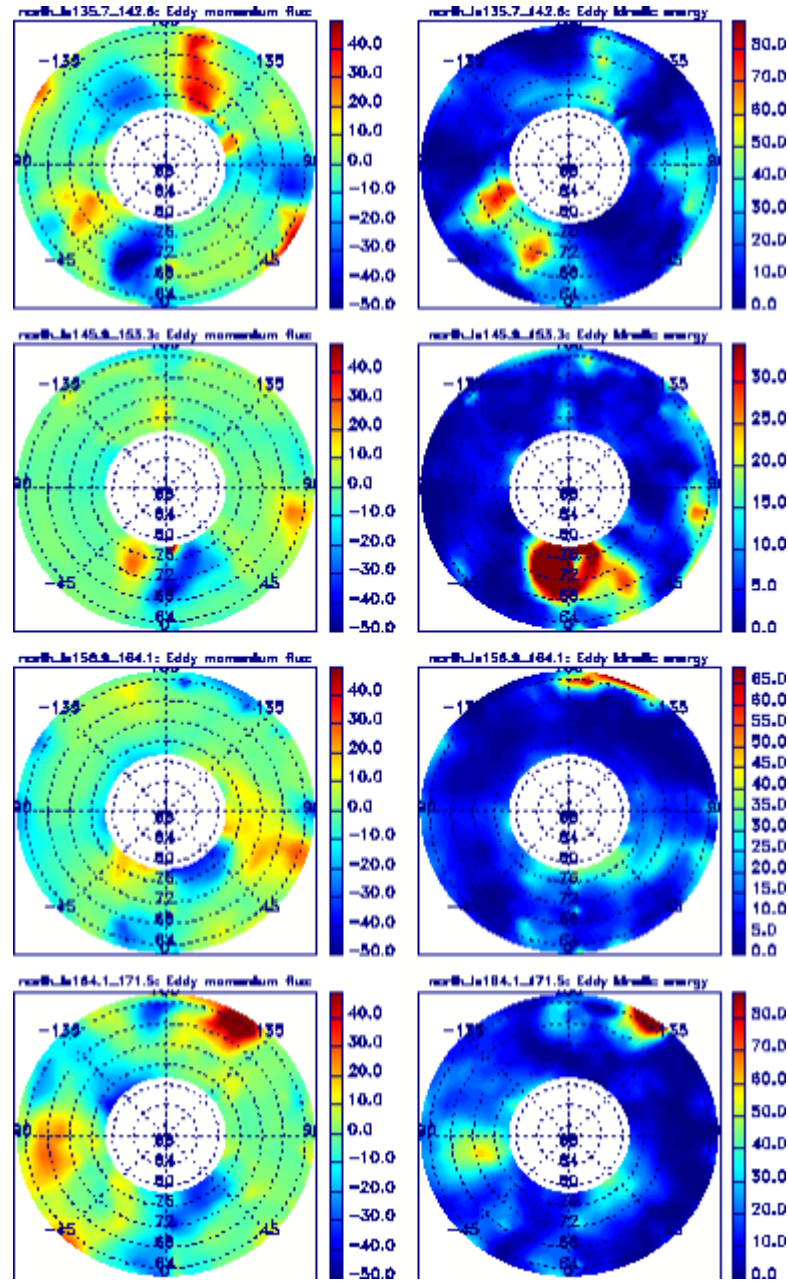
Plate 3.1 shows polar stereographic maps ( $62^\circ\text{N}$ - $78^\circ\text{N}$ ) of eddy momentum flux  $\overline{u'v'}$  and eddy kinetic energy  $(u'^2 + v'^2)/2$  for four 2-week periods that have good spatial coverage of cloud-tracked winds, where  $u' = u - \bar{u}$ ,  $v' = v - \bar{v}$ . Again, we assumed that the measured winds were at the same height. Positive value of eddy

momentum flux (red in the left panels of Plate 3.1) indicates poleward transport of eastward momentum or equatorward transport of westward momentum by the wave. Negative value (blue in the left panels of Plate 3.1) indicates poleward transport of westward momentum or equatorward transport of eastward momentum by the wave. The average eddy momentum fluxes for the four periods are slightly negative ( $> -2 \text{ m}^2/\text{s}^2$ ), but the spatial distribution for each period shows large scale waves with large amplitudes (up to  $40 \text{ m}^2/\text{s}^2$ ). Depending on the latitude and time, either Wave 2 or Wave 3 appears to dominate the spatial distribution of eddy momentum flux. The wave amplitudes for  $L_s$   $135.7^\circ$ - $142.6^\circ$  and  $L_s$   $164.1^\circ$ - $171.5^\circ$  appear larger than those for  $L_s$   $145.9^\circ$ - $153.3^\circ$  and  $L_s$   $156.9^\circ$ - $164.1^\circ$ . The detailed distribution also changes from one period to another. For example, positive eddy momentum flux occurs in the  $135^\circ\text{E}$ - $180^\circ\text{E}$  sector during  $L_s$   $135.7^\circ$ - $142.6^\circ$  and  $L_s$   $164.1^\circ$ - $171.5^\circ$ , but not during  $L_s$   $145.9^\circ$ - $153.3^\circ$  and  $L_s$   $156.9^\circ$ - $164.1^\circ$ . However, there appears to be a persistent positive-negative-positive wave pattern with respect to longitude in the  $60^\circ\text{W}$ - $0^\circ$ - $90^\circ\text{E}$  sector (northeast of Tharsis), though the wave pattern shifts slightly in longitudes for different periods. Referring to Fig. 3.3, we see that the shift appears to be associated with the shift in the position of the cyclonic gyre in the  $90^\circ\text{W}$ - $0^\circ$ - $30^\circ\text{E}$  sector. The eddy kinetic energy maps for the four periods are shown in the right columns of Plate 3.1. Regions of large eddy kinetic energy correspond to regions of large positive or negative eddy momentum flux. Although different periods have different activity centers, all the centers occur in the  $90^\circ\text{W}$ - $0^\circ$ - $60^\circ\text{E}$  (Acidalia),  $135^\circ\text{E}$ - $180^\circ\text{E}$  (Arcadia) sectors, and around  $90^\circ\text{E}$  (Utopia). Hollingsworth et al. [1996] simulated strong eddy

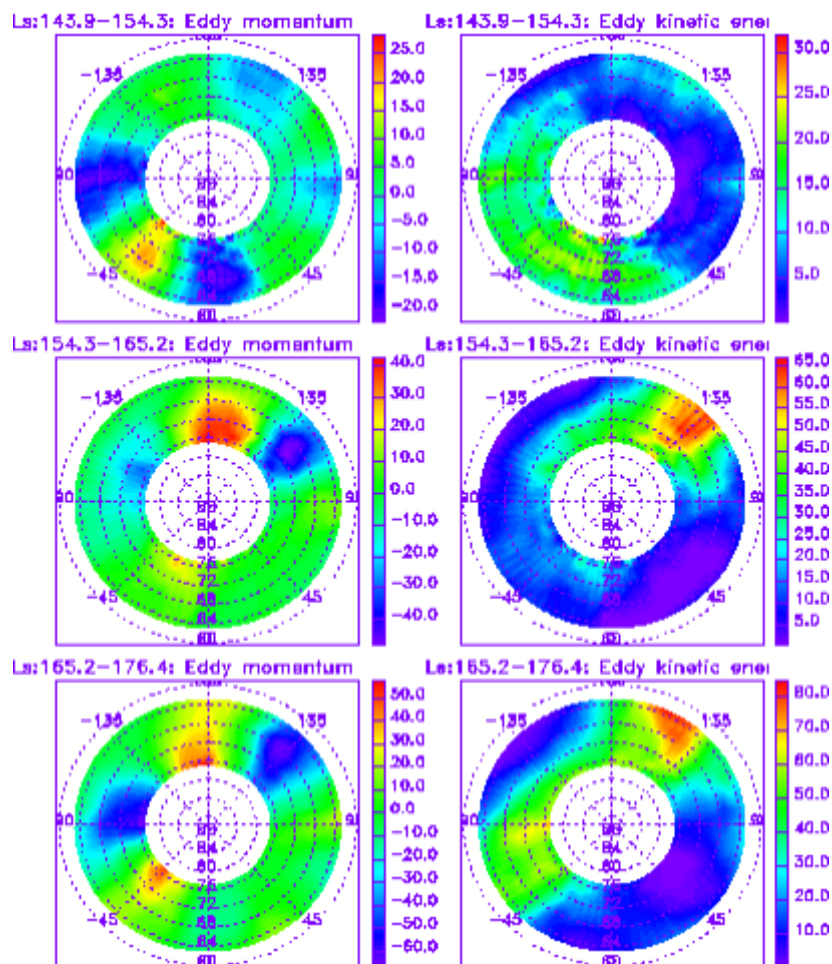
activities in these regions using NASA Ames GCM, and pointed out that they are controlled by topography.

Plate 3.2 shows the eddy momentum flux and eddy kinetic energy at 225 Pa (~10.6 km) simulated by the GFDL Mars GCM [Wilson and Hamilton, 1996; Richardson and Wilson, 2002] for three periods corresponding to the last three rows of Plate 3.1. The simulated winds are sampled at 2 PM local time before they are time averaged within the period.  $u'$  and  $v'$  are derived by subtracting the zonal mean and used to calculate the eddy momentum flux and eddy kinetic energy. The results reproduce several features displayed in Plate 3.1. (1) Large scale waves are present. (2) There is persistent positive eddy momentum flux with relatively large eddy kinetic energy northeast of Tharsis (longitude ~0-60°W). (3) There is reasonable correspondence of the position of certain highs and lows between the observation and simulation. For example, the observed strong eddy kinetic energy regions in the 135°E-180°E and 60°W-105°W sector during  $L_s$  164.1°-171.5° correspond well with the simulation results for  $L_s$  165.2°-176.4°. However, the observed positive-negative-positive eddy momentum flux pattern is not apparent in Plate 3.2. The area of large eddy kinetic energy is larger than that shown in Plate 3.1. The simulation results appear to emphasize waves in the 90°W-135°W-180°-135°E-90°E hemisphere. There are also some detailed differences. For example, the simulated eddy kinetic energy distribution in the 135°E-180°-135°W sector during  $L_s$  165°-176° is almost out of phase with the observed distribution during  $L_s$  164°-171°. The same analysis performed for 302 Pa (~7.4km, not shown) leads to very similar wave patterns as those shown in Plate 3.2, but the wave amplitudes are much smaller, and the maximum positive eddy

momentum flux is sometimes much less than the absolute value of the minimum negative eddy momentum flux.



**Plate 3.1** Eddy momentum flux ( $u'v'$ , m<sup>2</sup>/s<sup>2</sup>, left panels) and eddy kinetic energy ( $0.5*(u'^2+v'^2)$ , m<sup>2</sup>/s<sup>2</sup>, right panels) derived from cloud-tracked winds. Ls is indicated above each panel. Longitudes in the panels are east longitudes, latitudes are north latitudes.



**Plate 3.2** Eddy momentum flux ( $u'v'$ ,  $m^2/s^2$ , left panels) and eddy kinetic energy ( $0.5*(u'^2+v'^2)$ ,  $m^2/s^2$ , right panels) derived from winds at 224 Pa simulated by the GFDL Mars GCM. Ls is indicated above each panel. Longitudes in the panels are east longitudes, latitudes are north latitudes.

### 3.7 Summary

We measured cloud-tracked winds for the first MGS mapping year using MOC wide angle global map swaths. Due to the limitations of the data, our measurements are concentrated in the north polar region during Ls  $135^\circ$ - $195^\circ$  and Ls  $20^\circ$ - $55^\circ$ , and in the south polar region during Ls  $337^\circ$ - $10^\circ$ . We do not have direct information about

cloud height. Smith [2002] estimated the altitude of the water vapor condensation level to be in the range 5-10 km during the season of our north polar measurements. At this altitude, the wind speeds computed by the NASA Ames GCM generally agree with our measurements. For the south polar region, we tracked dust clouds using red images. The measured winds are much weaker than the GCM simulated winds at the water vapor condensation level (~10 km). This suggests that the height of the observed dust clouds was lower than 10 km since GCM predicts slower wind speed at lower altitude. The observed mean zonal wind increases from late summer to early fall in both hemispheres, and decreases in the spring in the north polar region. In the north, the zonal wind increase from late summer to early fall appears larger at the higher latitudes. The curvature of the absolute vorticity within 60°N-70°N indicates the possibility of barotropic instability during Ls 135°-195°. A cyclonic gyre in the 90°W-0°-30°E sector at northern high latitudes is observed. It is associated with large eddy momentum fluxes and eddy kinetic energy, and implies poleward transport of water vapor at the level of observed clouds. The longitudinal distribution of meridional winds at 70°N indicates the presence of large scale waves during Ls 135°-171°. The Wave 2 and 3 components appear to oscillate in phase and amplitude. Due to the sampling strategy of MGS, waves derived from our data could contain stationary waves and certain modes of thermal tides. Wave 1 and 2 are probably dominated by stationary waves. Wave 3 is probably confined in the lower atmosphere. Large amplitude waves are also observed in the eddy momentum flux field. There appear to be a positive-negative-positive pattern northeast of Tharsis. Consistent with GCM simulations, strong eddy activities exist in northern Acidalia, Arcadia and Utopia.

These locations also correspond to the southward meridional winds of Wave 3. Our measured winds are stronger than the gradient winds at the water vapor condensation level derived from TES. However, uncertainties in our measurements (velocity, height), TES retrieval, and GCM simulations greatly complicate comparisons between them. Future work is needed to better understand the results presented here and to use them to constrain atmospheric models.

### 3.8 References

- Banfield, D., B. J. Conrath, M. D. Smith, P. R. Christensen, and R. J. Wilson, Forced waves in the martian atmosphere from MGS TES nadir data, *Icarus*, 161, 319-345, 2003.
- Haberle, R. M., J. B. Pollack, J. R. Barnes, R. W. Zurek, C. B. Leovy, J. R. Murphy, H. Lee, and J. Schaeffer, Mars atmospheric dynamics as simulated by the NASA Ames general circulation model, 1. the zonal-mean circulation, *J. Geophys. Res.*, 98, 3093-3123, 1993.
- Hess, S., R. Henry, C. Leovy, J. Ryan, and J. Tillman, Meteorological results from the surface of Mars: Viking 1 and 2, *J. Geophys. Res.*, 82, 4559-4574, 1977.
- Hollingsworth, J. L., R. M Haberle, J. R. Barnes, A. F. C. Bridger, J. B. Pollack, H. Lee, J. Schaeffer, Orographic control of storms zones on Mars, *Nature*, 380, 413-416, 1996.
- Kahn, R., and P. Gierasch, Long cloud observations on Mars and implications for boundary layer characteristics over slopes, *J. Geophys. Res.*, 87, 867-880, 1982.

- Kahn, R., Some observational constraints on the global-scale wind systems of Mars, *J. Geophys. Res.*, 88, 10,189-10,209, 1983.
- Malin, M. C., and K. S. Edgett, The Mars Global Surveyor Mars Orbiter Camera: Interplanetary cruise through Primary mission, *J. Geophys. Res.*, 106, 23,429-23,570, 2001.
- Mischna, M. A., J. F. Bell, III, P. B. James, and D. Crisp, Synoptic measurements of Martian winds using the Hubble Space Telescope, *GRL*, 25, 611-614, 1998.
- Richardson, M. I. and R. J. Wilson, Investigation of the Martian seasonal water cycle with a general circulation model, *J. Geophys. Res.*, 107, 5031, doi: 10.1029/2011JE001536, 2002.
- Salby, M. L., *Fundamentals of atmospheric physics*, pp 517-523, Academic press, San Diego, California, 1996.
- Smith, M. D., J. C. Pearl, B. J. Conrath, and P. R. Christensen, Thermal Emission Spectrometer results: Mars atmospheric thermal structure and aerosol distribution, *J. Geophys. Res.*, 106, 23,929-23,945, 2001.
- Smith, M. D., The annual cycle of water vapor on Mars as observed by the Thermal Emission Spectrometer, *J. Geophys. Res.*, 107, 5115, doi: 10.1029/2001JE001522, 2002.

Sullivan, R., R. Greeley, M. Kraft, G. Wilson, M. Golombek, K. Herkenhoff, J. Murphy, and P. Smith, Results of the imager for Mars Pathfinder windsock experiment, *J. Reophys. Res.*, 105, 24547-24562, 2000.

Wang, H. and A. P. Ingersoll, Martian clouds observed by Mars Global Surveyor Mars Orbiter Camera, *J. Geophys. Res.*, 107, 5078, doi: 10.1029/2001JE001815, 2002.

Wilson, R. J., and K. Hamilton, Comprehensive model simulation of thermal tides in the Martian atmosphere, *J. Atmos. Sci.*, 53, 1290-1326, 1996.

### **3.9 Acknowledgements**

We thank Michael D. Smith for providing us gradient winds in digital form. We thank Mark I. Richardson for providing output from GFDL Mars GCM. We thank Don Banfield and an anonymous reviewer for comments about improving this paper. We thank Mark Richardson and R. John Wilson for providing GFDL Mars GCM outputs.

**Chapter 4: Martian Clouds Observed by the Mars  
Global Surveyor Mars Orbiter Camera. Results for the  
Second Martian Year**

Huiqun Wang and Andrew P. Ingersoll

Division of Geological and Planetary Sciences,  
California Institute of Technology, Pasadena

## 4.1 Introduction

Global map swaths taken from Feb 2001 to Jan 2002 were released in Oct 2002. These data span  $L_s$  110°-319° of the second Martian year (Results for the first Martian year are summarized in Chapter 1). We processed these images using the same method as that in Wang and Ingersoll [2002]. In this Chapter, we will describe the Martian clouds observed from these new data and compare them with those observed in the first Martian year.

## 4.2 The 2001 global dust storm

The 2001 global dust storm highlights the difference between the first and second Martian year. Smith et al. [2002] described the development of this storm using dust opacities derived from the Thermal Emission Spectrometer (TES). They observed rapid expansion of a local dust storm in Hellas ( $L_s \sim 185^\circ$ ) to global scale within ~2weeks, the associated warming of the atmosphere, and the increase in the amplitudes of thermal tides. In this section, we will discuss this global dust storm using MOC data.

### 4.2.1 Effects on photometric processing

The 2001 global dust storm has a mean optical depth of  $\sim 1.2$  at  $1075 \text{ cm}^{-1}$  [Smith et al., 2002]. The presence of significant amount of atmospheric dust on global scales changed the photometric behavior of Mars. Figure 4.1 compares a pair of processed red and blue swaths (a and c) at  $L_s$  190° in the first Martian year (no global dust storm) with a pair of processed red and blue swaths (b and d) that covered

approximately the same surface area at the same  $L_s$  in the second Martian year (after the onset of the 2001 global dust storm). The same processing procedure of dividing the Data Number (DN) of each pixel in the radiometrically calibrated image by the value calculated from the photometric function in Wang and Ingersoll [2002] is applied for all the global map swaths. Our photometric processing flattened both the red and the blue images reasonably well before and after the 2001 global dust storm (Fig. 4.1 ac). However, the same procedure makes the pixels with small phase angles darker during the storm (Fig. 4.1bd, black arrows point to pixels with zero phase angles), indicating an over-correction of the opposition surge (increase in brightness toward zero phase angle). This suggests that atmospheric dust suppresses the surface opposition effect.

Thorpe [1978] noticed suppressed opposition surges during global dust storms observed by Viking, and concluded that opposition surge was a surface effect instead of an atmospheric effect. Including an atmospheric optical depth parameter into the photometric function could better flatten the images during a global dust storm. Thorpe [1978] suggested such a function for the total planetary reflectance which involves the atmospheric particle phase function, the surface phase function, the atmospheric reflectance and transmission as functions of the optical depth and geometry. Hapke [1986] developed an analytic function for the surface bi-directional reflectance that includes the opposition effect. Our photometric function is modified from Hapke's function. Since we over-corrected the opposition surge during the global dust storm, we divide each image by an average image (derived by averaging

photometrically processed images taken during the global dust storm) [Wang and Ingersoll, 2002] to produce better flattened image for making the daily equatorial map.

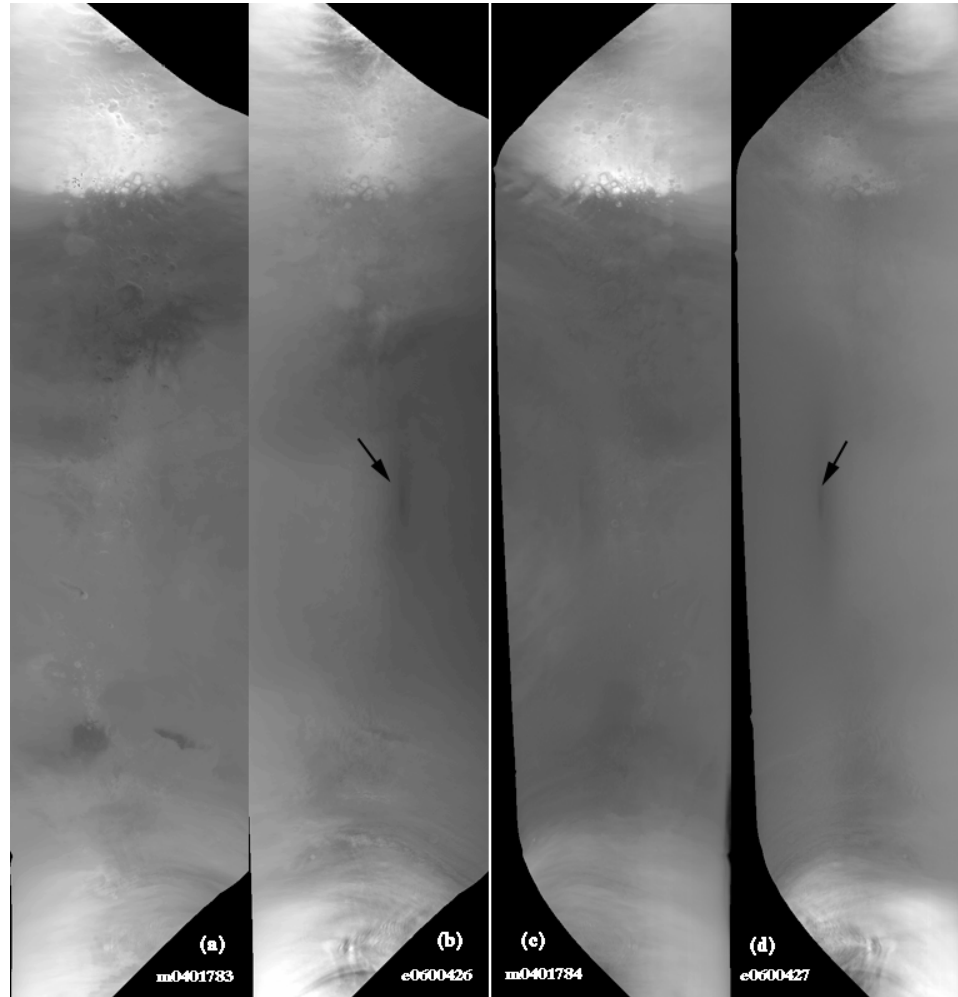


**Figure 4.1** Processed red images (a) m0401783 from Year 1 and (b) e0600426 from Year 2, and processed blue images (c) m0401784 from Year 1 and (d) e06004427 from Year 2.

### 4.2.2 Storm evolution

The development of the 2001 global dust storm is shown in Fig. 4.2. A local Hellas dust storm at  $L_s \sim 179^\circ$  transported significant amount of dust out of the basin (Fig. 4.2a), signaling the beginning of the 2001 global dust storm. The region in and

around Hellas remained a continuous dust source for the following ~3.5 weeks (Fig. 4.2bc). During this period (Ls 179°~190°), multiple storm centers occurred in the eastern hemisphere as the lofted dust traveled eastward and expanded in latitude. Of these storm centers, some occurred at northern low to mid latitudes (around Syrtis and the dark albedo feature in Utopia), others near the south polar cap (Fig. 4.2d). During Ls 140°~186°, local dust storms occurred at the edge of seasonal south polar cap, but did not generate apparent visual effects above the cap (Fig. 4.3a). At Ls ~186°, a large amount of dust was blown onto the south polar cap by powerful dust storms originating in the Hellas basin (Fig. 4.3bc). The dust then encircled the south pole within about a week, at which point (Ls ~191°) large regional dust storms emerged at the cap edge in the 0°-90°W-180°W sector (Fig. 4.3e), shooting northward to the southern low latitudes (Fig. 4.2e). These active cap edge storms lasted for about 10 sols, shifting the active storm centers from the eastern to the western hemisphere. By Ls ~199°, the whole south polar region appeared dusty and cap edge storms could no longer be recognized in the south polar map (Fig. 4.3f). However, active dust storm centers in/around Solis Planum can be recognized every day during Ls 199°~207° in the equatorial map (Fig. 4.2f), making the atmosphere dustier. The shift of active storm centers from Hellas to Solis was also observed from TES data [Smith et al., 2002]. Solis dust storms continued to contribute dust into the atmosphere before Ls ~230°, though the frequency was less than before. The 2001 global dust storm resulted from not only the Hellas storms but also the cap edge dust storms and Solis dust storms. The atmosphere began to clear after Ls ~230°, and surface features could be clearly seen by Ls ~260°.

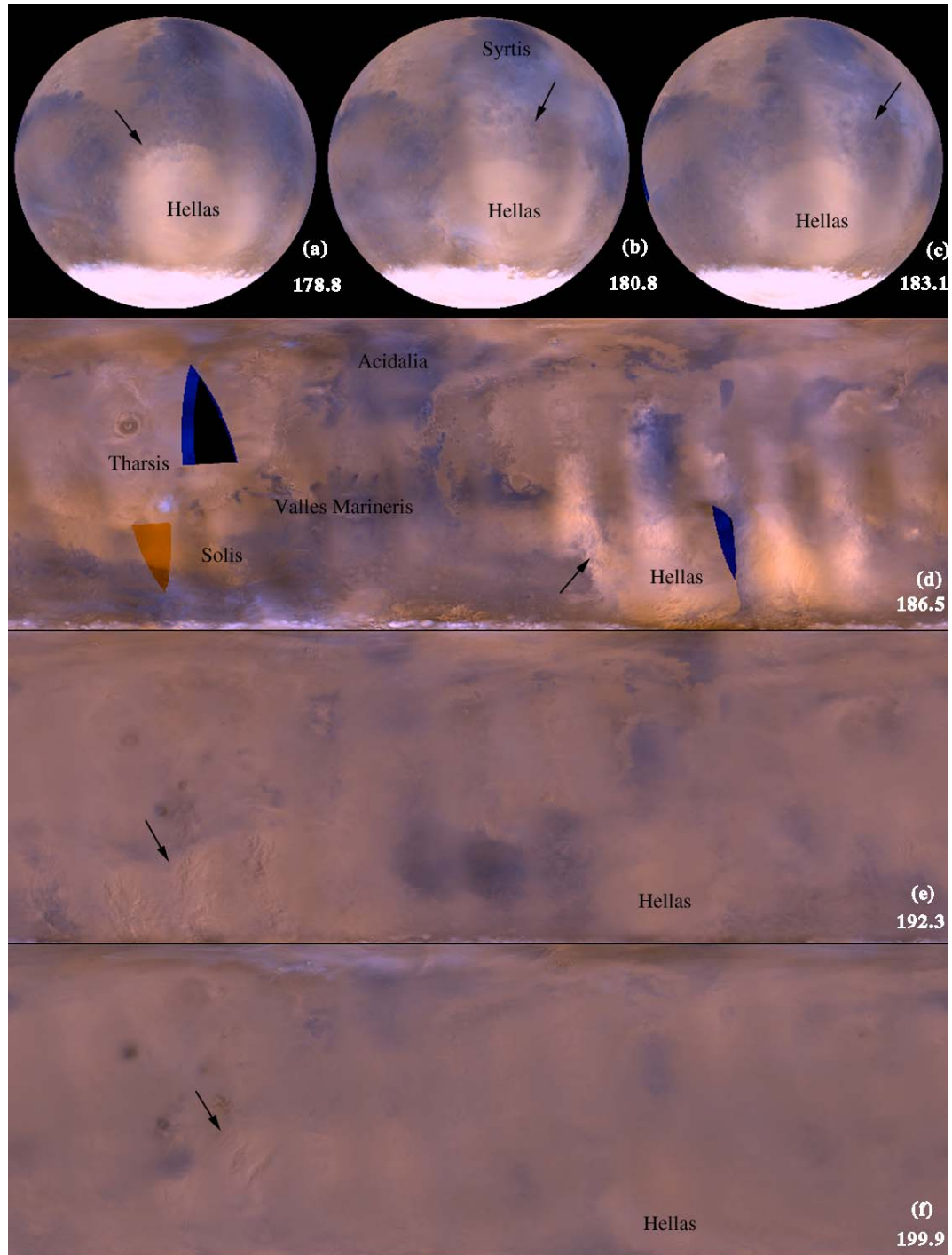


**Figure 4.2** Evolution of the 2001 global dust storm. Dust is indicated by black arrows. (a-c) Daily global maps wrapped on a sphere (satellite projection). White area at the bottom is the seasonal south polar cap. (d-f) equatorial maps (60S-60N). White blobs near 60N are clouds in the north polar hood. White blobs near 60S in (d) is the northern edge of the seasonal south polar cap.

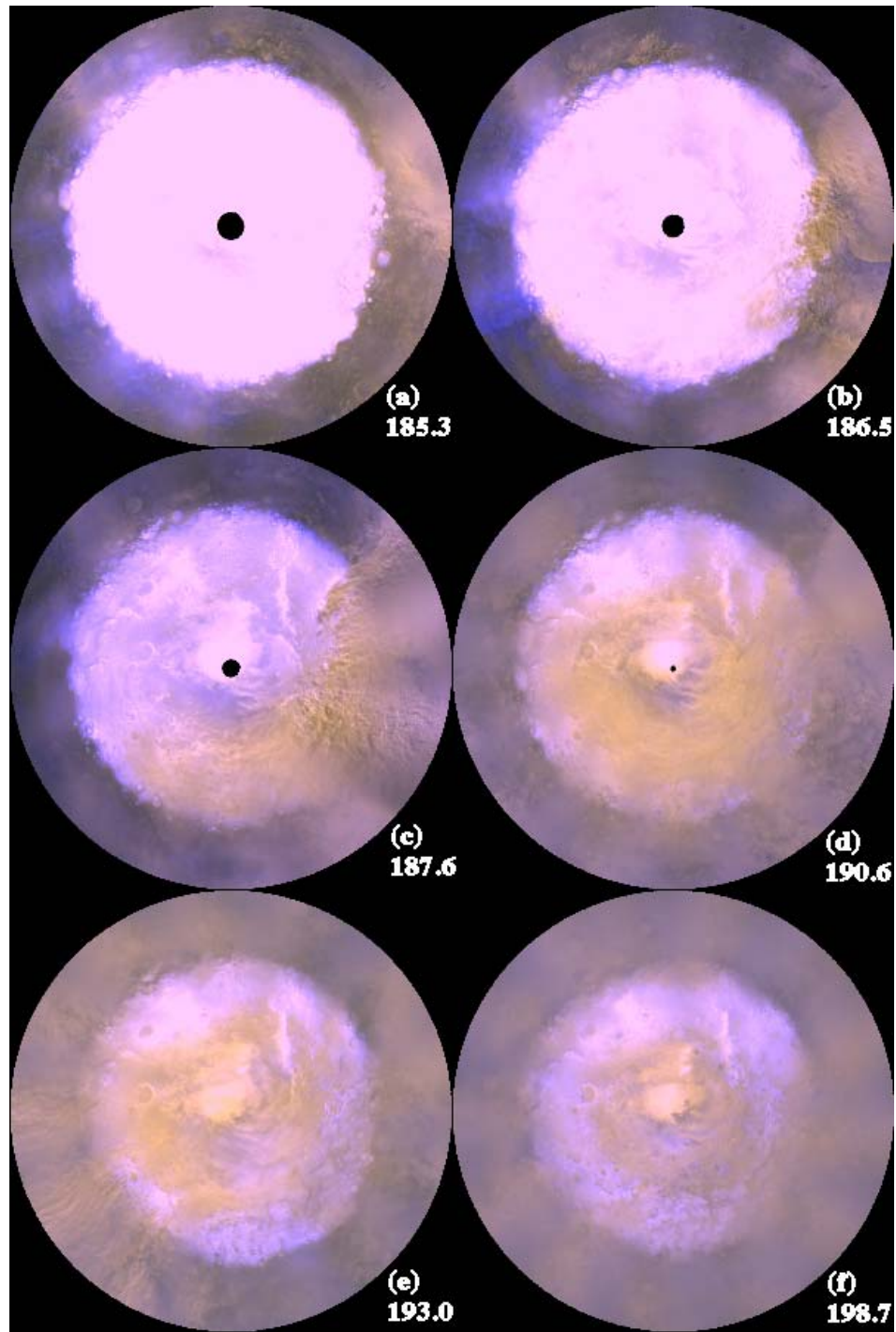


**Figure 4.3** South polar maps during the development of the 2001 global dust storm.

### 4.2.3 Effects on surface albedo

Comparing equatorial maps after the 2001 global dust storm with those at the same  $L_s$  in the previous Martian year (arrows, Fig. 4.4), we find apparent brightening in Hellas, Syrtis, and Solis relative to their surroundings. Surface features in these regions are clearly seen. Moreover, animation of daily global maps shows that the features do not change from day to day. These suggest that the brightening occurred at the surface. The three regions were once active dust storm centers at various stages of the global dust storm development. The brightening could imply that relatively dark dust was blown away revealing the underlying brighter surface. It could also imply that relatively bright dust favorably settled on these areas during the decline of the global dust storm. Surface brightening of northern hemisphere dark regions (e.g. Syrtis, Acidalia) was also observed after the 1977 Viking global dust storms [Christensen, 1988]. However, dark regions in the southern hemisphere were reported to be not measurably brighter following the 1977 global dust storms [Christensen, 1988].

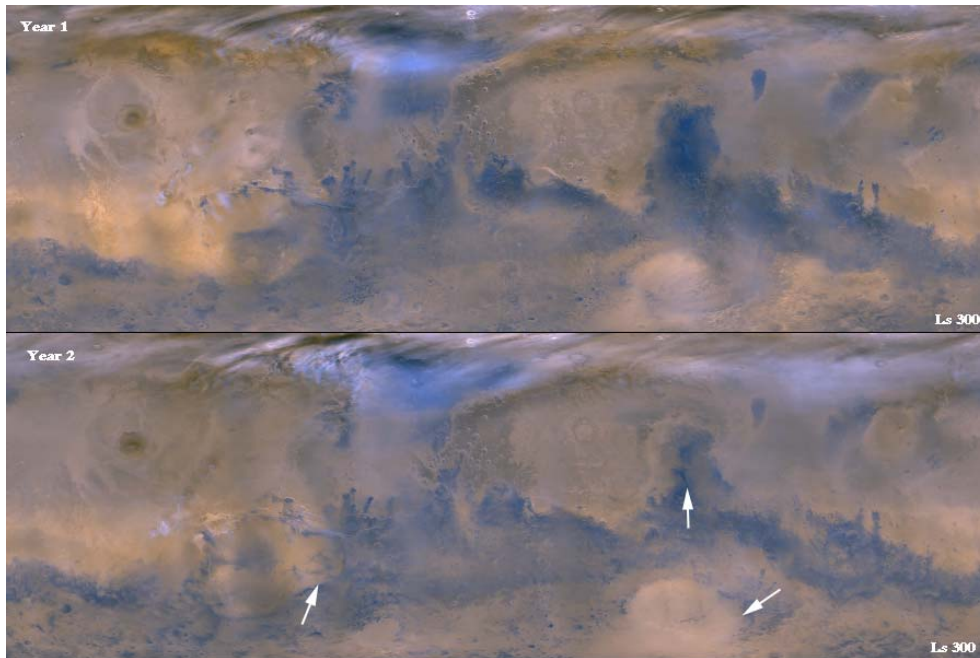


**Figure 4.4** Equatorial maps at Ls 300 for the first and second Martian year.

#### 4.2.4 Effects on polar clouds

During the clearing phase of the 2001 global storm (Ls 230°-260°), local cap edge dust storms were observed around the shrinking south polar cap. They are similar to those in the previous Martian year. However, after the global dust storm, there were very few local dust storms around the south polar cap (Fig. 4.5). While in the previous Martian year, active cap edge dust storms lasted until Ls ~275° before the whole region became clear (Fig. 4.5). It is possible that the 2001 global dust storm depleted the south polar dust source or the atmospheric condition right after the 2001 global storm did not favor the generation of local dust storms.

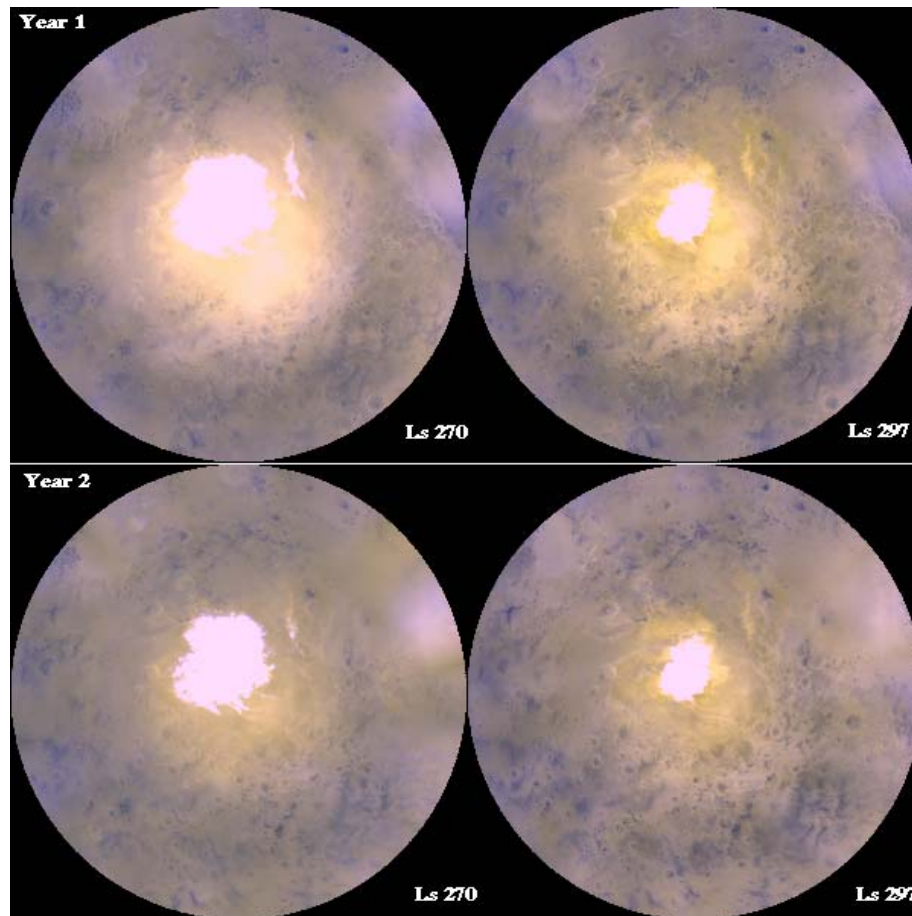


**Figure 4.5** South polar maps at  $L_s 270^\circ$  and  $297^\circ$  for the first and second Martian year.

Smith et al. [2002] observed a very steep latitudinal temperature gradient in  $40^\circ\text{N}$ - $70^\circ\text{N}$  that greatly strengthened the polar vortex which served as an effective barrier against northward dust transport during the 2001 global dust storm. Figure 4.6 compares representative north polar maps during the 2001 global dust storm (c, d) with those at the same  $L_s$  in the previous Martian year. The polar hood appeared to have less condensate clouds, smaller spatial extent and more axisymmetric shape during the global dust storm, though typical polar hood clouds (including streak clouds, lee waves, haze, and local dust storms) dominated the north polar region in both years. This is consistent with the simulated meridional expansion of enhanced

Hadley cell under high dust loading [Haberle et al., 1993]. Wilson [1997] simulated polar warming during global dust storm. He found a high degree of axisymmetry for the polar vortex and marked reduction in transient (non-tidal) and stationary wave activity. North polar clouds before and after the global dust storm are very similar between the two Martian years. This will be discussed in Section 4.4.2.

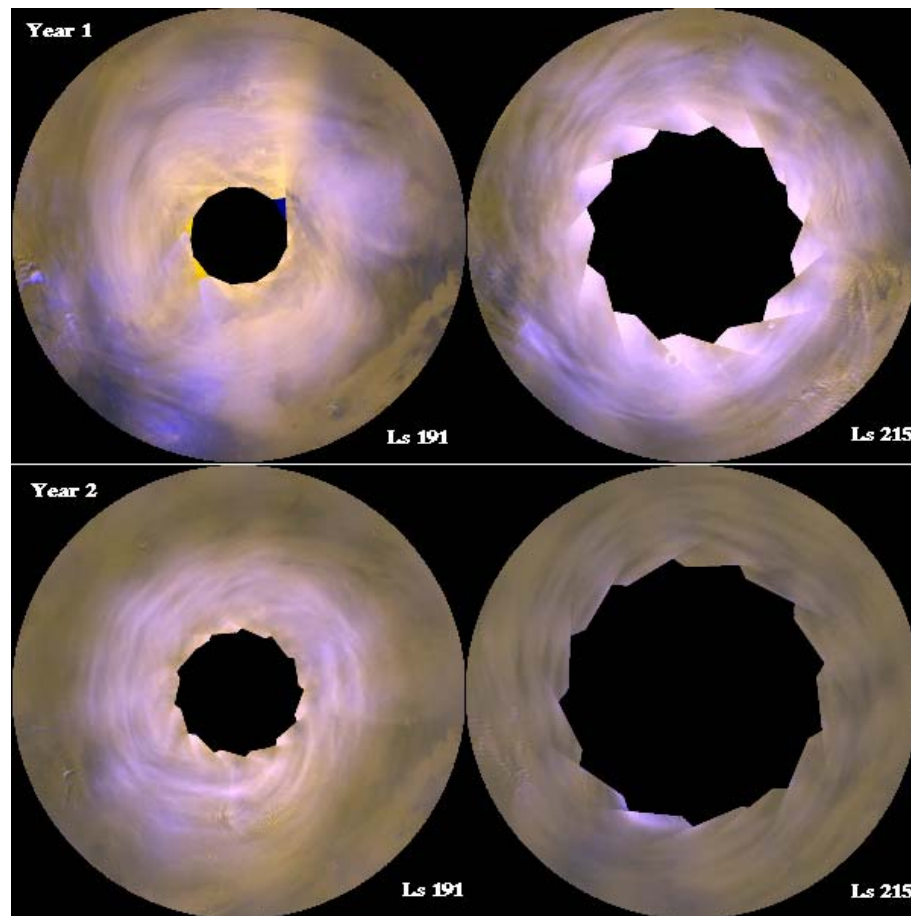


**Figure 4.6** North polar maps at Ls 191 and 215 in the first and second Martian year.

### 4.2.5 Global dust storm initiation

Smith et al. [2002] noticed a number of local dust storms in and around Hellas before the onset of the 2001 global dust storm (at Ls 185°) using TES data. Using

MOC data, we find that wintertime Hellas dust storms had similar frequency, size and even morphology before  $L_s \sim 185^\circ$  between the two Martian years (Fig. 4.7 and Fig. 4.8). At  $L_s \sim 180^\circ$  of the first Martian year, Hellas dust storms blew out of the northern slope continuously for three sols (Fig. 4.7bcd). The suspended dust lingered north of Hellas for about a week and dissipated (Fig. 4.7e). Although there were additional Hellas storms after this event, they were confined within the basin, and did not appear to contribute significant amount of dust outside Hellas (Fig. 4.7f). At  $L_s \sim 178^\circ$  of the second Martian year, a similar event happened. The sequence of dust storms (Fig. 4.8bcd) is very similar in morphology and history to that in the first Martian year (Fig. 4.7bcd). However, before the dust was dissipated, additional Hellas storms blew more dust out of the basin (Fig. 4.8f), which sustained the level of dustiness in the southern subtropics. As the suspended dust spreaded eastward, additional dust storm centers appeared to be triggered in the western hemisphere and northern hemisphere. The sequence of events eventually led to a global dust storm. The comparison between the two Martian years suggests that sufficient supply of dust to the southern subtropics within a short time period could facilitate global dust storm initiation. When dust accumulates in the Hadley cell convergence zone, the circulation greatly strengthens [Wilson, 1997]. This could provide a positive feedback for additional dust lifting by stronger surface stress.

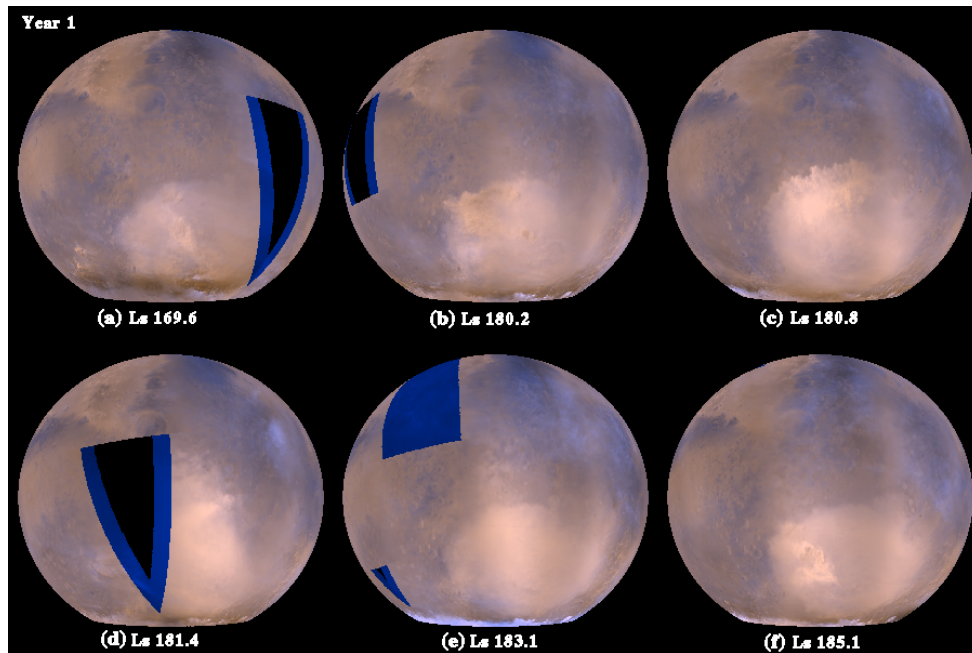


**Figure 4.7** Hellas dust storms in the first Martian year. Each image has the same satellite projection as that for Fig. 4.2a-c, except that only the area north of 60°S is shown.

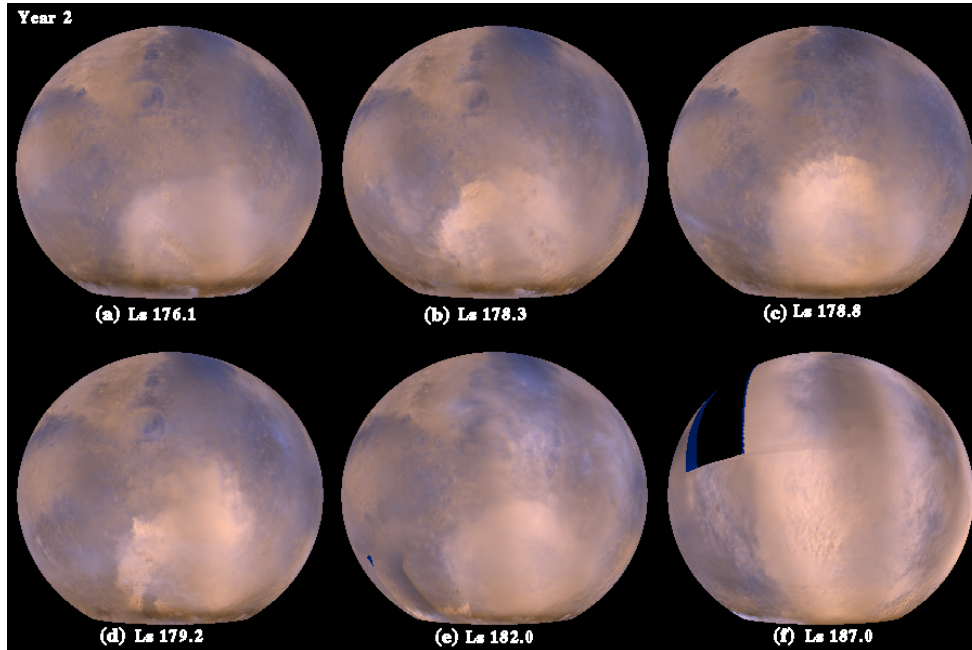


**Figure 4.8** The same as Fig. 4.7, but for the second Martian year.

### 4.3 Global condensate cloud distribution

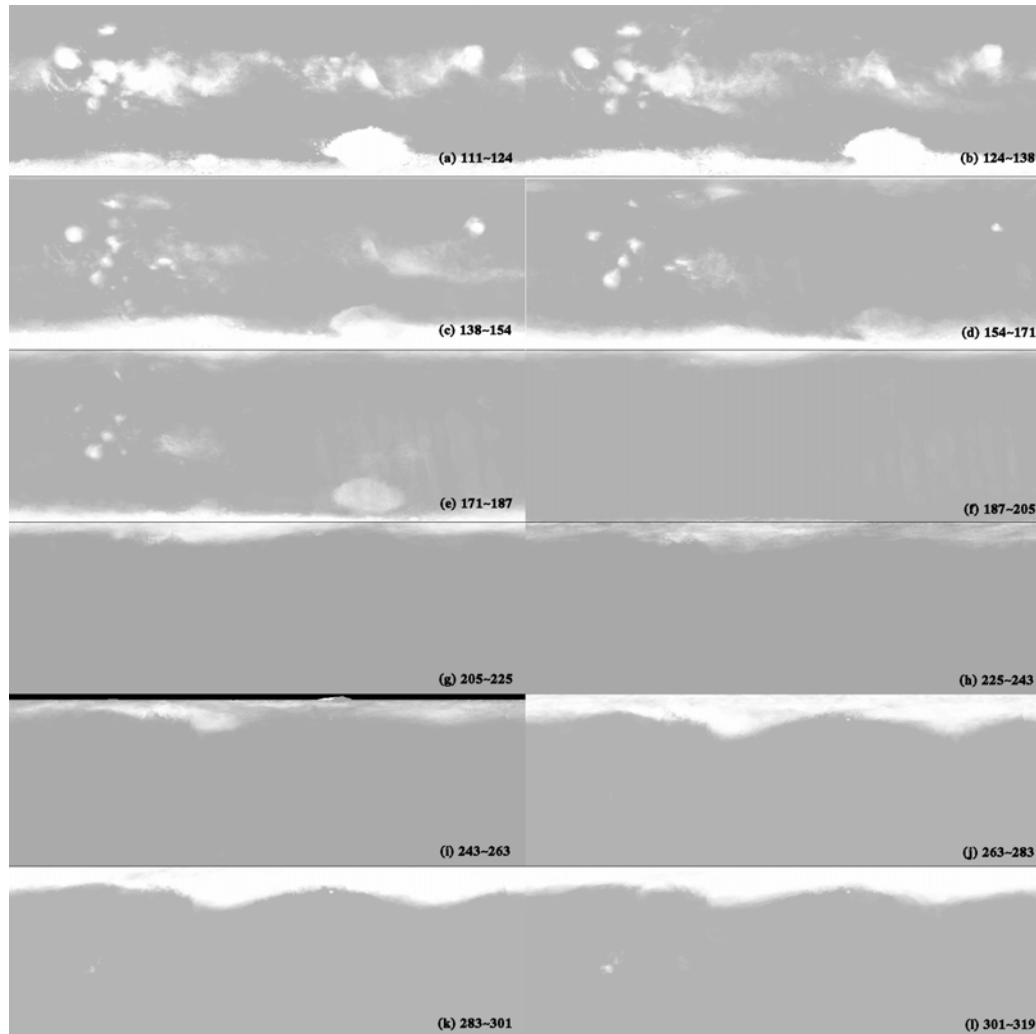


**Figure 4.9** Cloud occurrence frequency maps for the second Martian year.

Using the method described in Wang and Ingersoll [2002] Section 3, we derived cloud occurrence frequency maps ( $60^{\circ}\text{S}$ - $60^{\circ}\text{N}$ ) for each month of the second Martian year (Fig. 4.9). Cloud identification is based on brightness contrast between clouds and background in the blue equatorial maps, so the identified clouds include the polar caps, condensate clouds and thick local or regional dust storms. Although the 2001 global dust storm greatly raised the background optical depth, it had little contribution

to Fig. 4.9(f-i) because of the low contrast of dust in blue images. Figure 4.9 shows the recession of the south polar cap and hood in southern winter, the growth of the north polar cap and hood in northern fall, and the decay of the equatorial cloud belt in northern summer. Neumann et al. [2003] noticed that clouds tracked the advancing and receding edges of the seasonal polar caps using Mars Orbiter Laser Altimeter (MOLA) data.

The two Martian years overlap in the period from mid northern summer to mid northern winter ( $L_s$  135°~319°). Figure 4.9 is similar to Fig. 2 of Wang and Ingersoll [2002] in the following aspects: The tropical cloud belt disappeared in late northern summer; topographic clouds over the volcanoes lasted longer than clouds in other parts of the cloud belt; clouds over Arsia Mons appeared first in southern summer; the south polar cap and hood receded south of 60°S shortly after the southern spring equinox when the north polar hood grew south of 60°N; Hellas basin remained cloudy longer than other areas at the same latitudinal bands; the north polar hood had a longitudinal wave 2 structure.

The main difference between the two years is the timing of the disappearance and appearance of topographic clouds over the volcanoes. No tropical clouds were identified during the 2001 global dust storm in the second year ( $L_s$  185°~280°, Fig. 4.9 f-j), while Arsia (120°W, 9°S) clouds in the first Martian year lasted until  $L_s$  ~235° and reappeared at  $L_s$  ~255°. The early disappearance and late appearance of Arsia clouds in the second year is consistent with the increased atmospheric temperatures (~40°K at 0.5 mb) during global dust storm [Smith et al., 2002].

In order to compare the tropical cloud belt decaying phases of the two Martian years in detail, we generated cloud occurrence frequency maps every  $10^\circ$  of  $L_s$  during  $L_s$   $135^\circ\sim 180^\circ$  for each year (Fig. 4.10). We still find similarities on this timescale. In both Martian years, the clouds in the tropical cloud belt dissipated first in Arabia Terra, second in the eastern hemisphere, then around Valles Marineris, and last above the volcanoes. There are some detailed differences. For example, the clouds north of Valles Marineris during  $L_s$   $135^\circ\sim 145^\circ$  in the first year appeared more frequent and spatially extensive; the Elysium clouds in the first year also appeared to last longer.

The meridional streamfunction simulated by the NASA Ames GCM shows rising motion within  $20^\circ\text{S}\text{-}20^\circ\text{N}$  during  $L_s$   $140^\circ\sim 166^\circ$  [Haberle et al., 1993]. The position of the ascending branch of the circulation agrees with the position of the cloud belt. Temperature decreases within the rising air due to adiabatic cooling, producing favorable condition for condensation. Formation of water ice clouds is also controlled by the water vapor abundance. During  $L_s$   $135^\circ\sim 180^\circ$  in the first Martian year, the column water vapor at  $20^\circ\text{N}$  gradually decreases from  $\sim 25$   $\mu\text{m}$  to  $\sim 23$   $\mu\text{m}$ , that near the equator increases from  $\sim 15$   $\mu\text{m}$  to  $\sim 23$   $\mu\text{m}$ , and that at  $20^\circ\text{S}$  increases from  $\sim 6$   $\mu\text{m}$  to  $\sim 15$   $\mu\text{m}$  [Smith, 2002]. Richardson et al. [2003] simulated water ice clouds using GFDL Mars GCM. Their results show reasonable agreement with our observations. They also show that the decline of the tropical cloud belt in mid northern summer is related to an increase in air temperatures, rather than to decreases in water vapor supply or the vigor of Hadley circulation.

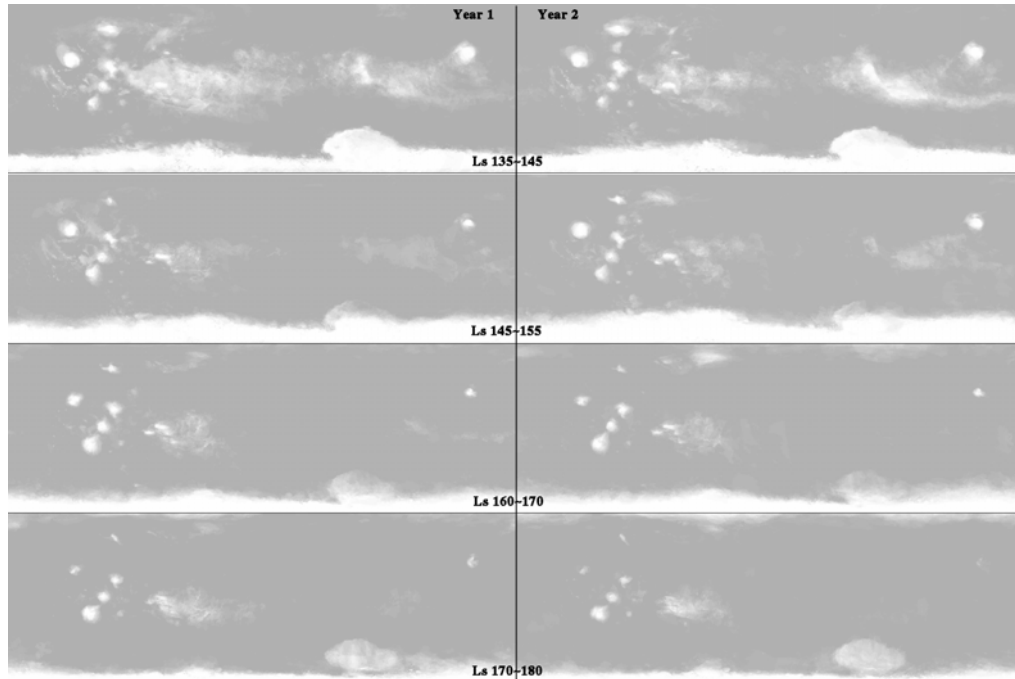


**Figure 4.10** Decaying tropical cloud belt in the first and second Martian year.

## 4.4 Recurrent phenomena

Although there was no global dust storm in the first Martian year, all types of clouds observed in the first year were observed in the second year. Many recurred in approximately the same location and time of year. Cantor et al. [2002] noticed repeated weather phenomena (annular clouds, Valles Marineris dust storms, dust cells and devils) during  $L_s$   $124^\circ\sim 140^\circ$ . Our study suggests that recurrent weather phenomena on Mars span a much larger range of  $L_s$  than that reported by Cantor et al [2002]. In the previous sections, we described repeated Hellas dust storms and tropical cloud belt evolution. In this section, we will discuss several other types of recurrent Martian clouds.

#### 4.4.1 Aster clouds

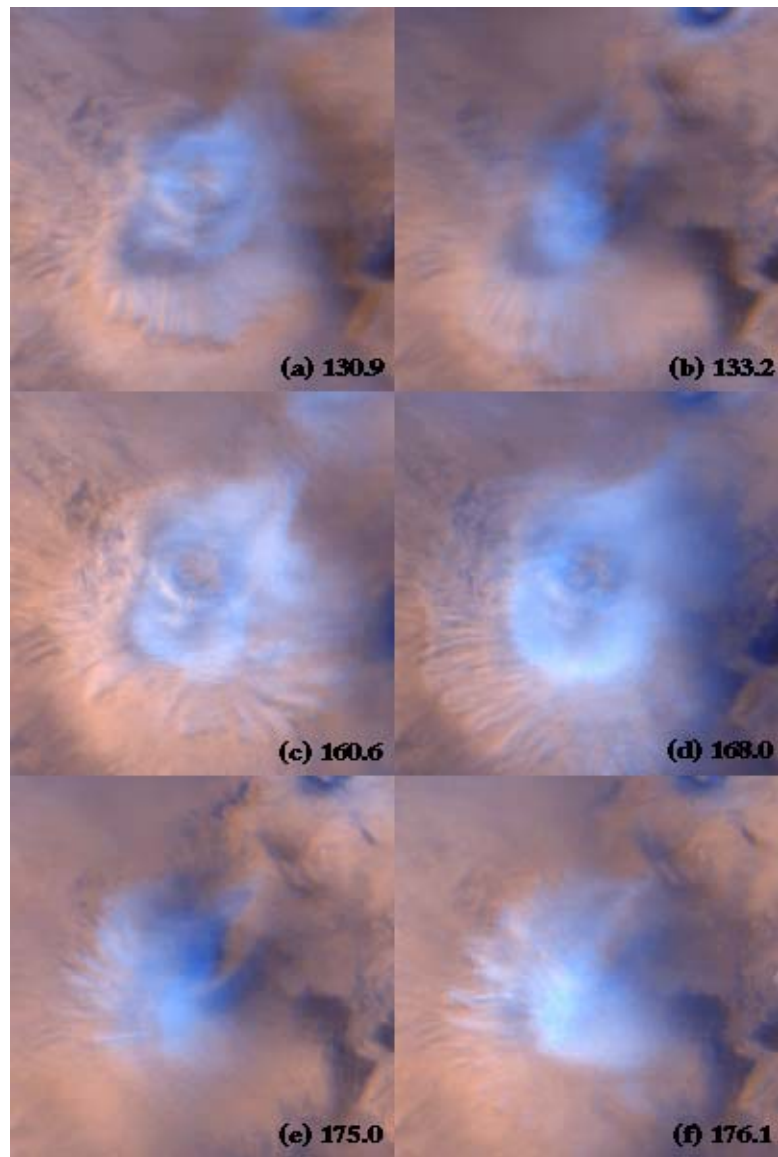


**Figure 4.11** Aster clouds above Arsia Mons in the second Martian year.

Aster clouds above the volcanoes were first observed by MGS in its first mapping year [Wang and Ingersoll, 2002]. They are characterized by a central patch and surrounding rays. Rising air above high topography could lead to central patch formation through condensation. Rafkin et al. [2002] simulated a spiral cloud over

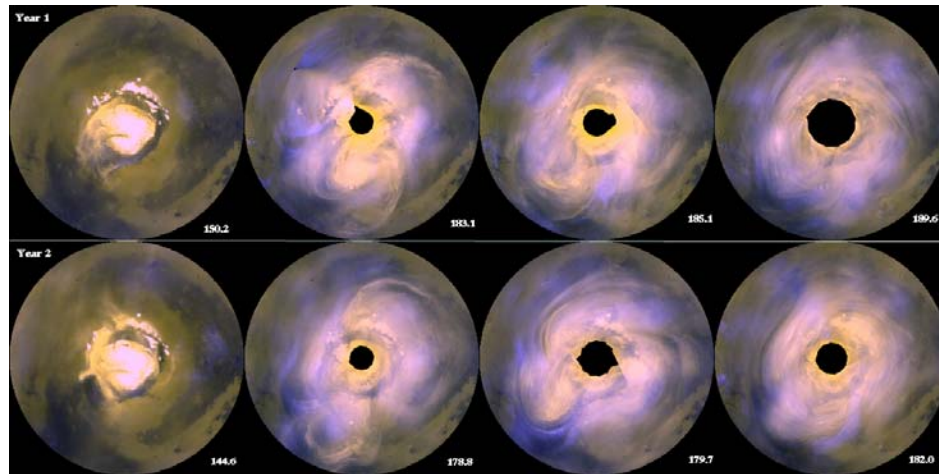
Arsia Mons using Mars Regional Atmospheric Modeling System. Their results suggest that the spiral cloud resulted from a forced thermal circulation where air parcels near the base or along the slope of the volcano traversed helical convergent paths upwards. However, they got no rays in the simulation. Convection organization following converging upslope winds in the boundary layer could produce the rays. Alternatively, rays could be related to Taylor-Gortler instability. In this case, centrifugal instability leads to longitudinal rolls when the flow turns from upslope to horizontal [Floryan, 1991]. However, Gortler instability is weak and is often associated with secondary instabilities. Aster clouds recurred above all the major volcanoes (Olympus, Ascraeus, Pavonis, Arsia and Elysium) in the same season (mid to late northern summer) in both Martian years. Similar to the first year, clouds above Arisa Mons lasted the latest into the season and provided the best examples of aster clouds. Less symmetric aster clouds are probably related to large scale winds.

#### **4.4.2 Polar clouds**

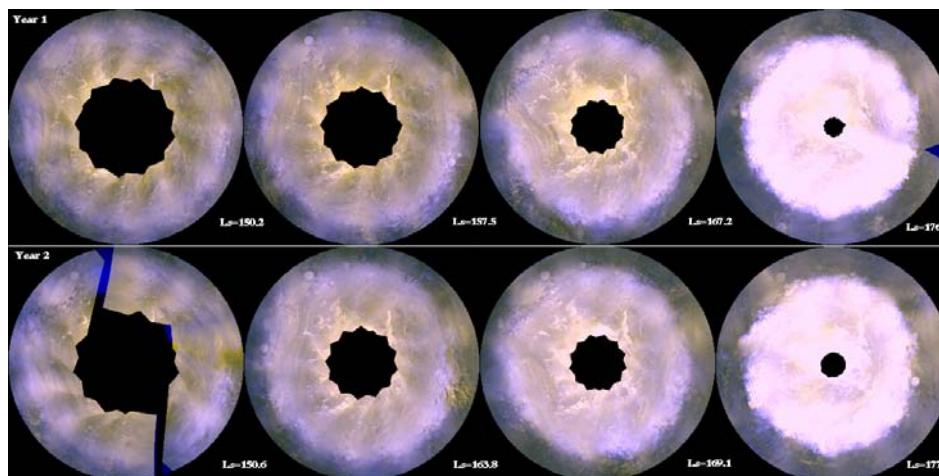
In Section 4.2.4, we discussed the effects of the 2001 global dust storm (Ls 185°) on the south and north polar clouds. However, before the storm started, the behavior of polar clouds in the north and south polar maps in 2001 was very similar to that in the previous year.

Figure 4.12 shows the comparison of north polar clouds between the first and second Martian year. Notice the morphological similarities of clouds between the two Martian years. In both years, there were cap edge dust storms and scattered condensate clouds in mid northern summer, and the north polar maps in mid summer appeared

substantially clearer than those in late summer. Following a series of large frontal storms characterized by arc-shaped arms, streak clouds formed which marked the beginning of the polar hood. Streak clouds are expected under strong winds. Their formation at the end of summer is consistent with the increasing latitudinal temperature gradient and wind speed.



**Figure 4.12** Comparison for the north polar maps from mid to late northern summer between the two Martian years.



**Figure 4.13** Comparison for the south polar maps from mid to late southern winter between the two Martian years.

Figure 4.13 shows comparison for the south polar maps from mid to late southern winter. The two Martian years again show great similarities. Mid winter clouds are dominated by streak clouds and cap edge dust storms in both years. Lee waves were abundant in both years. The direction of streaks was nearly the same, and streaks became less abundant in both years in late winter. Local dust storms still followed the receding south polar cap edge, and Martian clouds followed approximately the same seasonal cycle (except for periods with global dust storm) in both years. However, on shorter timescales, the sequence of weather phenomena at a particular place and  $L_s$  is usually different from year to year. When dust storms follow each other closely in time, the lifted dust does not have enough time to fall back onto the surface before the next storm raises more dust. Dust accumulation in the air could produce global impact on atmospheric temperatures and circulation (e.g. the 1999 cross-equatorial dust storm and 2001 global dust storm).

#### **4.4.3 “Flushing” dust storms**

In the first mapping year, MGS observed southward moving dust storms (“flushing” dust storms) transporting dust from northern high latitudes to low latitudes and even to the southern hemisphere [Cantor et al., 2001]. Dust raised by northern high latitude baroclinic storms was sometimes entrained into the Hadley return flow and transported southward. Additional dust lifting in Acidalia-Chryse channel was also observed during dust transport. “Flushing” storms occurred in the low topography regions (Acidalia, Arcadia and Utopia) within two seasonal windows before and after northern winter Solstice. Such events reoccurred in the second year after the 2001 Global dust storm. Figure 4.14 shows examples in Acidalia-Chryse for the first and

second Martian year. Wang et al. [2003] argued that “flushing” storms were favored when the daytime southward tidal flow in the Hadley return branch was synchronized with the frontal winds in the baroclinic storms. They suggested that the seasonal variability was probably related to decreased baroclinic storm activity at solstice. They also suggested that “flushing” storms had the potential to produce global impact if they occurred sufficiently close in time and transported enough dust in the southern hemisphere Hadley convergence zone.

#### **4.4.4 Spiral clouds**

Wang and Ingersoll [2002] summarized spiral clouds observed by MGS in its first mapping year. They all occurred around the north polar cap, and were observed from mid summer to early fall and from mid to late spring. Examples are shown in Figure 4.15. Spiral clouds were also observed near the north polar cap from mid northern summer to early fall of the second mapping year (our data did not cover the second spring). There were also many arc shaped clouds which may be related to less well developed spiral clouds. Some spiral clouds in the second year have very similar morphology to those in the previous year, suggesting repeatable atmospheric conditions from year to year. Figure 4.15b shows a spiral cloud with putative cold fronts, warm fronts, and occluded fronts in early northern fall of the second Martian year. It is very similar to the spiral cloud in Fig. 4.15a which occurred in the same season of the first year.

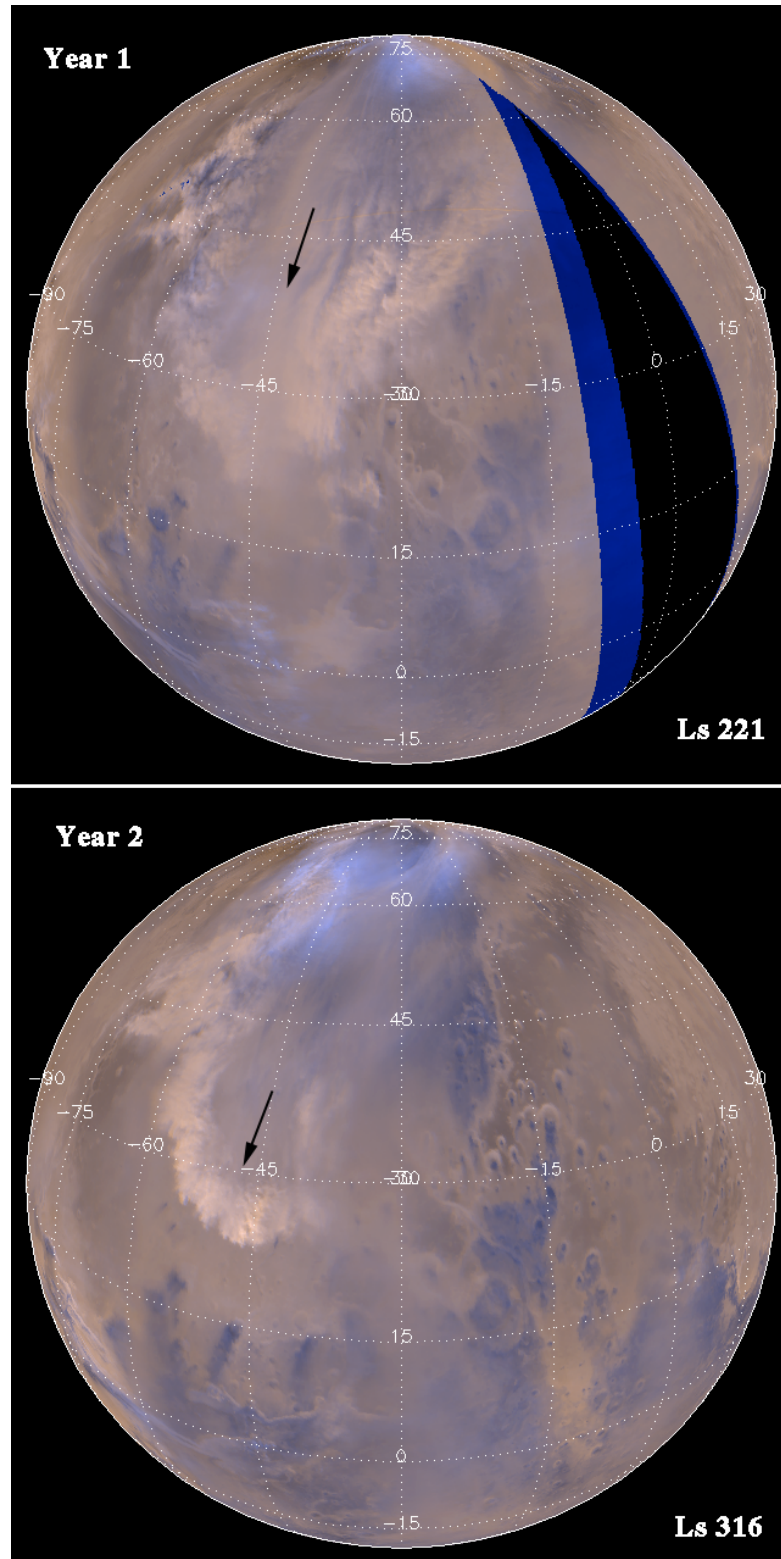


**Figure 4.14** Example “flushing” dust storms in the first and second Martian year.

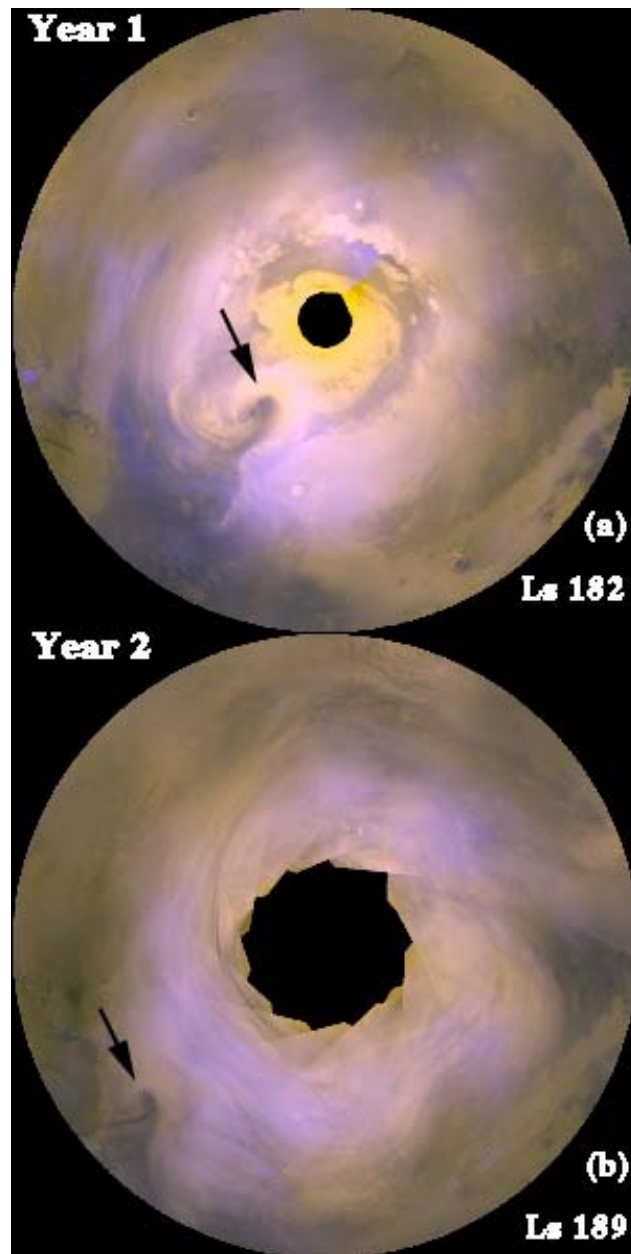


**Figure 4.15** Example spiral clouds of the first and second Martian year.

## 4.5 Summary

We processed global map swaths taken during the second MGS mapping year using data released as of October 2002. The 2001 global dust storm is the largest

difference between the first and second year. It appeared to start when several local Hellas storms continuously blew dust to the southern low latitudes and onto the seasonal south polar cap. Although very similar Hellas storms occurred in the previous year, atmospheric dust outside Hells did not get replenished by additional storms, and the dust dissipated within a week. During the developing phase of the global dust storm, active dust storm centers shifted from Hellas to Solis. The global dust storm changed the photometric behavior of Mars, suppressing the opposition surge. It brightened Hellas, Solis and Syrtis which were once active dust storm centers at different stages of global dust storm development. Cloud occurrence frequency maps derived from the blue filter are similar to those for the previous year, in spite of the 2001 global dust storm. Except for the global storm, many types of clouds (streak clouds, flushing storms, spiral clouds, aster clouds) recurred in the same season as that of the first year, suggesting repeated atmospheric conditions from year to year. Due to the short radiative timescale of the Martian atmosphere, external forcings from the sunlight distribution, surface topography, thermal inertia and albedo are likely to produce a largely repeatable atmospheric seasonal cycle.

## 4.6 References

Cantor, B. A., P. B. James, M. Caplinger, and M. J. Wolff, Martian dust storms: 1999 Mars Orbiter Camera observations, *J. Geophys. Res.*, 106 (E10), 23,653-23,687, 2001.

- Cantor, B., M. Malin, and K. S. Edgett, Multiyear Mars Orbiter Camera (MOC) observations of repeated Martian weather phenomena during the northern summer season, *J. Geophys. Res.*, 107 (E3), 10.1029/2001JE001588, 2002.
- Christensen, P. R., Global albedo variations on Mars: Implications for active Aeolian transport, deposition, and erosion, *J. Geophys. Res.*, 93 (B7), 7611-7624, 1988.
- Floryan, J. M., On the Gortler instability of boundary layers, *Prog. Aerospace Sci.*, 28, 235-271, 1991.
- Haberle, R. M., J. B. Pollack, J. R. Barnes, R. W. Zurek, C. B. Leovy, J. R. Murphy, H. Lee, and J. Schaeffer, *J. Geophys. Res.*, 98, 3093-3123, 1993.
- Hapke, B., Bidirectional reflectance spectroscopy. 4. The extinction coefficient and the opposition effect, *Icarus*, 67, 264-280, 1986.
- Neumann, G. A., D. E. Smith, and M. T. Zuber, Two Mars years of clouds detected by the Mars Orbiter Laser Altimeter, *J. Geophys. Res.*, 108 (E4), 5023, doi:10.1029/2002JE001849, 2003.
- Rafkin, S. C., M. R. V. STA. Maria, and T. Michaels, Simulation of the atmospheric thermal circulation of a martian volcano using a mesoscale numerical model, *Nature*, 419, 697-699 (2002), doi:10.1038/nature01114.
- Richardson, M. I., R. J. Wilson and A. V. Rodin, Water ice clouds in the Martian atmosphere: General circulation model experiments with a simple cloud scheme, *J. Geophys. Res.*, 107, E9, 5064, doi:10.1029/2001JE001804.

- Smith, M.D., B. J. Conrath, J. C. Pearl, and P. R. Christensen, Thermal Emission Spectrometer observations of Martian planet encircling dust storm 2001A, *Icarus*, 57, 259-263, 2002.
- Thorpe, T. E., Viking Orbiter observations of the Mars opposition effect, *Icarus*, 36, 204-215, 1978.
- Wang, H. and A. P. Ingersoll, Martian clouds observed by Mars Global Surveyor Mars Orbiter Camera, *J. Geophys. Res.*, 107 (E10), doi:10.1029/2001JE001815, 2002.
- Wang, H., M. I. Richardson, R. J. Wilson, A. P. Ingersoll, A. D. Toigo, and R. W. Zurek, Cyclones, tides and the origin of a cross-equatorial dust storm on Mars, *GRL*, 30, doi:10.1029/2002GL016828, 2003.
- Wilson, R. J., A general circulation model simulation of the Martian polar warming, *GRL*, 24, 123-126, 1997.

## Appendix

Figure 5.1 shows the brightness of the pixels between Line 700 and Line 900 as a function of the sample number for global map swath m0300717 (red) and m0300718 (blue) respectively. Red image shows general limb darkening, while blue image shows general limb brightening. The brightness variations in the images are functions of the observational geometries (incidence angles, emission angles, and phase angles), the camera response function [Caplinger, 1997] and the albedo of Mars.

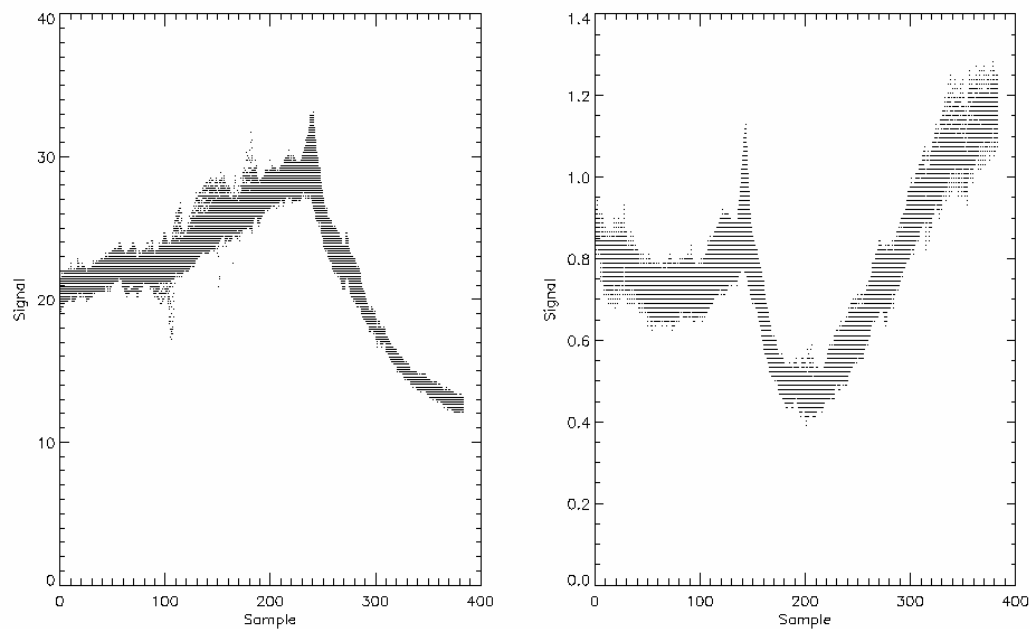


**Figure 5.1** The brightness of the pixels between Line 700 and Line 900 as a function of the sample number for global map swath m0300717 (Left, red image) and m0300718 (Right, blue image).

Incidence angle is the angle between the line of sunlight and nadir. Emission angle is the angle between the line of observation and nadir. Phase angle is the angle between the line of sunlight and the line of observation. The distributions of the

incidence, emission and phase angles of a typical global map swath (m0300717, red filter, 7.5 km/pixel, 384 samples, 1600 lines) are shown in Fig 5.2 (a-c). Due to the 2 AM – 2 PM sun-synchronous mapping orbit of MGS and the position of the push-broom MOC wide angle cameras with respect to the spacecraft, the emission angles increase from 0 at the middle sample of each line towards  $\sim 90$  at both limbs (Fig. 5.2b). The incidence angles increase from the left limb towards the right limb along each line, and increase from a minimum somewhere in the middle toward both the top and the bottom along each sample (Fig. 5.2a). The position of the line with the minimum incidence angle changes with season. The phase angles tend to 0 in the interior of the image and increase outward (Fig. 5.2c). The increase of brightness toward 0 phase angle is called the opposition surge. The position of the opposition surge changes with season as well. The blue images are mirror images of the red images, so are the incidence, emission and phase angles of the blue images.

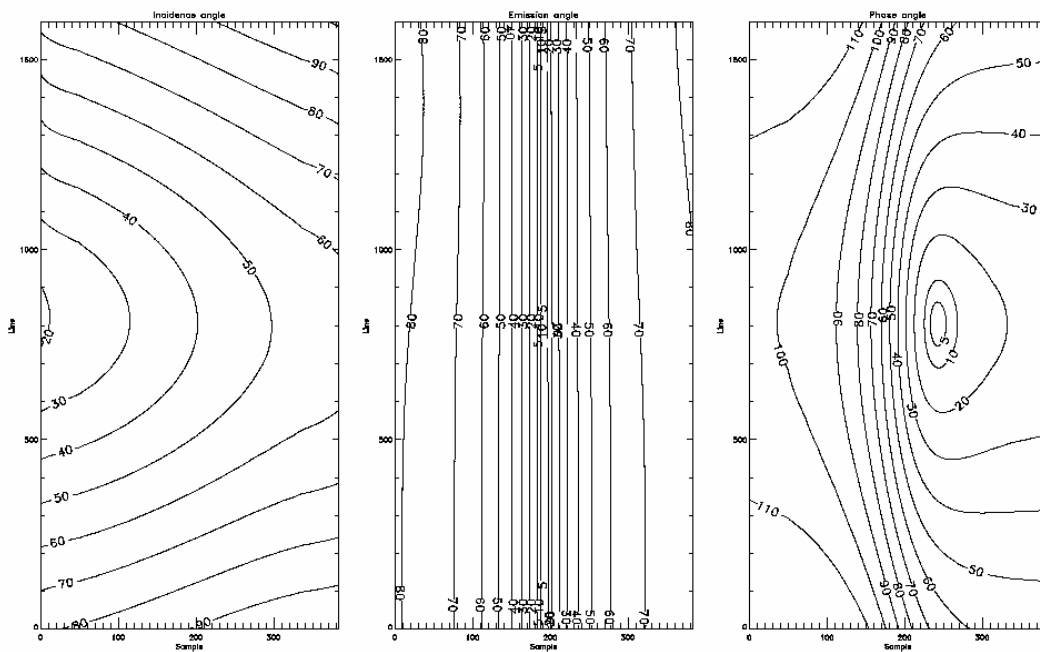


**Figure 5.2** Distribution of incidence angle (left), emission angle (middle), and phase angle (right) for image m0300717.

The MOC camera response function describes the brightness variation along a line due to the optical effects of the camera and the pixel-to-pixel variation of the response of the CCD line array. Different pixel-to-pixel response leads to the vertical streaks in the raw images. These streaks are removed by dividing an empirically derived vector after the image is flattened using a photometric function. The optical effects of the camera could lead to general brightness variation along a line even the brightness of the target is uniform. This effect is not treated separately in our study. Instead, we derive a photometric function that includes the contribution from both the observational geometries and the camera optical effect.

In order to highlight the brightness variations due to the albedo of surface features and clouds, we divide each radiometrically calibrated image by the 2D array calculated using the photometric function. This will cancel the brightness variations due to the observational geometries and camera response, and retain those due to the albedo variations of the surface and clouds.

We had 12 red and blue pairs of global map swaths (data for one day) at the time when we developed the photometric function. We chose a pair with the least albedo variations, and assumed that they represented the photometric behavior of the red and blue MOC images of a target with uniform albedo. Each pixel in the image had its own incidence, emission and phase angles. So, the brightness of the pixel was a function of its position in the image. We applied function (1.1) in Chapter 1 for the

images, and derived the values of the parameters using the method of least squares (Table 1.1).

Since successive global map swaths had large overlaps in the polar regions and small overlaps in the equatorial regions, the photometric function was required to work better in the equatorial regions. Furthermore, there were much fewer pixels with small phase angles than pixels with large phase angles in the image. If equal weight was given to every pixel in the image, then the parameters derived from least squares would favor pixels with large phase angles and would not remove the opposition surge effectively. So, we first did least squares for the 200 lines that include the opposition surge, then tuned the parameters to get a reasonable fit for the pixels near the top and bottom parts of the images (pixels with large incidence and phase angles). We then applied the parameters resulted from the previous steps as initial guesses, and did least squares fit for the lines with small phase angles again. This process was repeated until a satisfactory fit for the whole image was obtained. The derived parameter set was not unique since slight change in the initial guess can lead to different parameter values under least squares fit. The existence of the many local minima could be related to the albedo variations and pixel-to-pixel variations of the selected images among other factors. As a result, different parameter values can be derived for different images. Figure 5.3 shows least squares fit results for the pixels between Line 700 and line 900 of red image m0300717 (a) and blue image m0200381 (b) respectively. Fortunately, the parameters in Table 1.1 of Chapter 1 were generally applicable to the global map swaths in the first and second MGS mapping years.

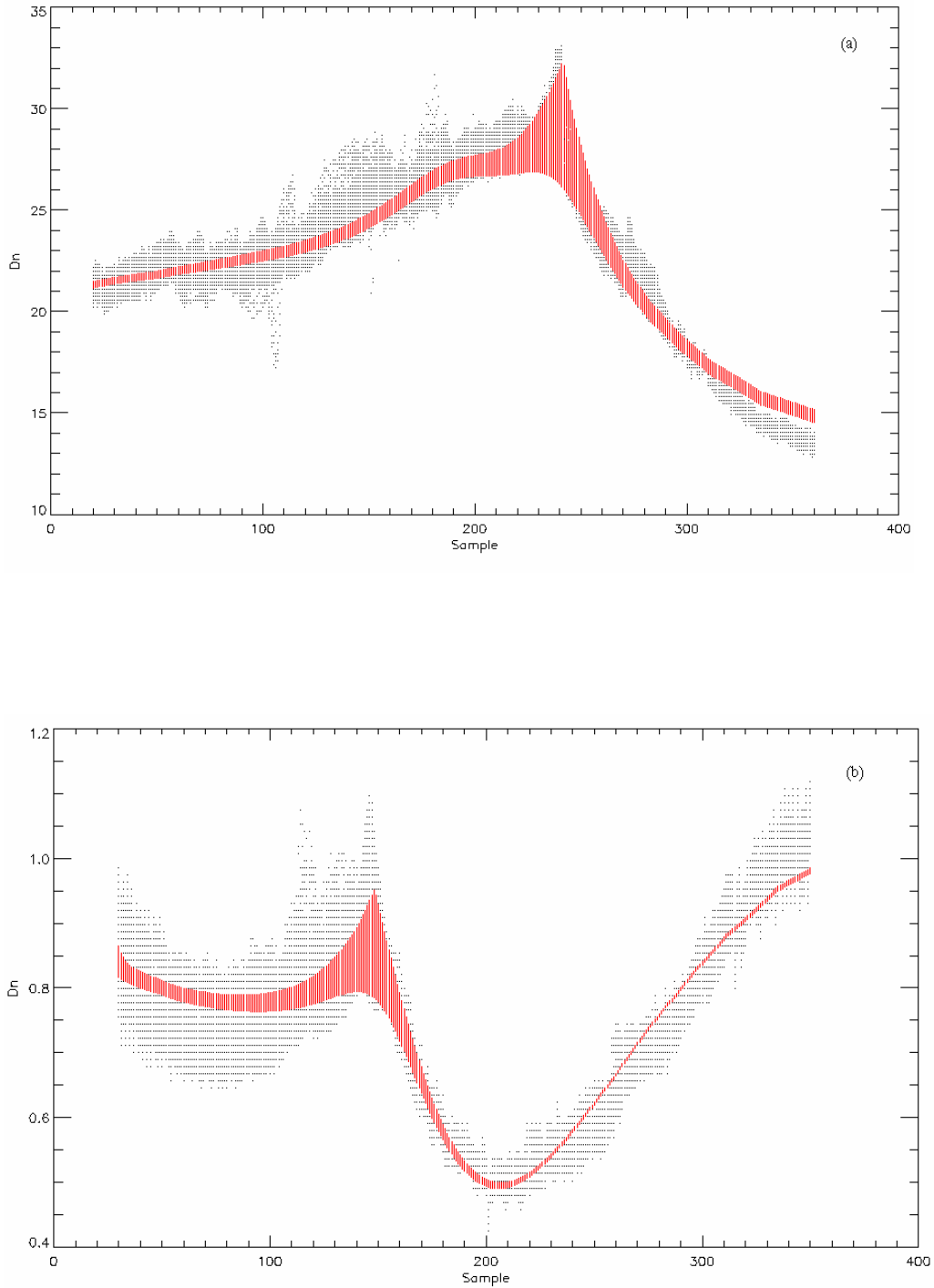


**Figure 5.3** Least squares fit results for the pixels between Line 700 and Line 900 of the (a) red image m0300717 and (b) blue image m0200381. Black dots are signals in the radiometrically calibrated images, red dots are the corresponding results calculated using parameters derived from least squares fit.